DESIGN, MODELING AND EXPERIMENTAL CHARACTERIZATION OF A FREE LIQUID-PISTON ENGINE COMPRESSOR WITH SEPARATED COMBUSTION CHAMBER

By

José A. Riofrío

Dissertation

Submitted to the Faculty of the
Graduate School of Vanderbilt University
in partial fulfillment of the requirements
for the degree of
DOCTOR OF PHILOSOPHY
in
Mechanical Engineering
December, 2008
Nashville, Tennessee

Approved:

Professor Eric J. Barth
Professor George E. Cook
Professor Michael Goldfarb
Professor Robert W. Pitz
Professor Alvin M. Strauss

ACKNOWLEDGMENTS

My deepest gratitude and appreciation goes to my adviser Dr. Eric Barth, for his extensive support throughout this work. Not only has he been an outstanding mentor and professor, but also a true friend, which enabled a remarkably rewarding experience as a graduate student. I would also like to thank the members of my dissertation committee: Dr. Michael Goldfarb, Dr. Alvin Strauss, Dr. George Cook and Dr. Robert Pitz, for their valuable guidance and support.

My experience at Vanderbilt has been greatly influenced by professors, peers, and staff members. I can say with no hesitation that everyone within the Center for Intelligent Mechatronics (and in many cases beyond the Center) has provided valuable help at one time or another. I am particularly grateful to my lab mates Chao Yong, Mark Hofacker, and Andy Willhite for their daily support. I would also like to thank John Fellenstein at the Vanderbilt Physics Machine Shop, and “Bubba” and his staff at Grooms Engines (Nashville, TN) for their valuable input towards the device fabrication. Also, our administrative staff formed by Suzanne Weiss, Myrtle Daniels and Jean Miller has gone above and beyond to keep me (and my peers) in the right track, and I am truly thankful to them.

Finally, I’d like to thank the National Science Foundation (NSF) and the Engineering Research Center for Compact and Efficient Fluid Power (CCEFP) for their financial contributions that made this work possible, as well as their direct influence in starting off my career.

TABLE OF CONTENTS

LIST OF FIGURES

LIST OF TABLES

CHAPTER I

INTRODUCTION

1.0 Motivation

The work presented in this dissertation is intended to address the current energetic limitations in untethered robotic systems of human-scale power output (in the neighborhood of 100 Watts, as defined in [1]). The existing body of work in such systems is mostly in the electromechanical domain, where the actuation is carried out by DC servo motors, and the source of electrical energy is typically Ni-Zn batteries [2]. From a design and controls perspective, these electro-mechanical systems provide convenient working platforms due to the relative ease of servo control. However, from an energetic perspective, they are fundamentally constrained by the low energy density of the batteries (250-290 kJ/kg for Ni-Zn [3]), in terms of their active duration between charges, and the relatively low power density of the servo motors [4]. Put simply, state-of-the-art batteries are too heavy for the amount of energy they store, and electric motors are too heavy for the mechanical power they can deliver, in order to present a viable combined power supply and actuation system capable of delivering human-scale mechanical work in a human-scale self contained robot package, for a useful duration of time. A state of the art example of this limitation is the Honda P3 humanoid robot, whose operational time ranges between 15 and 25 minutes before its 30-kg battery pack needs to be replaced.

A relatively new approach to developing such robotic systems is being undertaken in the pneumatic domain, where motion is typically carried out with linear pneumatic actuators. Control issues aside, linear pneumatic actuators have approximately an order of magnitude better volumetric power density and five times better mass specific power density than state of the art electrical motors [4]. Regarding power delivery, on-board air supply has shown to be a non-trivial issue, since standard air compressors are too heavy for the intended target scale, as are portable tanks with enough compressed air to supply the actuators for a useful duration of time. Goldfarb et al [5] have experimentally demonstrated the viability of utilizing hot gas released by the catalytic decomposition of hydrogen peroxide to drive pneumatic actuators, whereby the on-board supply of hot gas is carried out by a small tank of hydrogen peroxide in line with a small catalyst pack. An experimental energetic analysis carried out by Fite and Goldfarb [6] showed an achieved 45% conversion efficiency from stored chemical energy of a 70% concentration of H_2O_2 (whose lower heating value is 400 kJ/kg) to controlled mechanical work in a linear actuator. Despite its promising energetic characteristics, however, one of the biggest challenges still posed by a monopropellant-based actuation system is its high-temperature working fluid, which can present difficulties associated with valves and seals in pneumatic components.

This work presents yet an alternative approach for developing an on-board supply of cool air, via a free-piston compressor (FPC). The FPC is a compact internal combustion engine with a free-piston configuration, dynamically arranged to match the load of a pneumatic compressor of human-scale power output capability. Put simply, it serves the function of converting chemically stored energy of a hydrocarbon fuel into pneumatic potential energy of compressed air, with a combustion-driven free-piston acting as an air pump. It is shown that this dynamic arrangement (as opposed to the more traditional kinematic) can result in a compact, lightweight device capable of achieving adequate efficiencies (i.e., for its intended power scale). The combined factors of a high-energy density fuel, the efficiency of the device, the compactness and low weight of the device, and the use of the device to drive lightweight linear pneumatic actuators (lightweight as compared with power comparable electric motors) is projected to provide at least a twofold increase in total system energy density (power supply and actuation) than state of the art power supply (batteries) and actuators (electric motors) appropriate for human-scale power output. Table 1.1 below shows an energetic comparison between the electrical approach (batteries / DC motors), chemofluidic approach (H_2O_2 / pneumatic actuators) and the hereby proposed petrochemical approach (FPC / pneumatic actuators). It should be pointed out that the 1.1% efficiency goal in our proposed approach includes an assumed 30% efficiency of pneumatic actuators; hence, an overall 3.6% efficiency would be required of the Free Piston Compressor to convert from chemically stored energy of the fuel into pneumatic potential energy of compressed air in a reservoir.

Table 1-1: Energetic Comparison Between Domains

Domain	**Energy Source**	**Specific Energy Density**	**Actuation**	**Overall Conversion Efficiency**	**Overall System Energy Density**
Electrical	Batteries	~ 290 kJ/kg [3]	DC Motors	~ 50% - 90%	~145 – 260 kJ/kg
Chemofluidic	H_2O_2	~ 400 kJ/kg (70%) [6]	Pneumatic Actuators	~ 45% [6]	~180 kJ/kg
Petrochemical (FPC)	C_3H_{10}	~ 46,350 kJ/kg	Pneumatic Actuators	~ 1.1% (goal)	~ 500 kJ/kg (goal)

Free-piston engines have long held the attraction of being compact, mechanically simpler, and having fewer moving parts than crank-shaft based IC engines. Although it is widely recognized that the inertial load presented by a free-piston can be used advantageously to influence the thermal efficiency ([7],[8]), previous research fails to explicitly exploit this feature through design. The fundamental research barrier preventing this is a lack of tools regarding the design of "dynamic engines". These dynamic engines (a non-standard term) replace the kinematic dependencies of traditional engines with dynamic elements and controlled valves. Such a configuration has the potential of increased efficiency and compactness over current small scale kinematic IC engines. Efficiency is enhanced by utilizing a combination of dynamic elements, such as inertial and spring/elastic elements among other possible candidates, to transduce fuel energy into other energy domains with fewer losses. Compactness is enhanced given that dynamic elements are typically more compact and physically "simpler" than kinematic arrangements.

1.1 Previous Work

Various incarnations of free-piston engines for various applications have been attempted for more than 70 years since their conception. The idea of using a free-piston combustion-based device as a pump has been around since the documented origin of the free-piston idea. The progenitor free-piston patent by Pescara [9] was actually intended as an air compressor. Junkers developed a free-piston compressor that became widely used by German submarines through World War II [10]. The automotive industry conducted a large amount of research in the 1950's in an attempt to capitalize on the free-piston concept. Ford Motor Company considered the use of a free-piston device as a gasifier in 1954 [11] and General Motors presented the “Hyprex” engine in 1957 [12]. Such endeavors were aimed at an automotive scale engine. Similar attempts at free-piston engines in and around the 1950’s and 1960’s were unsuccessful in large part from a lack of adequate control due to mechanical, as opposed to electronic, control mechanisms [7]. In more recent times, the free-piston engine concept has been considered for small-scale power generation. Aichlmayr, et. al. [13,14,15] have considered the use of a free-piston device as an electrical power source in the 10 W range meant to compete with batteries. Beachley and Fronczak [16], among others, have considered the design of a free-piston hydraulic pump. McGee, et. al. [17] have considered the use of a monopropellant-based catalytic reaction as an alternative to combustion, as applied to a free-piston hydraulic pump. Achten, et. al. [18] at Innas have developed the Chiron free-piston engine as a direct hydraulic pump. Caterpillar, Sunpower and other companies also have a number of patents on free-piston engine technology. Very recently, Mikalsen and Roskilly [8] have carried out a comprehensive survey on free-piston engine history and applications, describing some of these and other larger-scale free-piston applications. They note that, since the free-piston engine is "restricted to the two-stroke operating principle" and therefore heavily reliant on scavenging in order to achieve proper combustion characteristics, "accurate control of piston motion currently represents one of the biggest challenges for developers of free-piston engines."

Despite this past and current work on free-piston engines, none of these previous designs explicitly exploit what is perhaps the main advantage of a free-piston, which is its capability to offer a purely inertial load to the combustion process during all or part of the stroke. This is evidenced by most free-piston engines being directly linked to a hydraulic pump and thereby "spoiling" the pure inertia of the free-piston. In fact, no efforts have been found in the literature to exploit this fact by specifically and purposefully tailoring the load dynamics through design. Although some work points out the high speed at which the piston moves, it is usually with regard to reducing emissions or other side benefits [8]. Energetically, the kinetic energy of the free-piston offers an intermediate energy storage mechanism that can be utilized to influence the transduction of heat energy to useful output work. This basic observation regarding a "free" piston as an inertial element capable of such energy storage is absent from the literature, and therefore it is not analyzed or exploited. Therefore the "gaps" in the current literature addressed in this work are 1) a recognition that the dynamic loading on the piston is the key to achieving an engine cycle with high efficiency, low noise, and other desirable attributes within the compact package of a free-piston engine; 2) a more systematic analysis of such loading in light of exploiting the intermediate kinetic energy storage of the free-piston; 3) a resulting synthesis method for the design of free-piston engine devices that have a load specifically tailored for compressing air, while also being "shaped" to benefit the combustion cycle for efficiency, power density and/or other metrics; and 4) the development of an alternative combustion configuration independent of the traditional 2-stroke principle and its associated issues of scavenging.

Earlier work by Riofrio and Barth [19] has addressed some of the aforementioned gaps in the literature and presented a preliminary free-piston compressor prototype. It was built with standard pneumatic equipment, and meant as proof of concept introduced in [20]. Figures 1-1 and 1-2 show a schematic and experimental setup of this device. The operational logistics are as follows: (1) two magnets hold the piston to the left while high-pressure fuel and air are injected into the combustion side, (2) sparked combustion occurs and the force on the piston exerted by the combustion pressure overcomes the magnetic holding, (3) the piston loads up with kinetic energy as it travels to the right and the combustion gases expand down to atmospheric pressure, (4) still in mid-stroke, the combustion gases reach atmospheric pressure and go slightly below (over-expansion), causing a breathe-in check valve to allow fresh air to quickly enter the chamber and cool down the combustion products, all while (5) the air in the rod-side of the piston is pumped into the high pressure air reservoir, and finally (6) the piston reaches the end of its stroke and the entire process takes place again from right to left.

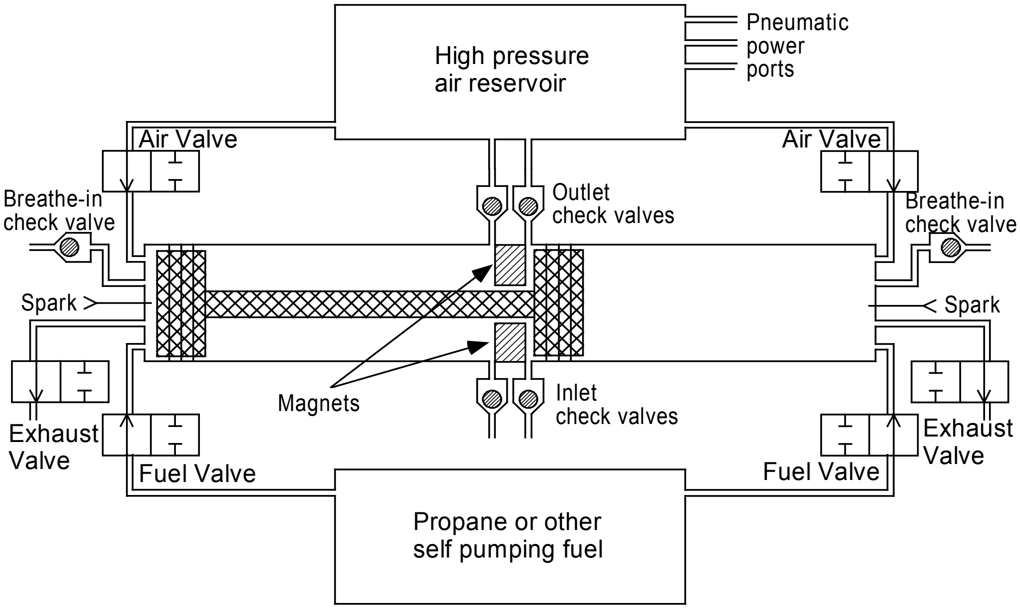

Figure 1-1: Schematic of previous free-piston compressor.

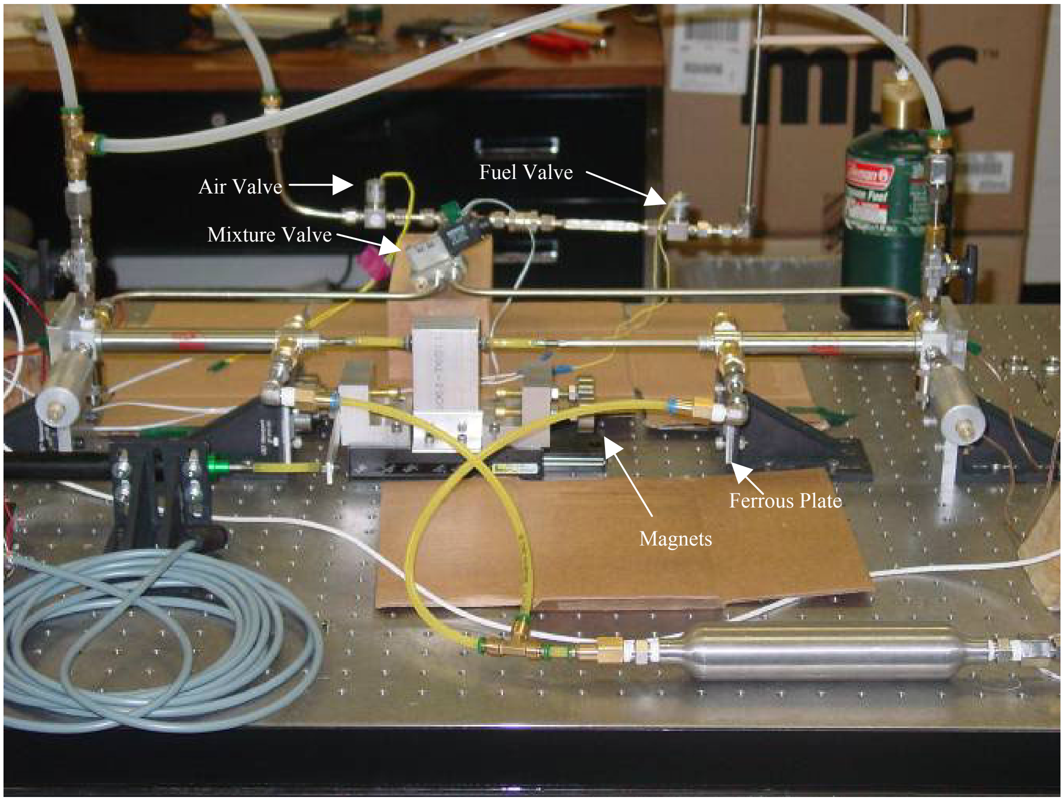

Figure 1-2: Experimental setup of previous free-piston compressor

It should be noted that due to the over-expansion and breathe-in in the combustion chamber, the free-piston compressor is self-cooling and has a quiet exhaust. Additionally, the use of high-pressure injection of air and fuel can allow for the device to operate without a starter or separate starting cycle, and more importantly, without the need for scavenging. These features, more thoroughly discussed in [19] are conceptually fundamental to the free-piston compressor and constitute a starting point for emerging research.

While this previous device successfully demonstrated the energetic merit potential of a free-piston compressor device, it fell short of achieving an adequate power density for its intended application, mostly due to the limitations of utilizing standard pneumatic cylinders and valves. As outlined in [19], these limitations include: high physical dead volume in the pump, high surface area-to-volume ratio in the combustion chamber, low combustion pressure, low frequency of operation, and finally losses attributed to seal friction, blow-by and metal-to-metal collisions.

1.2 Contribution

The work hereby presented is a full design, simulation, fabrication and experimental model validation of a new free-piston compressor device that addresses the limitations of the previous device by specifically matching the desired dynamic behavior of the system with custom-built equipment. The gaps in the literature will be addressed in more detail, most notably introducing a new combustion scheme consisting of a "separated" combustion chamber that passively delivers high-pressure combustion products to the piston for a power stroke. This implementation effectively decouples the fuel injection and combustion dynamics from the free-piston dynamics, and further allows for high-frequency operation while solving the problems associated with scavenging. A dynamics-based approach to modeling thermodynamics processes is presented and implemented. Additionally, new materials such as elastomeric membranes will be utilized to replace the conventional "piston" with equivalent passive dynamic elements in order to escape some of the fundamental losses encountered with traditional sliding piston seals. Similarly, custom-designed low-profile check valves will be introduced and experimentally validated. It is intended to highlight throughout the design that the proper arrangement of passive dynamic elements should provide optimal operational characteristics and that the free-piston engine concept should exploit the benefits offered by a purely dynamic (as opposed to kinematic) configuration. Most importantly, the fidelity of the model will be validated experimentally, and as a result it will be shown that the model will serve as an important diagnostic tool, as well as a valuable asset for future free-piston engine research endeavors.

1.3 Overview

The remainder of the document is arranged as follows: Chapter II introduces the design of a free liquid-piston compressor and its principle of operation, and present a full thermodynamic-based analysis for proper engine sizing, including estimated efficiencies; Chapter III presents a comprehensive dynamic model and simulation of the device, and its yielded results; Chapter IV presents the fabrication and experimental arrangement of the device; Chapter V shows experimental results and model validation; Chapter VI offers a thorough discussion on model-based diagnostics and suggestions for future designs; and finally, overall conclusions are presented in Chapter VII.

CHAPTER II

DESIGN OF A FREE LIQUID-PISTON COMPRESSOR

2.0 Introduction

The starting point for this new FPC design is to address the fundamental power density limitations of the earlier prototypes (dead volume in the pump, scaling of combustion chamber, low combustion pressure, low frequency of operation), as well as minimize some known energy losses (piston seal friction, blow-by leakage and metal-to-metal collisions). One known approach to eliminate piston seal friction and blow-by in pneumatic actuators is using diaphragms (particularly "rolling" diaphragms), clamped around the cylinder's circumference, and typically attached to the piston at the center. The use of rolling diaphragms was considered for the new FPC design, but a greater challenge would then be minimizing the dead volume in the pump, since a rolling diaphragm would offer much of an irregular shape (in other words, it would be difficult to match its contour to the inner pump wall). In addition, using elastomeric diaphragms with a solid piston would make attachment very difficult.

Holding on to the promising benefits of utilizing diaphragms to trap a moving piston, it was devised that a liquid slug could be used instead of any solid piston, since it would not require physical attachment to the diaphragms. Elastomeric diaphragms would then be used since their shape profile can allow for a relatively straight-forward design. It was also considered that a liquid slug trapped between these diaphragms could perfectly contour to the walls at the end of the strokes, which provided the opportunity to design a pump chamber with minimal dead volume. Assuming a "spherical segment" geometric displacement profile of such a liquid-piston arrangement, the inner pump walls of the pump chamber would be hemispherical by design. A preliminary design concept of a Free Liquid-Piston Compressor (FLPC) was visualized as a "capsule" with hemispheres at both ends and a fluid slug in the center. A simplified schematic of the FLPC is shown in Figure 2-1. All relevant chambers and components are labeled for future reference.

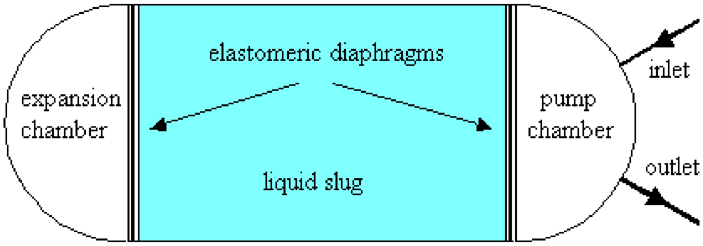

Figure 2-1: Schematic of Free Liquid-Piston Compressor (FLPC)

2.1 Tuned Resonator

The liquid slug trapped between the elastomeric diaphragms in Figure 2-1 essentially constitutes a forced mass-spring system, whereby a pulsating force input in the expansion chamber (i.e., produced by combustion) keeps the piston in oscillation with enough energy to produce the required pumping work. The fluid mass M and diaphragms' stiffness k can be selected for a desired resonant frequency $\omega_n = \sqrt{k/M}$, which would largely govern the dynamics of the return stroke barring any dead volume in the pump chamber serving as an additional returning spring-like force. An equivalent mass-spring system is represented in Figure 2-2. It should be noted that since combustion should occur at the instant where the fluid slug is fully retracted and the diaphragms are stretched in a non-equilibrium position, it will encounter very little resistance to its ideal adiabatic PV expansion. As a result, the fast acceleration of the piston immediately following combustion will promote a rapid expansion, which can reduce time-dependent losses and reactions such as heat transfer through the cylinder walls and NO_x formations [8].

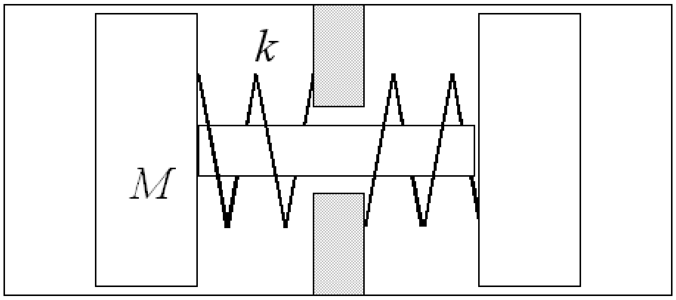

Figure 2-2: Equivalent Mass-Spring System

2.2 Combustion

Typically, free-piston engines, similarly to reciprocating kinematic engines, have their combustion event within the "expansion" chamber (as illustrated in Figure 2-1), and typical "intake" and "compression" are produced directly from the piston dynamics. This means that the power stroke has to carry enough energy to match the required load and produce the next compression. Single-piston free-piston engines generally contain a rebound device to store the energy required to carry out the next compression phase [8].

Since this device is already an air compressor, high-pressure air is available at all times. In addition, using a gaseous self-pumping fuel such as propane ensures high-pressure fuel delivery. Having pressurized air and fuel, then, makes traditional "intake" and "compression" strokes unnecessary, if instead the piston could somehow be "locked" in place at its most retracted position (i.e., "top dead center") while a high-pressure air/fuel mixture is injected and ignited. In previous designs, where standard pneumatic equipment was used, the piston rod was rigidly attached to a moving mass. This mass carried a set of magnets such that the piston would be locked in place while high-pressure air and fuel were injected. Figure 2-3 shows a picture of this configuration. It can be seen that the piston is fully retracted and the magnets are in contact with a grounded ferrous plate. The magnets were selected such that the bonding magnetic force was high enough to overcome the required injection pressure. Immediately following a sparked ignition, the combustion pressure would be significantly higher and thus overcome this magnetic force and allow the piston to "break away" from the magnetic force and generate a power stroke.

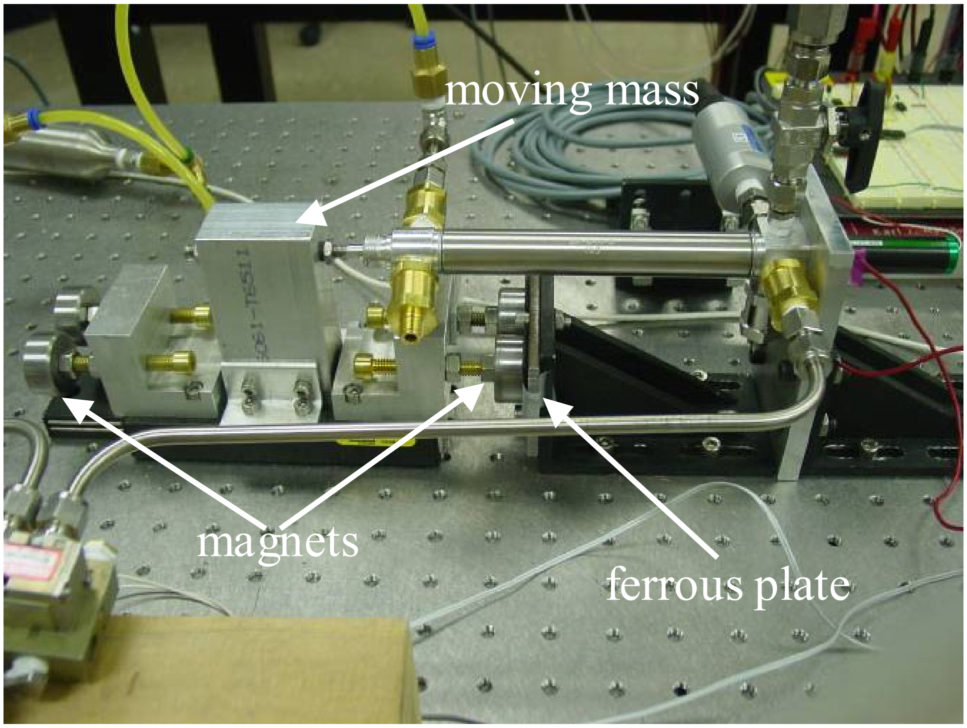

Figure 2-3: Close-up Picture of Previous FPC Configuration.

Locking the piston in place with magnets for the fuel injection phase provided significant benefits to the overall performance of the FPC. Most importantly, it facilitated the design of an over-expanded engine cycle, which, as demonstrated in [19], contributes to high efficiency, noise reduction and thermal management. Also, as previously stated, this allowed for the design of an extremely simple fuel-injection scheme, since high-pressure air and fuel were directly used. Unfortunately, however, this implementation would not be possible with a liquid piston device such as the one shown in Figure 2-1, mostly due to its geometry, and the fact that the piston is fully enclosed. The use of magneto-rheological fluid instead of water was considered, with coils wrapped around the cylinder to energize and "freeze" the fluid at desired positions; however this would require a large magnetic field (and hence, power input) and its response time would be inadequate for this application.

2.3 "Separated" Combustion Chamber

The selected approach was to implement a "separate combustor", that is, an "external" constant-volume chamber where combustion occurs, and whose combustion gases are flowed into the expansion chamber through a "combustion valve" (Figure 2-4). After the expansion stroke (i.e., power stroke), the combustion products are exhausted directly out of the expansion chamber, meaning that during the exhaust stroke the combustion valve can be fully closed and injection can occur simultaneously with exhaust. This unusual approach would decouple the fuel injection from the piston dynamics, and as a result the injection phase does not interfere with the natural resonance of the piston. This not only results in more "pure" desired dynamics, but also in higher attainable frequencies (since injection is no longer a cause for delays), and thus higher power output, while solving the problem of scavenging and issues associated with starting and stopping the engine (since "idling" would not be necessary). The bigger challenge now becomes finding a valve that can adequately channel a high-flow of high-temperature combustion products, and that can ideally open instantaneously upon ignition. In terms of standard actuated valves for pneumatic flow, the high flow area required for this application would result in inadequately large response times; not to mention the difficulty in finding a valve that could handle a constant stream of very high-temperature combustion products.

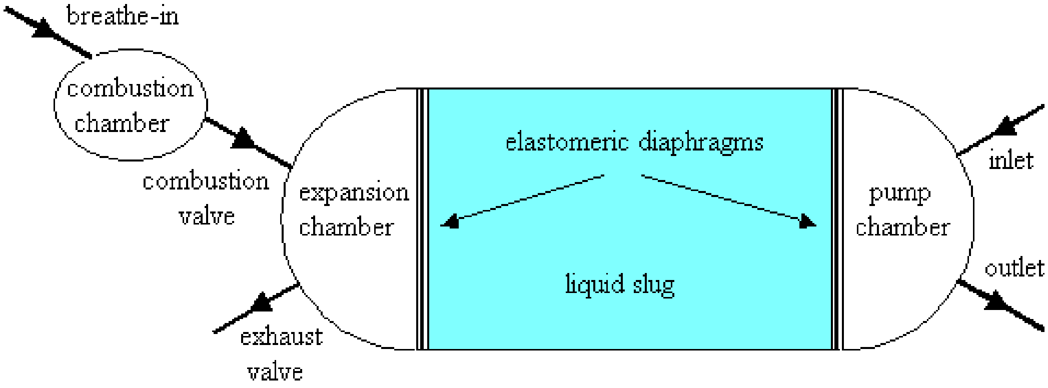

Figure 2-4: FPC With "Separated" Combustion Chamber

2.3.1 Combustion Valve

A custom-design for the implementation of a fast, high-flow, high-temperature combustion valve was formulated. An automotive valve was selected due to its high flow capacity, with a ferrous plate attached to its stem so that its opening and closing can be influenced by induced magnetic fields. Figure 2-5 shows a schematic of this arrangement. A permanent magnet holds the valve shut against the high-pressure injection of air and propane, and after a sparked combustion, the combustion pressure becomes high enough to overcome the magnetic force and throw the valve open, allowing for the high-pressure combustion products to quickly vent into the expansion chamber and perform adiabatic expansion work on the liquid-piston. The valve should stay open for a long enough duration of time such that the combustion products can expand all the way down to atmospheric pressure (over-expansion). This will happen before the end of the stroke, and the inertia-carrying remainder of the stroke will induce a check-valve to allow air into and through the combustion chamber (define this process as "breathe-in"), effectively cooling down the combustion products. The dynamics associated with the mass of the valve (with magnetic and pressure-related forces acting on it) will need to be designed properly to achieve the correct opening timing. Originally, an electromagnet was included to further influence these dynamics, but was later found to be unnecessary.

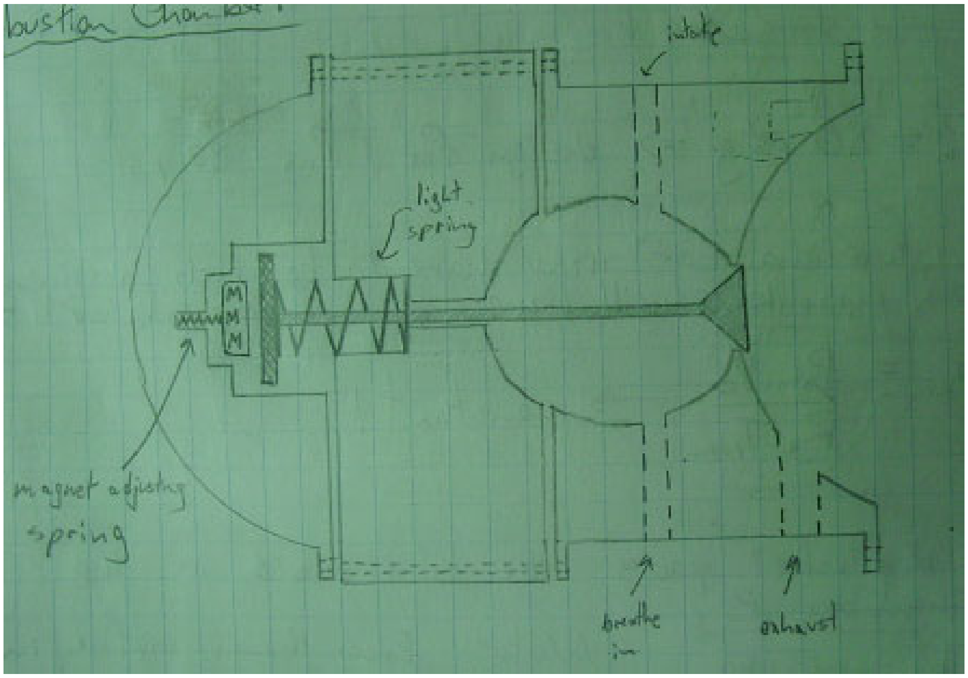

Figure 2-5: Schematic of Combustion Valve Arrangement

2.4 Thermodynamic Analysis of FLPC

A pressurized mixture of air and fuel in the "separated" combustion chamber of fixed volume V_c is characterized by the following ideal gas expression:

$$P_{inj}V_c = m_{c0}R_{inj}T_{inj} \tag{2.1}$$

where P_{inj}, m_{c0}, R_{inj} and T_{inj} are the injection pressure, mass, gas constant and temperature of the air/fuel mixture, respectively. Immediately upon ignition, assuming conservation of mass and "instantaneous" heat release of combustion, the new thermodynamic state can be represented by:

$$P_{c0}V_c = m_{c0}R_{prod}T_{c0} \tag{2.2}$$

where P_{c0} is the combustion pressure, R_{prod} is the gas constants of the combustion products, and T_{c0} is the resulting temperature, which, assuming an ideal full heat release of combustion, equals the adiabatic flame temperature for the air-supported combustion of propane, namely T_{AFT}, valued at 2250 K [21]. Combining Equations (2.1-2.2), the following expression relating the injection pressure to the resulting combustion pressure is obtained:

$$P_{c0} = \left(\frac{R_{prod}T_{AFT}}{R_{inj}T_{inj}} \right) P_{inj} \tag{2.3}$$

Since the air and fuel are already at high pressures prior to injection, it is conservatively assumed that $T_{inj} = T_{amb}$, where T_{amb} is ambient temperature. This feature of the design (i.e., the injection of a cold air/fuel mixture) serves to enhance the volumetric efficiency over other engine cycles with either intake and compression strokes (4-stroke) or scavenging and compression phases (2-stroke).

In order for the FLPC to perform efficiently, the energy produced by combustion must be "barely" sufficient for the liquid piston to complete a full stroke and pump out all the contents from the pump chamber into the reservoir. Any higher amount of combustion energy would be wasted by a collision of the liquid-piston against the compressor walls; any lower and the liquid-piston would not be able to complete a stroke, resulting in lower pump efficiency. The proper energy balance between the engine and the pump, then, is described by the following work balance:

$$W_e \geq W_{c1} + W_{c2} + W_s \tag{2.4}$$

where W_e is the work done by the expanding combustion gases on the liquid piston (resulting in kinetic energy), W_{c1} is the work required for the piston to adiabatically compress the air in the pump chamber from atmospheric pressure to "pumping" pressure (i.e., the pressure in the air reservoir), W_{c2} is the work associated with the constant-pressure pumping process (i.e., squeezing the pressurized air out of the pumping chamber and into the reservoir), and W_s is the work done to fight against the diaphragms' stiffness (only in the case where the "relaxed" volume in the pumping chamber is greater than the "relaxed" volume in the expansion chamber). As shown in [19] the values of W_e, W_{c1}, and W_{c2} are given by,

$$W_e = \frac{P_{c0} V_c^{\gamma_{prod}}}{1-\gamma_{prod}} \left(V_{e1}^{1-\gamma_{prod}} - V_c^{1-\gamma_{prod}} \right) - P_{atm} \left(V_{e1} - V_c \right) \tag{2.5}$$

$$W_{c1} = \frac{P_{atm} V_{p0}^{\gamma_{air}}}{1-\gamma_{air}} \left(V_{pi}^{1-\gamma_{air}} - V_{p0}^{1-\gamma_{air}} \right) - P_{atm} \left(V_{pi} - V_{p0} \right) \tag{2.6}$$

$$W_{c2} = \left(P_s - P_{atm}\right)\left(V_{pf} - V_{pi}\right) \tag{2.7}$$

where γ_{prod} and γ_{air} are the ratios of specific heats of combustion products and air, respectively, V_{e1} is the total volume in the combustion side (combustion chamber plus expansion chamber) when the combustion gases have expanded down to atmospheric pressure, P_{atm} is atmospheric pressure, V_{p0} and V_{pi} are the initial volume in the pump chamber and the intermediate volume at which compression ends and pumping begins, respectively, V_{pf} is the final volume in the pump chamber after pumping (i.e., dead volume), and P_s is the required pumping pressure (i.e., pressure in the air reservoir). The value of W_s is given by,

$$W_s = \frac{k}{2\pi^2 r^4}\left(V_{p\_rlx} - V_{e\_rlx}\right)^2 \tag{2.8}$$

where r is the radius of the fluid chamber (and hemisphere) and V_{p_rlx} and V_{e_rlx} are the volumes in the pump and expansion chambers, respectively, when the diaphragms are relaxed.

Assuming the value of W_s is very small compared to W_e, W_{c1}, and W_{c2}, the following expression relating V_{p0} and V_c can be derived from Equations (2.4-2.6):

$$\frac{V_c}{V_{p0}} = \frac{\dfrac{\gamma_{air} P_{atm}}{(1-\gamma_{air})}\left[1 - \left(\dfrac{P_{atm}}{P_s}\right)^{\frac{1-\gamma_{air}}{\gamma_{air}}}\right]}{\dfrac{P_{c0}}{(1-\gamma_{prod})}\left[\gamma_e \left(\dfrac{P_{atm}}{P_{c0}}\right)^{\frac{\gamma_{prod}-1}{\gamma_{prod}}} - 1 + (1-\gamma_{prod})\left(\dfrac{P_{atm}}{P_{c0}}\right)\right]} \tag{2.9}$$

This functionally constrained volume ratio of V_c to V_{p0} is required to meet the balance condition imposed by Equation (2.4), and therefore constitutes a critical design tool for the overall sizing of the chambers.

In addition to the work balance shown by Equation (2.4), it is necessary that the device achieves a certain amount of breathe-in (i.e., intake of air through a check valve upon overexpansion) to ensure cool operation of the device. Define a *breathe-in factor* α, such that

$$V_{p0} = \alpha V_{e1} \tag{2.10}$$

where breathe-in occurs as long as α is greater than 1.

2.4.1 Energetic Characterization

It is desirable to have an expression for stored pneumatic potential energy in a reservoir as a function of only its pressure and volume. This could be used for calculating the net energy delivered to the air reservoir by the FLPC, either on a per-stroke basis or over a determined period of time. Such an expression can be derived directly from the fundamental internal energy equation of a gas, given by,

$$\Delta U = mc_v \Delta T \tag{2.11}$$

which states that the net energy increase (ΔU) in a control volume (bounded by constant mass m) is only a function of its net temperature increase (ΔT), assuming that no heat or enthalpy fluxes occur. (c_v is the constant-volume specific heat of the gas in question). Since Equation (2.11) can be used to determine the energy differential between any two thermodynamic states of an ideal gas, we must clearly specify a "reference" state with which to compare our pneumatic potential energy. From the point of view of pneumatic actuation, this reference state should have the control volume mass at atmospheric pressure, occupying whatever amount of volume it naturally needs to. This should be intuitive since air at atmospheric pressure has precisely zero potential to perform work (i.e., in a pneumatic actuator at atmospheric conditions). Therefore, Equation (2.11) can be expanded as

$$\Delta U = mc_v T_{res} - mc_v T_{ref} \tag{2.12}$$

where T_{res} and T_{ref} are the temperatures of the "final" and "reference" states, respectively. Applying gas constant properties, Equation (2.12) can be written as

$$\Delta U = \frac{mRT_{res}}{\gamma - 1} - \frac{mRT_{ref}}{\gamma - 1} \tag{2.13}$$

where, recall, R and γ are the gas constant and ratio of specific heats of the gas, respectively. Further, from the ideal gas law, the following substitution can be made:

$$\Delta U = \frac{P_{res} V_{res}}{\gamma - 1} - \frac{P_{atm} V_{ref}}{\gamma - 1} \tag{2.14}$$

where P_{res} and V_{res} are the pressure and volume in the reservoir and V_{ref} is the volume that the mass occupies in its "reference" atmospheric state. Since the "final" and "reference" states have an adiabatic relationship, the following expression must be true:

$$V_{ref} = \left(\frac{P_{res}}{P_{atm}} \right)^{\frac{1}{\gamma}} V_{res} \tag{2.15}$$

Substituting into Equation (2.14) and expanding,

$$\Delta U = \frac{P_{res} V_{res}}{\gamma - 1} - \frac{P_{atm} \left(\frac{P_{res}^{1/\gamma}}{P_{atm}^{1/\gamma}} \right) V_{res}}{\gamma - 1} \tag{2.16}$$

Finally, after simplifying and rearranging, the following final expression is obtained:

$$\Delta U = \frac{P_{res} V_{res}}{1-\gamma}\left[\left(\frac{P_{res}}{P_{atm}}\right)^{\left(\frac{1-\gamma}{\gamma}\right)} - 1\right] \tag{2.17}$$

Equation 2.17, then, can provide the total amount of pneumatic energy stored in the air reservoir as a function of its pressure. Note that this same expression can be derived based on the capacity of the pressurized gas to perform full adiabatic work in a pneumatic actuator.

Assuming the work balance condition given by Equation (2.4) is met, and the liquid-piston completes a full "efficient" stroke, the energy-per-stroke delivered by the FLPC to the air reservoir can be determined based on the net amount of mass of air that enters the reservoir. Applying Equation (2.17), and assuming that this mass will occupy a partial volume V_f in the reservoir, its final stored pneumatic potential energy can be given by,

$$E_{net} = \frac{P_s V_f}{1-\gamma_{air}}\left[\left(\frac{P_s}{P_{atm}}\right)^{\frac{1-\gamma_{air}}{\gamma_{air}}} - 1\right] \tag{2.11}$$

It should be noted that the mass in question should exclude the mass of air required for the subsequent injection. With this in mind, and assuming complete heat loss in the reservoir for the hot pumped air, the partial volume V_f is calculated as,

$$V_f = \frac{R_{air} T_{amb}}{P_s}\left(m_p - m_{air\_inj}\right) \tag{2.12}$$

where T_{amb} is the ambient temperature, m_p is the total mass of air pumped out of the pump chamber, originally contained in volume V_{p0} and thus described by:

$$m_p = \frac{P_{atm} V_{p0}}{R_{air} T_{amb}} \tag{2.13}$$

and m_{air_inj} is the mass of air required for air/fuel injection, which, for a stoichiometric mixture of propane and air, is given by the following relationship:

$$\frac{m_{air\_inj}}{m_{fuel\_inj}} = 15.53 \tag{2.14}$$

where m_{fuel_inj} is the total mass of propane required for injection. The overall efficiency of the device can be calculated by dividing the obtained net energy transfer (E_{net}) by the original amount of chemically stored energy in the injected mass of air/fuel mixture. As shown in [19], this is given by,

$$\eta = \frac{E_{net}}{m_{c0} e} \tag{2.15}$$

where m_{c0}, recall, is the mass of the air/fuel mixture injected into the combustion chamber, and therefore:

$$(m_{c0} = m_{air\_inj} + m_{fuel\_inj}) \tag{2.16}$$

and e is computed from the lower heating value for the stoichiometric combustion of propane:

$$\begin{aligned} e &= \frac{46350\,\text{kJ}}{\text{kg fuel}} \times \frac{1\,\text{kg fuel}}{16.63\,\text{kg air/fuel mixture}} \\ &= 2787\,\frac{\text{kJ}}{\text{kg air/fuel mixture}} \end{aligned} \tag{2.17}$$

Combining Equations (2.11), (2.12), (2.14), and substituting them into Equation (2.15), the following expression can be derived:

$$\eta = \frac{1}{e} \cdot \frac{15.63 R_{air} T_{amb}}{16.63 (1 - \gamma_{air})} \left(\frac{m_p}{m_{air\_inj}} - 1 \right) \left[\left(\frac{P_s}{P_{atm}} \right)^{\frac{1-\gamma_{air}}{\gamma_{air}}} - 1 \right] \tag{2.18}$$

Finally, by combining Equations (2.1), (2.13), (2.14) and (2.16), the ratio $\frac{m_p}{m_{air\_inj}}$ contained in Equation (2.18) is related to the ratio $\frac{V_c}{V_{p0}}$ by the following expression:

$$\frac{m_p}{m_{air\_inj}} = \frac{16.63 R_{inj} P_{atm}}{15.63 R_{air} P_{inj}} \cdot \left(\frac{V_c}{V_{p0}} \right)^{-1} \tag{2.19}$$

For future reference, the values of all the applicable gas constants are given below:

$$R_{prod} = 0.2935 \frac{\text{kJ}}{\text{kg} \cdot \text{K}} \qquad R_{inj} = 0.2829 \frac{\text{kJ}}{\text{kg} \cdot \text{K}} \qquad R_{air} = 0.288 \frac{\text{kJ}}{\text{kg} \cdot \text{K}}$$

$$\gamma_{prod} = 1.249 \qquad \gamma_{inj} = 1.366 \qquad \gamma_{air} = 1.398$$

where the subscripts $_{prod}$, $_{inj}$ and $_{air}$ correspond to the combustion products, injection mixture, and fresh air, respectively.

2.4.2 Maximum Theoretical Efficiency

It is clear from Equations (2.18), (2.19) and (2.9) that overall efficiency of the FLPC is dependent only on the values of combustion pressure P_{c0}, and air reservoir pressure P_s, assuming that the work balance in Equation (2.4) is met. It is important to point out that geometry and size of the device do not affect this efficiency, if heat transfer issues associated with physical scaling are neglected. With regard to power capability of the device, however, sizing is important since the net energy delivered to the air reservoir per stroke depends on the quantity of $\left(m_p - m_{air\_inj}\right)$. The power characteristics of the FLPC will be addressed later.

Based on reasonable supply expectations for a human-scale pneumatic robot, the reservoir pressure P_s is targeted as 650 kPa (80 psig). Similarly, the injection pressure P_{inj} is selected as 650 kPa since the injection of air for combustion comes directly from the reservoir. Applying Equation (2.3), the combustion pressure yielded from the selected injection pressure P_{c0} is calculated as 5.08 Mpa (737 psig). Further, Equation (2.9) can now be calculated as:

$$\left.\frac{V_c}{V_{p0}}\right|_{ideal} = 0.0283 \tag{2.20}$$

This ratio becomes a key factor for the design because it reveals the required size of the combustion chamber in relation to the "displacement" volume of the liquid-piston. Notice that since Equation (2.3) assumes a complete heat release of combustion and no heat losses in the combustion chamber, this ratio represents an ideal case scenario that will be used to determine a maximum system efficiency attainable with the desired design parameters P_s and P_{inj}.

Combining Equations (2.18-2.20), and including the values for the gas constants and selected parameters P_{c0} and P_s, the maximum theoretical system efficiency is calculated as:

$$\boxed{\eta_{theory} = 14.26\%} \tag{2.21}$$

2.5 Dimensional Analysis and Sizing

The desired "displacement" volume V_{p0} can be selected based on the expected power delivery of the FLPC. Targeting 100 Watts of delivered power to the reservoir, and conservatively estimating an operating frequency $f_0 \approx 10\,\text{Hz.}$, a full stroke of the FLPC would need to deliver 10 Joules of pneumatic potential energy to the reservoir. Calculating Equations (2.11-2.12) (and thus accounting for air re-investment for combustion), the following required amount of mass pumped per stroke is determined:

$$m_p - m_{air\_inj} = 0.1158\,\text{grams} \tag{2.22}$$

However, since the ratio of $\frac{m_p}{m_{air\_inj}}$ is intrinsically linked to combustion pressure P_{c0}, an assessment must be made regarding combustion efficiency. Equation (2.3) assumes full heat release of combustion and hence a resulting combustion temperature T_{AFT}. This was a theoretical best case scenario, used for the sake of calculating the maximum theoretical system efficiency in the previous section. Based on previous experience, however, the actual expected combustion temperature is conservatively estimated as $\frac{1}{2}T_{AFT}$, or 1125 K. Maintaining the target injection pressure of 650 kPa, the new yielded combustion pressure is about 2.54 MPa (367 psig). Re-calculating Equation (2.9) we get the following ratio $\frac{V_c}{V_{p0}}$ for actual design:

$$\left.\frac{V_c}{V_{p0}}\right|_{design} = 0.0694 \tag{2.23}$$

and therefore, Equation (2.19) yields:

$$\frac{m_p}{m_{air\_inj}} = 2.3372 \tag{2.24}$$

Solving Equations (2.22) and (2.24) we get:

$$\begin{aligned} m_p &= 0.1956 \text{ grams} \\ m_{air\_inj} &= 0.0837 \text{ grams} \end{aligned} \tag{2.25}$$

Finally, the "displacement" volume V_{p0} can be determined by substituting the newfound value of m_p into Equation (2.13). This results in:

$$V_{p0} = 166.8 \text{ cc} \tag{2.26}$$

Referring back to Figure 2-4, it should be pointed out that the volume V_{p0} corresponds to the *sum* of the "relaxed" expansion and pump chamber volumes, namely V_{e_rlx} and V_{p_rlx}. This should be intuitive since, as previously described, the liquid-piston begins its stroke from a fully retracted position. The volume in the pump chamber is designed as a hemisphere, such that the liquid piston can match the contour of the compressor's inner walls and thus result in near zero dead space. However, since the return stroke is driven solely by the passive dynamics of the liquid-piston, the "relaxed" volume in the expansion chamber needs to be determined based on the maximum overshoot of the mass-spring-damper system. The maximum percent overshoot was conservatively selected as 50%, resulting in a damping ratio of 0.21 – a behavior reasonably expected from a liquid slug trapped between commercially available silicone rubber sheets. Therefore, this volume was assigned to be half of the pump chamber's. This gives the following geometrical constraint:

$$V_{e\_rlx} = 0.5V_{p\_rlx} = 0.5\left(\tfrac{2}{3}\pi r^3\right) = \tfrac{1}{3}\pi r^3 \tag{2.27}$$

yielding, finally:

$$V_{p0} = V_{e\_rlx} + V_{p\_rlx} = \pi r^3 \tag{2.28}$$

where r is the cylindrical radius of the liquid-piston.

The desired natural frequency f_0 plays a role in determining the required diaphragm stiffness and the mass of the liquid-piston (the latter determining its length). For $f_0 = \frac{\omega_n}{2\pi} \approx 10\,\text{Hz.}$, the preliminary values of diaphragm stiffness and liquid-piston mass were reasonably selected as $k \approx 2000\,\text{N/m}$ and $M \approx 0.5\,\text{kg}$. Table 2-1 shows a complete list of all the important design values and parameters.

Table 2-1: FLPC Design Parameters

Parameter	***Description***	***Approximate Value***
P_{inj}	*Injection Pressure*	**650 kPa**
P_{c0}	*Combustion Pressure*	**2.54 MPa**
P_s	*Reservoir Pressure*	**650 kPa**
V_c	*Volume of "Separated" Combustion Chamber*	**11.58 cc**
r	*Radius of Liquid-Piston*	**3.76 cm**
V_{p0}	*"Displacement" Volume of Liquid-Piston*	**166.8 cc**
k	*Spring Constant of Diaphragms*	**2000 N/m**
M	*Mass of Liquid-Piston*	**0.5 kg**
α	*Breathe-in Factor*	**1.09**
f_0	*Operating Frequency*	**10 Hz**
T	*Net Power Delivered to Reservoir*	**100 W**
η	*Overall Efficiency*	**4.03 %**

With all the selected design parameters, a Pro/ENGINEER model of the complete FLPC assembly was drawn. It is shown in Figure 2-5 below.

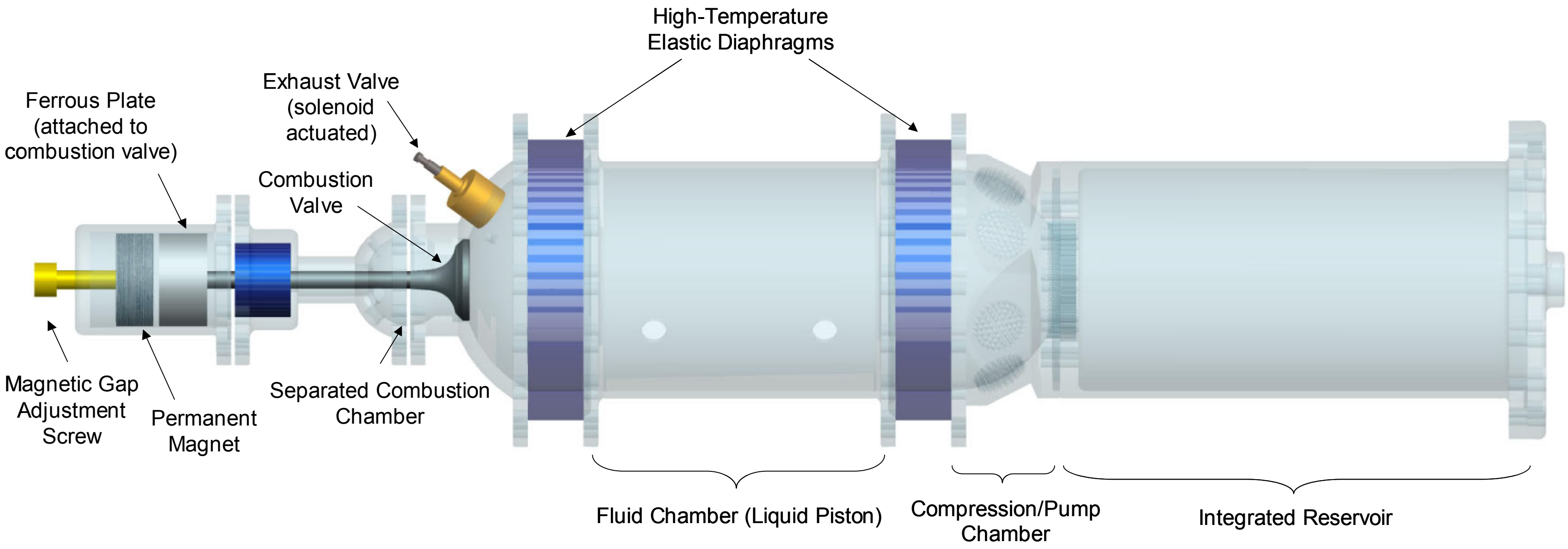

Figure 2-6: Pro/ENGINEER Model of FLPC

CHAPTER III

MODELING AND SIMULATION OF FREE LIQUID-PISTON COMPRESSOR

3.0 Dynamic Model of FLPC

While a full thermodynamic analysis was important to establish a work balance that is paramount in determining "static" design choices (pressures, volumes, geometry, etc) for a certain target efficiency and energy delivered per stroke, a complementary dynamic model is needed to analyze and design the time-based behavior of the system. Beyond looking at thermodynamic equations of state, dynamic processes such as inertial dynamics, enthalpy flows, heat fluxes and mass flow rates are taken into account. The main objectives of generating this model are 1) to assess and validate the inertial loading characteristics of the FLPC, 2) to analyze the time-based energetic behavior of the system, and perhaps most importantly 3) to study the sensitivity of the system to the variation of key design parameters such as piston mass, spring constant, dead volumes, etc.

For simplicity, the liquid-piston was modeled as the mass-spring-damper system shown in Figure 3-1. Three control volumes were considered: the combustion chamber (constant volume), the expansion chamber, and the pump chamber (all shown in Figure 3-1). Additionally, mass flow rates were modeled through all five channels: breathe-in check-valve in the combustion chamber, combustion valve between the combustion and expansion chambers, exhaust valve in the expansion chamber, and inlet and outlet check-valves in the pump chamber. Finally, the inertial dynamics of the liquid piston and the combustion valve were included to relate the time-based behavior of all three control volumes.

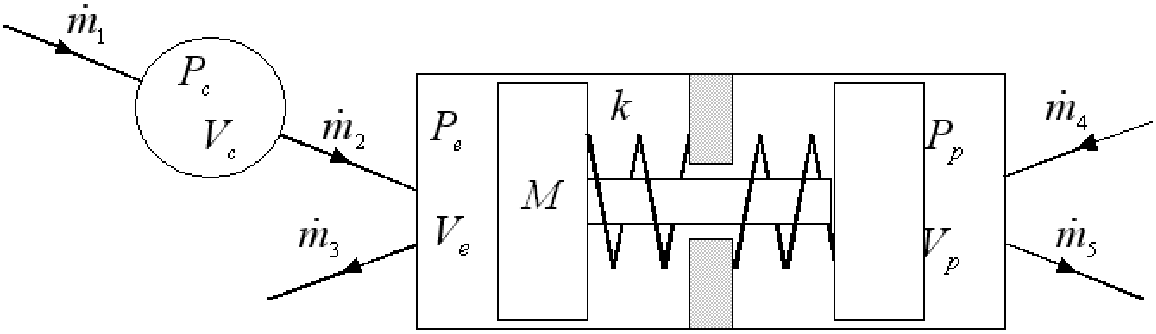

Figure 3-1: Simplified FLPC for Simulation.

In general, a power balance in a given control volume is characterized by the following expression:

$$\dot{U}_j = \dot{H}_j + \dot{Q}_j - \dot{W}_j \tag{3.1}$$

where j is a subscript index indicating a particular control volume, $\dot{U}$ is the rate of change of internal energy, $\dot{H}$ is the net enthalpy flow into the CV, $\dot{Q}$ is the heat flux into the CV, and $\dot{W}$ is the rate of work done by the gas in the CV. The values of $\dot{H}$, $\dot{W}$ and $\dot{U}$ can be expanded in the following way:

$$\dot{H}_j = \sum \dot{m}_j \left(c_{p_{in/out}}\right)_j \left(T_{in/out}\right)_j \tag{3.2}$$

$$\dot{W}_j = P_j \dot{V}_j \tag{3.3}$$

$$\dot{U}_j = \dot{m}_j (c_v)_j T_j + m_j (c_v)_j \dot{T}_j = \frac{1}{\gamma_j - 1}\left(\dot{P}_j V_j + P_j \dot{V}_j\right) \tag{3.4}$$

where $\dot{m}$ is an individual mass flow rate entering (positive sign) or leaving (negative sign) the CV, $c_{p_{in/out}}$ and $T_{in/out}$ are the constant pressure specific heat and the temperature of the substance entering or leaving the CV, respectively, P, V and T are the pressure, volume and temperature in the CV, respectively, c_v is the constant volume specific heat of the substance in the CV, and γ is the ratio of specific heats of the substance in the CV. Combining Equations (3.1-3.4), the following differential equations can be obtained:

$$\dot{P}_j = \frac{(\gamma_j - 1)\sum \dot{m}_j \left(c_{p_{in/out}}\right)_j \left(T_{in/out}\right)_j + (\gamma_j - 1)\dot{Q}_j - \gamma_j P_j \dot{V}_j}{V_j} \tag{3.5}$$

$$\dot{T}_j = \frac{\sum \dot{m}_j [\left(c_{p_{in/out}}\right)_j \left(T_{in/out}\right)_j - (c_v)_j T_j] - P_j \dot{V}_j + \dot{Q}_j}{m_j (c_v)_j} \tag{3.6}$$

Additionally, the mass flow rates through all five valves are modeled by the following standard equations [22]:

$$\dot{m}_j = a_j \psi_j (P_u, P_d) = \begin{cases} a_j C_d C_1 \dfrac{P_u}{\sqrt{T_u}} & \text{if} \quad \dfrac{P_d}{P_u} \le P_{cr} \\ a_j C_d C_2 \dfrac{P_u}{\sqrt{T_u}} \left(\dfrac{P_d}{P_u}\right)^{1/\gamma_u} \sqrt{1 - \left(\dfrac{P_d}{P_u}\right)^{\gamma_u - 1/\gamma_u}} & \text{if} \quad \dfrac{P_d}{P_u} > P_{cr} \end{cases} \tag{3.7}$$

where C_d is a nondimensional discharge coefficient of the valve, a is the area of the valve orifice, P_u and P_d are the upstream and downstream pressures, T_u is the upstream temperature, γ_u is the ratio of specific heats in the upstream substance, and C_1, C_2 and P_{cr} are substance-specific constants given by

$$C_1 = \sqrt{\frac{\gamma_u}{R_u}\left(\frac{2}{\gamma_u + 1}\right)^{\gamma_u + 1/\gamma_u - 1}} \tag{3.8}$$

$$C_2 = \sqrt{\frac{2\gamma_u}{R_u(\gamma_u - 1)}} \tag{3.9}$$

$$P_{cr} = \left(\frac{2}{\gamma_u + 1}\right)^{\gamma_u/\gamma_u - 1} \tag{3.10}$$

where R_u is the gas constant of the upstream substance. For simulation, all valves are assumed to open and close instantaneously (on/off), except for the combustion valve, which due to its larger inertia was dynamically modeled such that its valve orifice has a time-dependence.

3.0.1 Combustion Chamber

The "separated" combustion chamber is modeled with two one-way mass flows, namely $\dot{m}_1$ (breathe-in check valve) and $\dot{m}_2$ (combustion valve). Since the volume of this chamber is constant, $\dot{V}_c = 0$, and therefore applying Equations (3.5-3.6) for this chamber yields:

$$\dot{P}_c = \frac{(\gamma_c - 1)\left(\dot{m}_1 c_{p_{air}} T_{amb} - \dot{m}_2 c_{p_c} T_c\right) + (\gamma_c - 1)\dot{Q}_c}{V_c} \tag{3.11}$$

$$\dot{T}_c = \frac{\dot{m}_1\left(c_{p_{air}} T_{air} - c_{v_c} T_c\right) - \dot{m}_2 R_c T_c + \dot{Q}_c}{m_c c_{v_c}} \tag{3.12}$$

where the gas-specific values γ_c, c_{p_c} and c_{v_c} correspond to the species concentration contained in the chamber. Immediately after combustion, the mass composition in the chamber consists purely of combustion products. Upon breathe-in this composition is no longer constant, since fresh air begins to enter the chamber through the breathe-in check valve while the combustion valve continues to flow out. Therefore, the specific heats were continuously recalculated based on the partial mass of each substance present in CV and their molecular weight averages is included in the model. This formulation starts with the principle of conservation of mass:

$$\dot{m}_c = \dot{m}_1 - \dot{m}_2 \tag{3.13}$$

where $\dot{m}_c$ is the rate of change of mass in the combustion chamber. Integrating Equation (3.13), the total amount of mass present in the chamber after some time t is:

$$m_c = \int_{t_0}^{t} \dot{m}_1 dt - \int_{t_0}^{t} \dot{m}_2 dt + m_c\Big|_{t=t_0} \tag{3.14}$$

For the sake of simulation, t_0 corresponds to the instant after ignition where combustion pressure is at its highest. Therefore $m_c\big|_{t=t_0} = m_{c0}$, which, recall, is the mass of the combustion mixture in the chamber.

Since the total mass present in the chamber is a sum of the mass of each present species, it can be expressed as:

$$m_c = m_{c\_prod} + m_{c\_air} \tag{3.15}$$

where m_{c_prod} and m_{c_air} are the amount of mass of combustion products and air, respectively, present in the chamber at any given time. Therefore the species' mass-composition in the chamber can be represented as:

$$\frac{m_{c\_prod}}{m_c}\underbrace{\left(3CO_2 + 4H_2O + 18.8N_2\right)}_{\text{Combustion Products}} + \frac{m_{c\_air}}{m_c}\underbrace{\left(O_2 + 3.76N\ \right)}_{\text{Fresh Air}} \tag{3.16}$$

Since m_{c_prod} and m_{c_air} are complementary, it suffices to find an expression for only one. For convenience, let us denote the partial masses from Equation (3.16) as:

$$\begin{aligned} \delta_1 &= \frac{m_{c\_prod}}{m_c} \\ \delta_2 &= \frac{m_{c\_air}}{m_c} \end{aligned} \tag{3.17}$$

Furthermore, the rates of change of concentration mass of each species in the chamber can be described as:

$$\dot{m}_{c\_prod} = \left(\dot{m}_{c\_prod}\right)_{in} - \left(\dot{m}_{c\_prod}\right)_{out} \tag{3.18}$$

$$\dot{m}_{c\_air} = \left(\dot{m}_{c\_air}\right)_{in} - \left(\dot{m}_{c\_air}\right)_{out} \tag{3.19}$$

where the subscripts $_{in}$ and $_{out}$ denote inward in outward flow, respectively. Since no concentration of combustion products will ever enter the chamber through the breathe-in check valve, Equation (3.18) can be simplified as

$$\dot{m}_{c\_prod} = -\left(\dot{m}_{c\_prod}\right)_{out} \tag{3.20}$$

Assuming that the outward mass flow rate of each species is proportional to its concentration in the chamber at any time t, the following relationship is obtained:

$$\left(\dot{m}_{c\_prod}\right)_{out} = \left[\frac{m_{c\_prod}(t)}{m_c(t)}\right]\dot{m}_2 \tag{3.21}$$

Finally, substituting Equation (3.21) into Equation (3.20), we get the following first order differential equation:

$$\dot{m}_{c\_prod} = -\left[\frac{\dot{m}_2(t)}{m_c(t)}\right]m_{c\_prod}(t) \tag{3.22}$$

whose initial condition is $m_{c\_prod}(t_0) = m_{c0}$, since the initial mass composition in the chamber consists purely of combustion products. Equation (3.22) can be calculated in simulation as the values of $\dot{m}_2(t)$ and $m_c(t)$ change. Consequently, values for Equation (3.17) can be obtained in real-time, and gas constants c_{p_c} and c_{v_c} (and therefore γ_c and R_c) are calculated from molecular weight averages and average specific heats

3.0.2 Expansion and Pump Chambers

The expansion chamber is modeled with two one-way mass flows: $\dot{m}_2$ inward (combustion valve) and $\dot{m}_3$ outward (exhaust valve). Applying Equations (3.5-3.6), and assuming that combustion products as the only substance present, the dynamic pressure and temperature functions are given by:

$$\dot{P}_e = \frac{(\gamma_{prod} - 1)(\dot{m}_2 c_{p_{prod}} T_c - \dot{m}_3 c_{p_{prod}} T_e) + (\gamma_{prod} - 1)\dot{Q}_e - \gamma_{prod} P_e \dot{V}_e}{V_e} \tag{3.23}$$

$$\dot{T}_e = \frac{\dot{m}_2 (c_{p_{prod}} T_c - c_{v_{prod}} T_e) - \dot{m}_3 R_e T_e + \dot{Q}_e - P_e \dot{V}_e}{m_e c_{v_{prod}}} \tag{3.24}$$

Similarly, for the pump chamber we have:

$$\dot{P}_p = \frac{(\gamma_{air} - 1)(\dot{m}_4 c_{p_{air}} T_{amb} - \dot{m}_5 c_{p_{air}} T_p) + (\gamma_{air} - 1)\dot{Q}_p - \gamma_{air} P_p \dot{V}_p}{V_p} \tag{3.25}$$

$$\dot{T}_p = \frac{\dot{m}_4 (c_{p_{air}} T_{amb} - c_{v_{air}} T_p) - \dot{m}_5 R_{air} T_p + \dot{Q}_p - P_p \dot{V}_p}{m_p c_{v_{air}}} \tag{3.26}$$

3.0.3 Combustion Valve

Since the combustion valve has dynamic characteristics that influence its flow area, it has to be properly modeled so that Equation (3.7) can be computed in real-time. Figure 3-2 shows a free-body diagram of this valve.

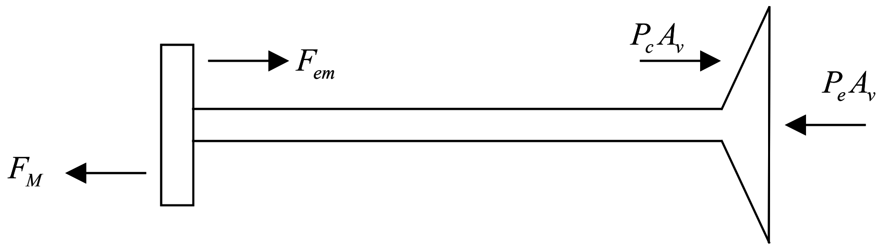

Figure 3-2: Free-Body Diagram of Combustion Valve.

Therefore, applying Newton's second law, the valve dynamics are thus given:

$$m\ddot{x}_v = P_c A_v + F_{em} - F_M - P_e A_v \tag{3.27}$$

where m is the mass of the valve, x_v is the position of the valve, F_{em} and F_M are the magnetic forces generated by the electromagnet and permanent magnet, respectively, and A_v is the cross-sectional area of the valve head. Furthermore, the valve flow area $a_2(x_v)$ can be described by the following:

$$a_2(x_v) = \min\{2\pi r_v x_v\ ,\ \pi(r_v^{\ 2} - r_{stem}^{\ \ 2})\} \tag{3.28}$$

where r_v and r_{stem} are the radii of the valve head and valve stem, respectively.

3.0.4 Inertial Dynamics

Finally, the dynamics given by the liquid piston are modeled by the following differential equation:

$$\ddot{V}_e = \frac{1}{M}\left[\left(P_e - P_p\right)A^2 - kV_e - b\dot{V}_e + kV_{e\_rlx}\right] \tag{3.29}$$

where V_e is the volume in the expansion side, A is the cross-sectional area of the liquid-piston, b is the effective viscous friction assumed for a 50% overshoot, and V_{e_rlx}, recall, is the "relaxed" volume in the expansion chamber, when the diaphragms are unstretched.

3.1 Simulation

A dynamic simulation was carried out using SIMULINK, with the model presented, and using most of the physical parameters shown in Table 2-1. Some non-idealities that were not considered in Chapter II are accounted for in this Simulation. Most notably, these are frictional losses caused by viscous damping in the liquid-piston and losses caused by assuming a dead volume in the pump chamber, which is almost inevitable due to pressure fittings, check valves, etc. This dead volume has been greatly reduced from previous designs, however, and further design choices can minimize it further.

The simulation algorithm consists of one complete cycle, starting at the instant immediately after ignition, whereupon an initial condition of "instant" high pressure and high temperature in the combustion chamber are assumed. Similarly, it ends at the instant where the liquid-piston completes the return stroke. All valves are modeled as "check-valves", with specified flow conditions.

A full set of plots will first be showed for a "nominal" scenario – that is – one that exhibits a reasonably desired performance with design parameters. To account for the aforementioned non-idealities, the yield combustion temperature was increased from 50% to 52%. Additionally, to account for the additional stiffness provided by the compressed air in the pump dead volume (assumed at 1 cc), the diaphragms' spring constant was lowered to 1000 N/m, in order to maintain the desired dynamic behavior of the piston.

After presenting the "nominal" scenario, an analysis will be performed where certain design parameters are changed one at a time and their effect on power and efficiency investigated.

3.1.1 Nominal Scenario

Figures 3-3 through 3-7 show plots of a complete cycle of the simulated FLPC. Figure 3-3 shows the pressures in the combustion, expansion and pump chambers. It can be seen that the pressure in the combustion chamber starts at around 2.7 MPa and expands out all the way out to atmospheric pressure (over-expansion) in under 5 milliseconds. Since the pressure in the expansion chamber begins at atmospheric pressure, it takes about 1 millisecond to catch up with the combustion pressure, at which point they become equal for the remainder of the stroke. With regard to the pressure in the pump chamber, it can be seen that at around 3 milliseconds it reaches the supply pressure and begins to pump, hence a horizontal line at around 650 kPa. Similarly, Figure 3-4 shows the temperatures in these chambers, and it can be seen that although they reach peaks of near 1200 K, they quickly come down to manageable temperatures. The elastomeric diaphragms that will be used have temperature ratings of up to 750 K, and as can be seen from Figure 3-4, the temperature in the expansion chamber settles at around 620 K. Furthermore, since this simulation assumed no heat losses, these temperatures will be lower in reality. It should also be noted that at around 4 milliseconds, the temperature in the combustion chamber quickly drops to near ambient temperature due to breathe-in.

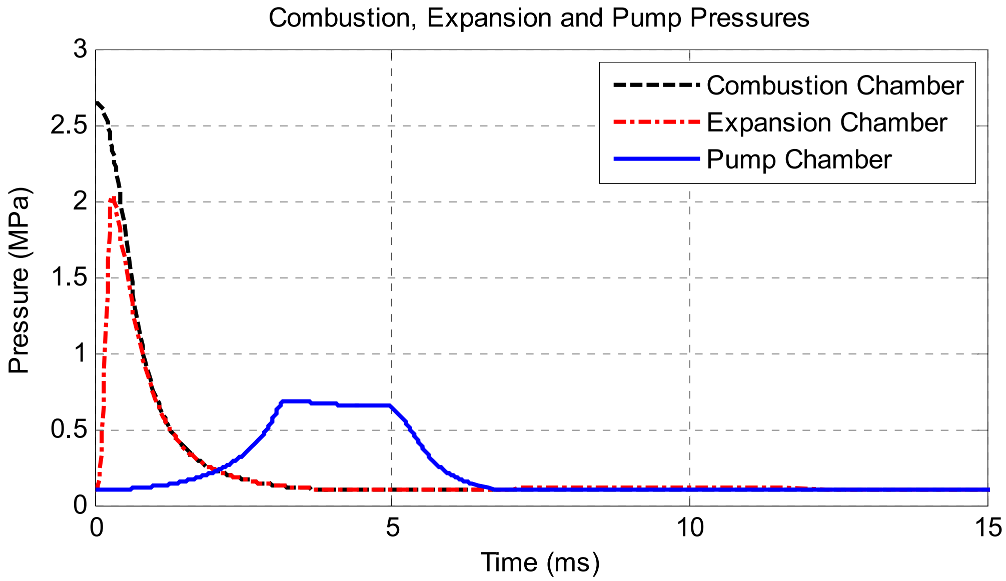

Figure 3-3: Simulated Pressure Signals.

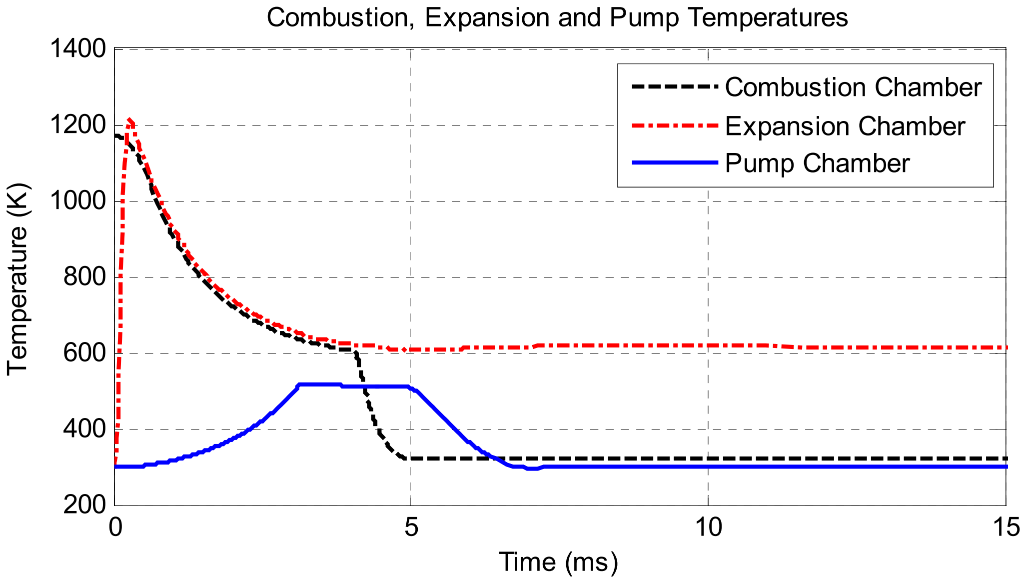

Figure 3-4: Simulated Temperature Signals.

Figure 3-5 shows the displacement of the liquid piston. It is plotted in a different time-scale since its dynamics are slower than those of combustion. It is shown that the selected passive dynamics are capable of returning the piston all the way back and fully exhausting the combustion products. This plot also demonstrates that the desired device frequency can be higher than the passive dynamics' natural frequency, since the combustion gases expand so quickly and the passive dynamics of the piston are only responsible to carry out half of the cycle, which is also relatively fast due to the extra spring element provided by the compressed air in the pump dead volume. This is an important realization because it reveals that the power capability of the FLPC can be much higher than anticipated: Based on the cycle timeline shown in Figure 3-5 it can be seen that the device could theoretically operate at up to 50 Hz.

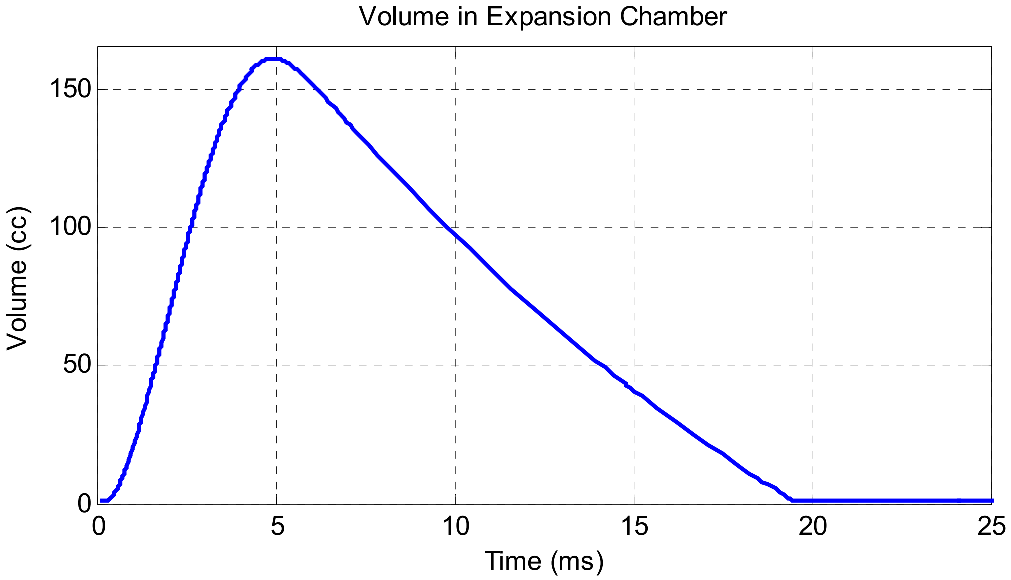

Figure 3-5: Simulated Displacement of Liquid Piston.

Figures 3-6 and 3-7 show the mass flow rates through all five valves. They are separated into two plots to show adequate resolution in terms of time-scale and amplitude, since some of the valve flow rates are roughly an order of magnitude higher than others. Figure 3-6 shows the mass flow rates through the combustion and pump outlet valves. It is plotted in the same time-scale as Figures 3-3 and 3-4, so that it is easy to see the relationships between pressures, temperatures and these larger flows. Similarly, Figure 3-7 is plotted in the same time-scale as Figure 3-5. Breathe-in can be seen in both Figures 3-6 and 3-7 by a "bump" in the combustion and breathe-in valves at around 4 milliseconds. Also, it should be mentioned that the area under the pump outlet mass flow rate signal (Figure 3-6) represents the amount of air that was pumped into the air reservoir. Therefore, this integrated signal will be used to estimate the overall efficiency and power output of the device.

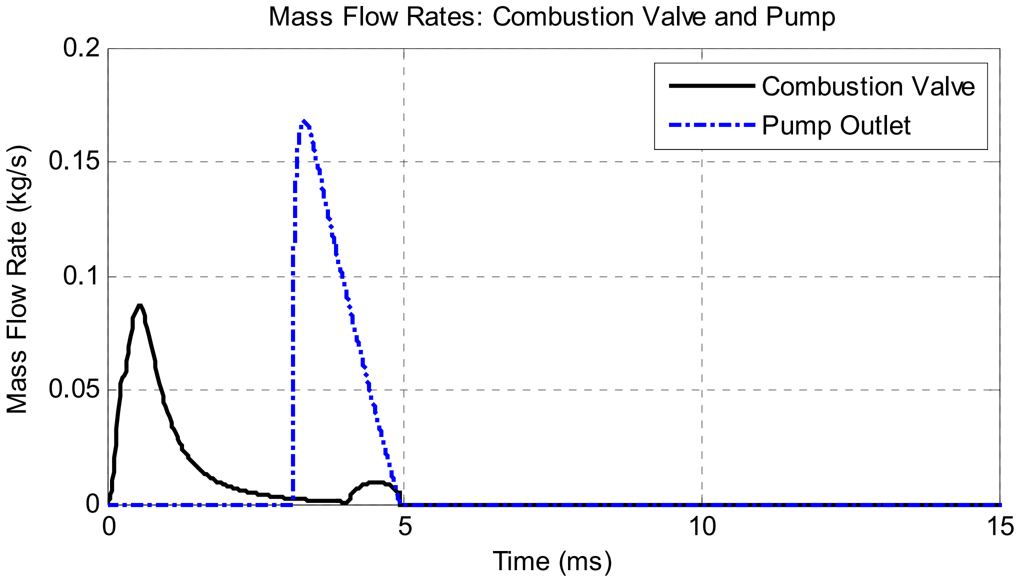

Figure 3-6: Simulated Mass Flow Rates Through Combustion and Pump Outlet Valves.

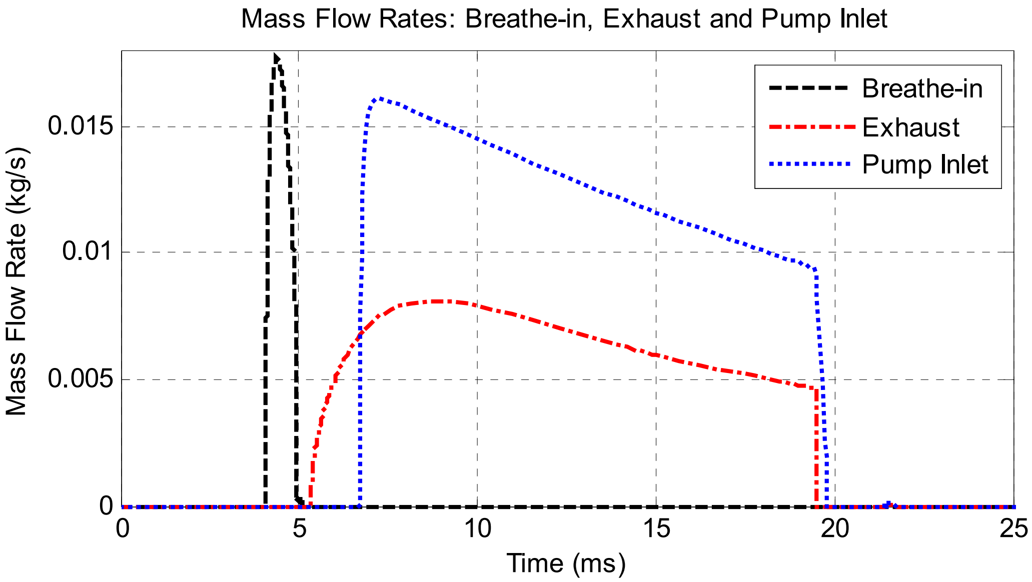

Figure 3-7: Simulated Mass Flow Rates Through Breathe-in, Exhaust and Pump Inlet Valves.

Simulated power delivery was obtained by integrating the pump outlet mass flow rate signal and applying Equations (2.11) and (2.12). The total mass of air pumped into the reservoir in a single stroke was computed as 0.165 g, while the mass needed for reinvestment (for the subsequent injection phase) is 0.0838 g (assuming stoichiometric mixture at 653 kPa injection pressure). This gives a net energy transfer of 7.226 Joules, which divided over the cycle period (19.4 ms) yields a maximum net power output of 372 Watts.

Simulated overall efficiency was calculated as per Equation 2.15. Given that the mass of air/fuel mixture injection is 0.089 g, the overall efficiency is obtained as 2.91 %.

3.1.2 Sensitivity to Parameter Variation

In addition to analyzing and presenting the "nominal" case scenario, we want to explore the system's sensitivity to important design parameters, in particular piston mass, diaphragm spring constant, and dead volume in the pump chamber. This is done so that we can gain some insight useful for future experimental troubleshooting.

Sensitivity to Mass and Spring Constant

Figure 3-8 shows a simulated plot of output power and overall system efficiency as a function of piston mass, with otherwise "nominal" conditions. It can be seen that the trade-off between power and efficiency is not too disconcerting, though a steep roll-off in both power and efficiency can be seen at around $m = 0.2\,\mathrm{kg}$. This can be attributed to two main reasons, both of which have to do with scaling: firstly, for very light masses, viscous damping effects begin to dominate over inertial characteristics; secondly, and most importantly, lighter masses decrease the timescale of each stroke, thus increasing the required volumetric flow rates through the valves (in particular pump outlet, pump inlet, and exhaust valves). When the mass is too light and the stroke too fast, the flow through the valves becomes choked and the piston dynamics heavily damped, resulting in energy losses. As seen in Figure 3-8, these losses become very dominant in our device if the liquid piston is lighter than 0.2 kg. This is a very important realization because in a way it *quantifies* the inertial loading attribute of the free piston compressor. In addition, this should become a crucial factor in the design methodology for future FPC devices.

Also from Figure 3-8, the power plot peaks at low masses because of the high attainable frequencies. From the figure it can be assessed that an adequate range of mass is between 0.4-0.8 kg, and that increasing the mass beyond that will result mostly in lower power densities.

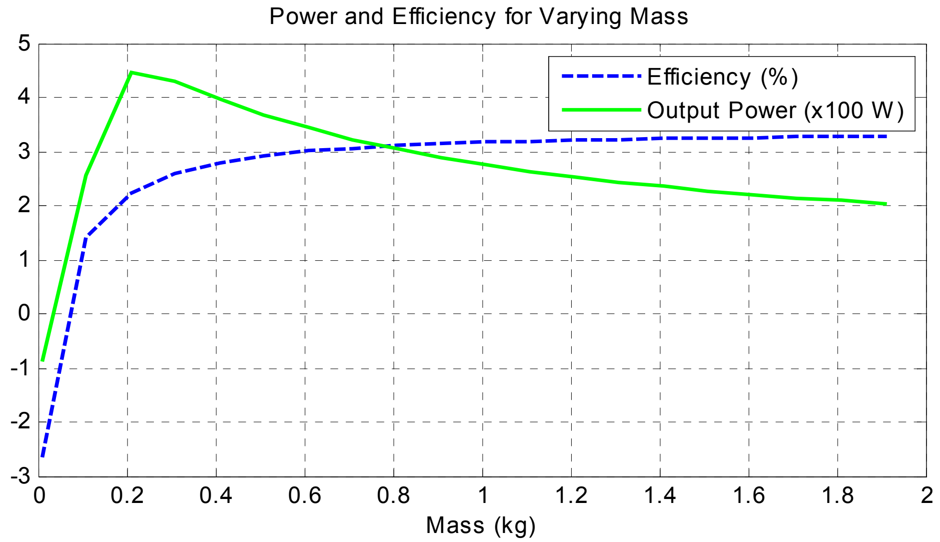

Figure 3-8: Simulated Power and Efficiency Versus Varying Mass

Likewise, Figure 3-9 shows a simulated plot of output power and overall system efficiency versus diaphragm spring constant k, with all other parameters at their nominal values. A steady drop in efficiency can be seen for increasing values of k, while the output power exhibits a nearly exponential rise. Lower output powers corresponding to decreasing values of k are attributed to lower operational frequencies associated to lower stiffness; whereas higher efficiencies at low values of k can be explained by 1) decreased viscous damping resulting from slower liquid-piston motion, and 2) lower spring potential energy that needs to be overcome in order to complete a stroke. From a design perspective, this plot suggests that if a 0.5-kilogram liquid-piston is to be used, an adequate spring constant should be somewhere between 400-1000 N/m.

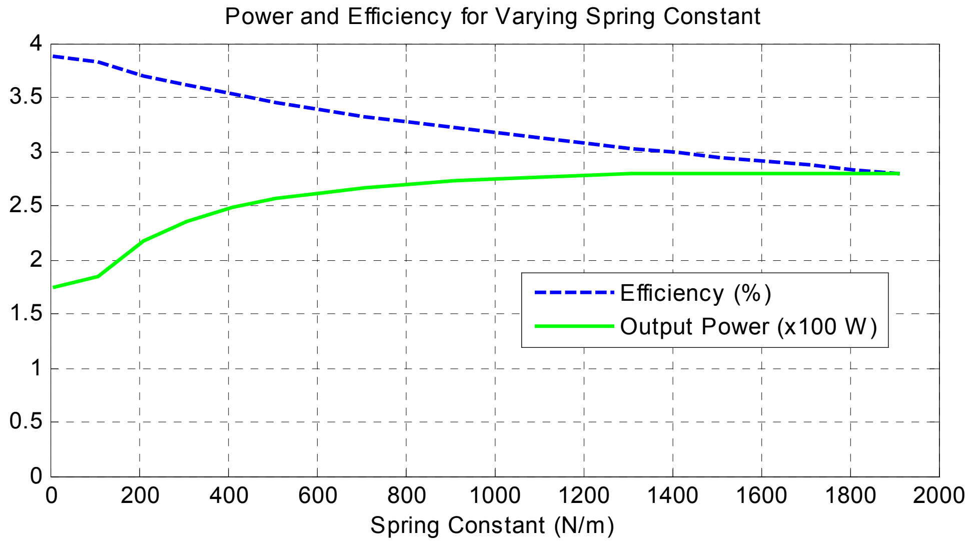

Figure 3-9: Simulated Power and Efficiency Versus
Varying Diaphragm Spring Constant

Since Figures 3-8 and 3-9 present cases where one of the two parameters is locked at a nominal value, 3-dimensional plots are needed to evaluate cases for multiple combinations of liquid-piston mass and spring constant. Figures 3-10 and 3-11 show simulated 3-dimensional plots for overall system efficiency and output power, respectively, as functions of combinations of M and k for values between $M = [0.01, 1.91]\,\text{kg}$ and $k = [10, 1910]\,\text{N/m}$, in 0.1-kg and 100-N/m intervals of mass and spring constant, respectively. It can be seen from Figure 3-10 that the system efficiency enjoys a vast plateau for most of its *k-M* zone, slightly rising towards smaller spring constants, and with a general roll-off at masses lower than 0.25 kg. The more interesting Figure 3-11 shows a general decline in power for lower spring constants, and a power peak at 0.2-kg mass.

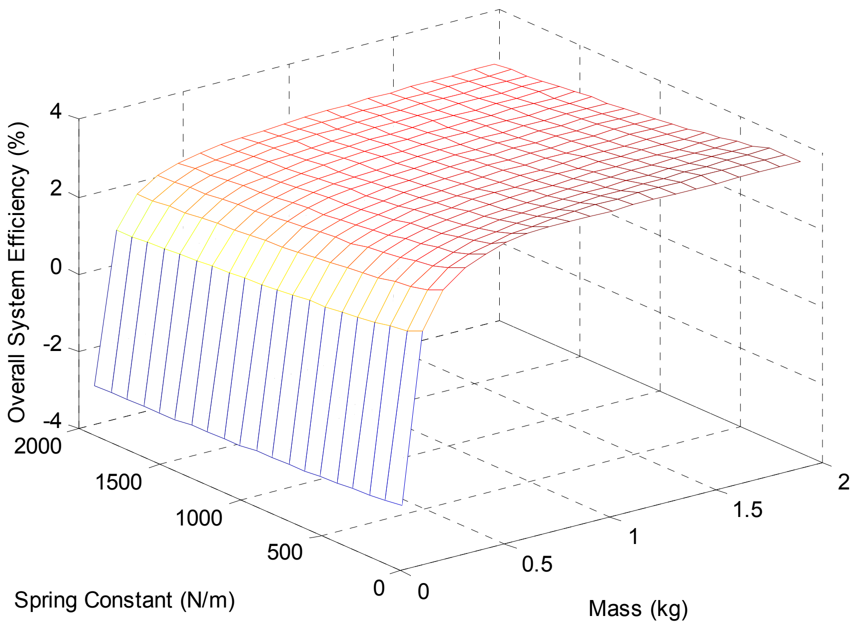

Figure 3-10: Simulated Efficiency versus Mass and Spring Constant

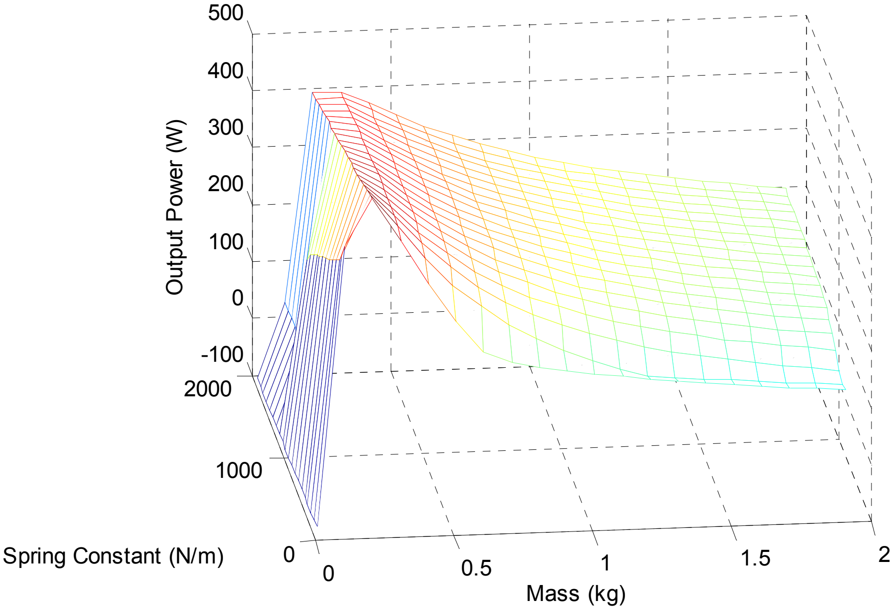

Figure 3-11: Simulated Power versus Mass and Spring Constant

Sensitivity to Dead Volume in Pump Chamber

Figure 3-12 shows a simulated plot of output power and overall system efficiency versus dead volume in the pump chamber, for dead volume values of 0 to 10 cubic centimeters. It can be seen that the efficiency has a slow, steady decline for increasing values of dead volume, while the power output remains mostly unaffected. The sensitivity to this parameters is relatively low in this device mostly because the displacement volume is very large in comparison. However, minimizing this volume is still very important since a small increase in system efficiency can result in great energetic gains. A slight, almost negligible drop in power at low dead volumes is due to the fact that as more air is squeezed out of the pump chamber, less compressed air is left to act as a spring element for the liquid-piston return stroke. A slight drop in power at higher dead volumes is simply due to less net energy being delivered to the reservoir.

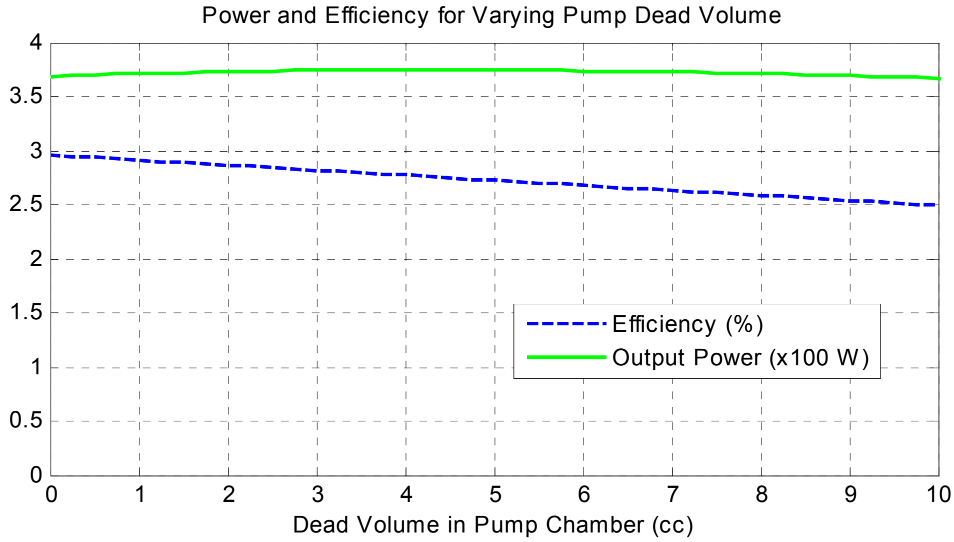

Figure 3-12: Simulated Power and Efficiency Versus

Dead Volume in Pump Chamber

Energy Domains

Figure 3-13 shows a simulated plot containing the time-based energy storage throughout every relevant energetic domain, as a function of simulation time. It starts with pneumatic potential energy of combustion gases (which has already suffered nearly a 75% energy loss from chemically stored energy of the injected fuel, due to the conservatively assumed low combustion temperature plus engine cycle inefficiencies), and ends with pneumatic potential energy in the reservoir. The total energy contained in the system at any given time can be grasped by drawing a vertical line anywhere along the time axis and adding up the values of all the intersecting points. Furthermore, the "dynamic" efficiency of each process could be assessed by analyzing the evolution of this sum throughout the timeline. The drop in the "reservoir" signal is attributed to the re-investment of air for the next injection event. The plot was cut at 10 milliseconds to show adequate resolution, though it should be noted that the return stroke continues until near 20 milliseconds, hence the red line indicating some kinetic energy left in the liquid-piston at 10 milliseconds. It should also be noticed from the figure that both the kinetic energy of the combustion valve and the elastic potential energy of the diaphragms are too small to be seen qualitatively in this scale. This indicates that their role within the main energy transduction is negligible.

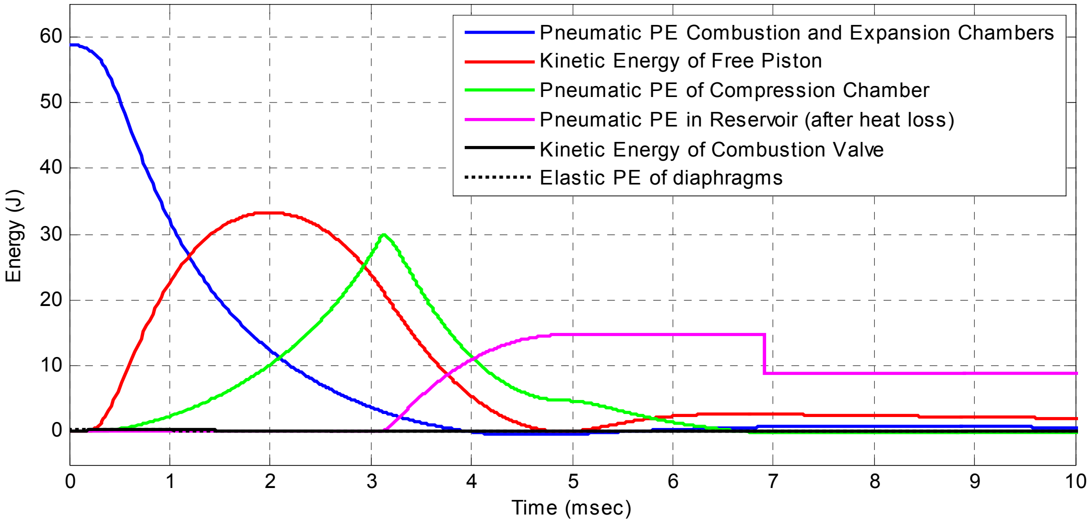

Figure 3-13: Energy Storage as a Function of Time

Plotting the energy domains as in Figure 3-13 can be a very useful tool to evaluate the overall system performance in terms of most of its conceptual features. Over-expansion of the combustion products can be seen by the complete drop of the "combustion" signal, and furthermore, breathe-in is acknowledged by the fact that there is kinetic energy left in the piston afterwards. The "reservoir" signal can quickly tell us how much air, if any, was pumped into the reservoir. It is also shown that the energy losses associated with opening the combustion valve and overcoming the diaphragms' stiffness are essentially negligible. But most importantly it can be seen, as proof of concept, that the inertial loading becomes a dominant energy carrier, as is shown at around 2 milliseconds. It is evident, just from looking at this figure, that it is mostly the inertial loading that contributes directly to both the compression and pumping work.

CHAPTER IV

FABRICATION AND EXPERIMENTAL ARRANGEMENT OF FREE LIQUID-PISTON COMPRESSOR

4.0 Fabrication Overview

The FLPC was fabricated at Vanderbilt as per Figure 2-5. The assembly, shown in Figure 4-1, consists of 6 main components (from right to left): The two rightmost are the reservoir and the pump chamber (which almost seem as one single component, since their interface has no external flanges). The next component is the fluid chamber, which can be seen between the blue elastomeric diaphragms. To the left of the fluid chamber is a component which contains the expansion chamber on its right side and half of the combustion chamber on its left side. The next component contains the other half of the combustion chamber on its right side, a valve guide through its middle, and a press-fit electromagnet on its left side. Finally, the leftmost component is an end cap containing a Neodymium-Iron-Boron (NdFeB) magnet, with a magnet position-adjusting screw which can be seen in the picture.

The overall length of the whole device (including the air reservoir) is just under 50 centimeters, and its overall weight (including the fluid) is around 2.5 kg. Both these dimensions can be reduced once higher frequencies undergo testing, by reducing the mass of the fluid and thus the length of the fluid chamber. Similarly, an eventual application device (as opposed to this research prototype) could be further optimized in terms of weight by reducing wall thicknesses and other tolerances.

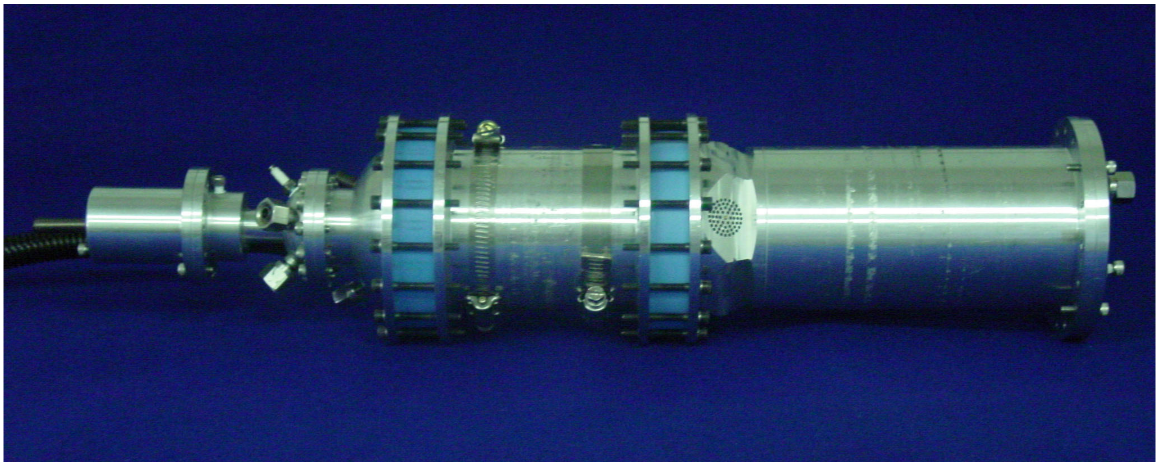

Figure 4-1: Fabricated FLPC Assembly.

4.1 Pump Chamber and Reservoir

The hemispherical pump chamber was ported for inward and outward flow and pressure sensing. In order to minimize dead volumes and flow restrictions, custom low-profile inlet and outlet check valves were implemented by using thin silicone rubber membranes covering clusters of small holes. Figures 4-2a and 4-2b show a Pro/ENGINEER model of the pump chamber and its exposed check-valve orifices, and Figures 4-3a and 4-3b show the fabricated component with membranes covering the orifices, thus promoting passive one-way flow. As can be seen in Figure 4-3b, the pump "outlet" check valve was reinforced with stiff foam pressed by a metal plate. The position of this plate can be adjusted by the turn of a screw, providing variable force to the membrane. This allows us to stiffen the check valve as desired, in order to properly tune it for optimal flow characteristics, given the trade-off between the dynamic response time of the valve and its flow restriction. In particular, its dynamic response time should be barely fast enough (or "stiff" enough) to minimize or altogether avoid backflow at the end of the pump stroke; however, too much stiffness can result in severe flow restrictions as the pumping stroke would find a reduced effective flow area through it.

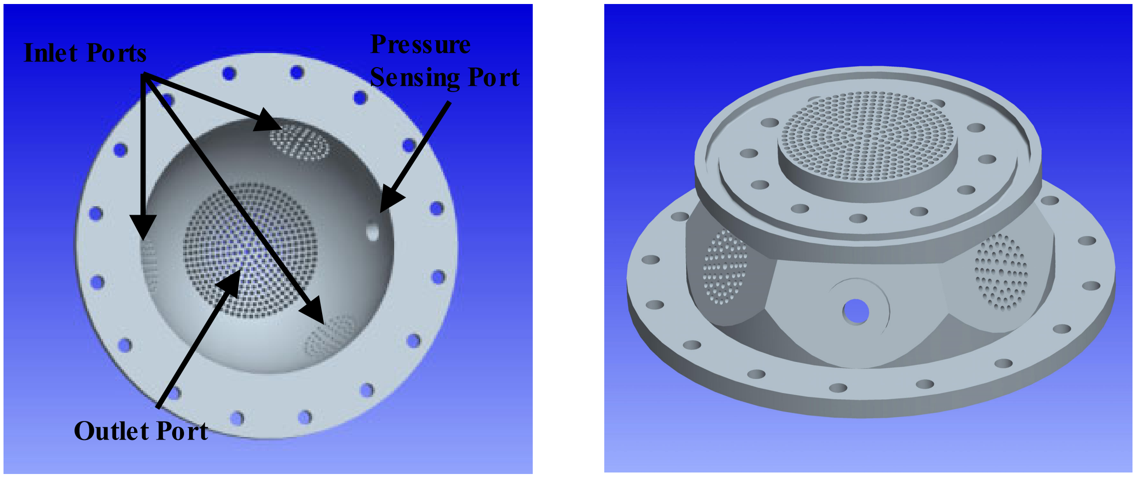

(a) (b)

Figure 4-2: Pro/ENGINEER Drawing of Pump Chamber, Inside (a) and Outside (b).

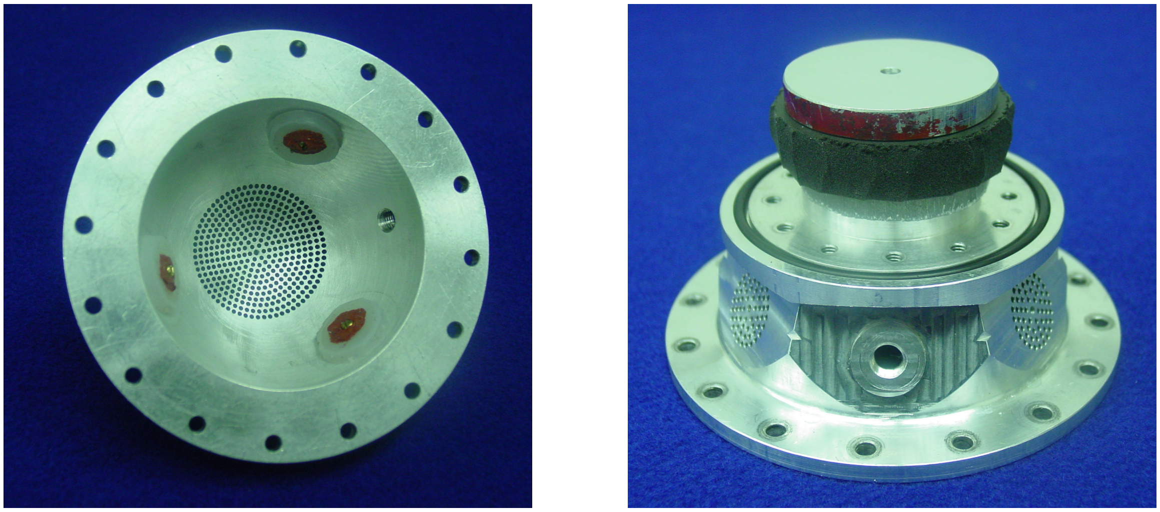

(a) (b)

Figure 4-3: Fabricated Pump Chamber With Integrated Check Valves, Inside (a) and Outside (b).

Figure 4-4 shows the pump chamber and the reservoir assembled together, viewed through the reservoir (with its lid removed). The pump outlet flow port can be seen exposed (Figure 4-4a) and covered with the foam-reinforced check valve (Figure 4-4b)

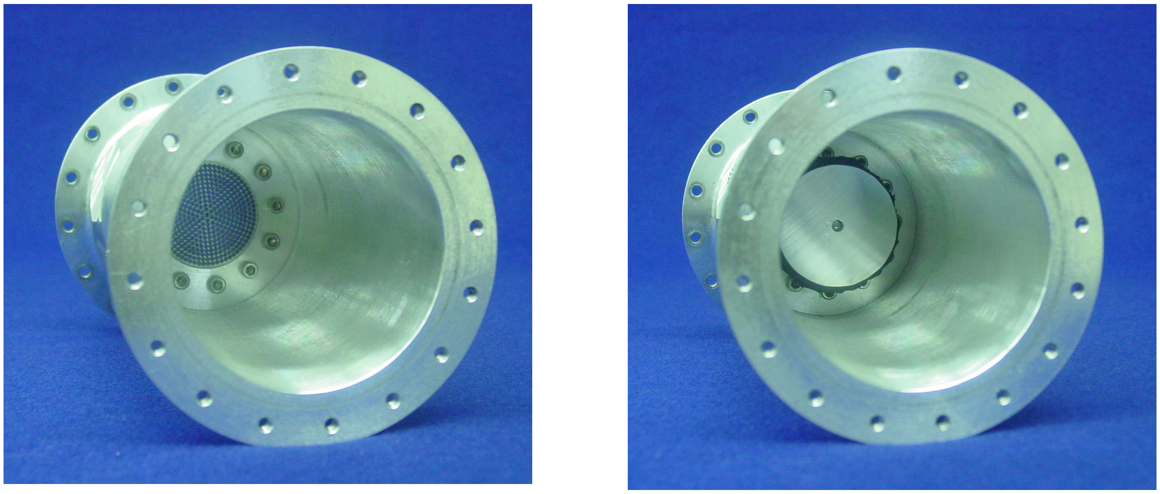

(a) (b)

Figure 4-4: Assembled Pump with Reservoir, Showing Outlet Flow Port: Uncovered (a) and Covered to Form a Check Valve (b).

4.2 Fluid Chamber and Diaphragms

The fluid chamber is essentially a hollow tube sized to contain 0.5 kg of water. Figure 4-5 shows two pictures of the fluid chamber containing water trapped between elastic rubber diaphragms. The rings shown clamping the diaphragms were fabricated for display purposes only. The diaphragms were custom-made with Smooth-On® liquid rubber, which consists of a two-part solution that cures into rubber with a desired durometer when mixed together. It was desired to have a very flexible rubber (i.e., low durometer) to trap the water slug, with a stiffer rubber (i.e., high durometer) around the clamping circumference, in order to avoid too much volume-displacement of the rubber material when subject to a clamping force. Since silicone rubbers can cure onto themselves, two different rubber mixtures with different durometers were used: Shore A 00-30 (white) for the elastic center, and shore A 50 (blue) for the "hard" circumference. Their thickness was selected at approximately 2 centimeters, thick enough to withstand hard collisions without rupturing. A close-up of these diaphragms is shown in Figure 4-6.

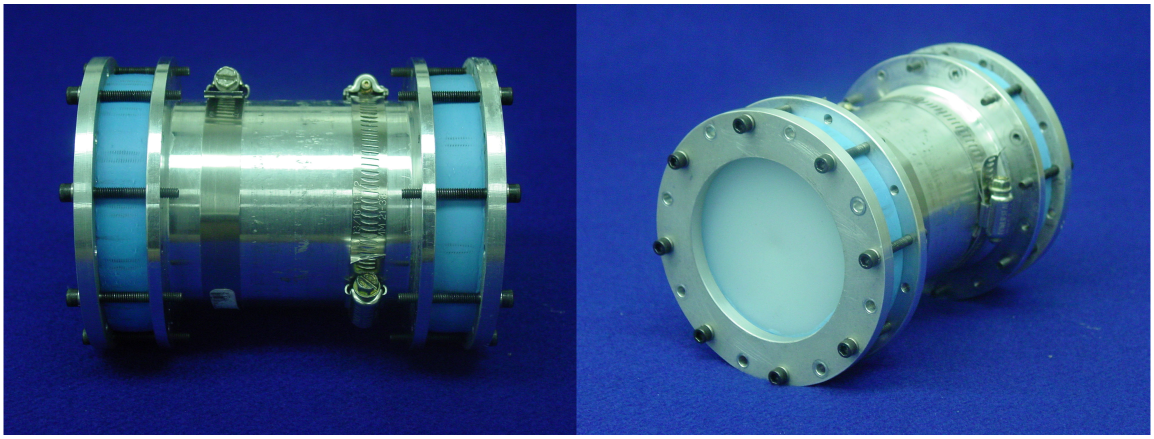

Figure 4-5: Fabricated Fluid Chamber With Liquid-Piston
Trapped Between Thick Diaphragms.

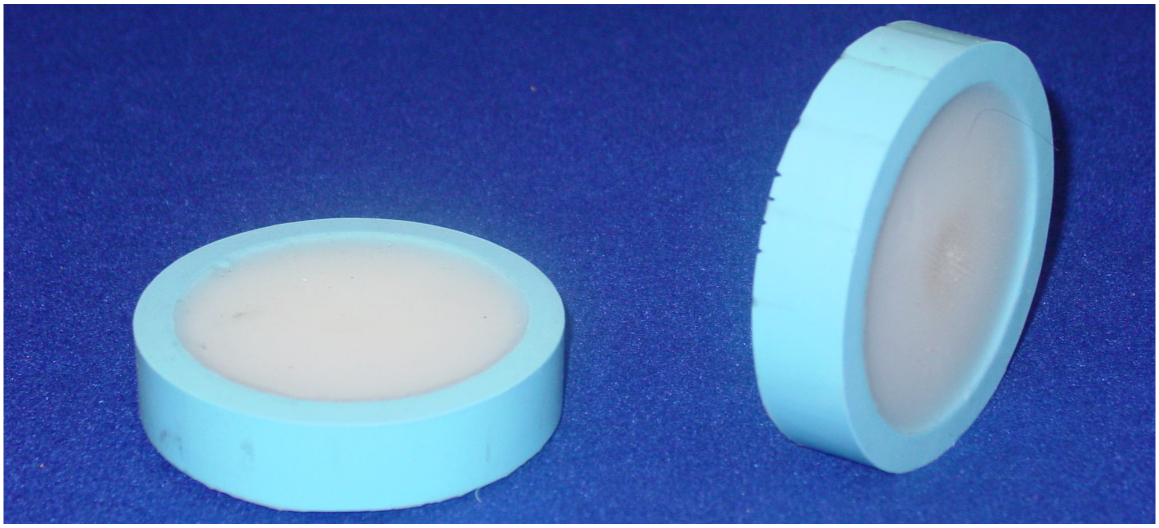

Figure 4-6: Custom-molded Rubber Diaphragms

4.3 Combustion Side

The "separated" combustion chamber was designed and fabricated as a sphere to minimize the surface area to volume ratio and its associated heat loss. For ease of fabrication, it was split into two hemispheres. Figure 4-7 shows a transparent drawing of the combustion side assembly. The combustion valve can be seen in its retracted position, where the permanent magnet in the back pulls it shut. An automotive valve was selected with its set of guide and seat. The seat was press fit between the expansion chamber and the combustion chamber, and machined at a local head shop to obtain the proper contact angles. This procedure is shown in Figure 4-8.

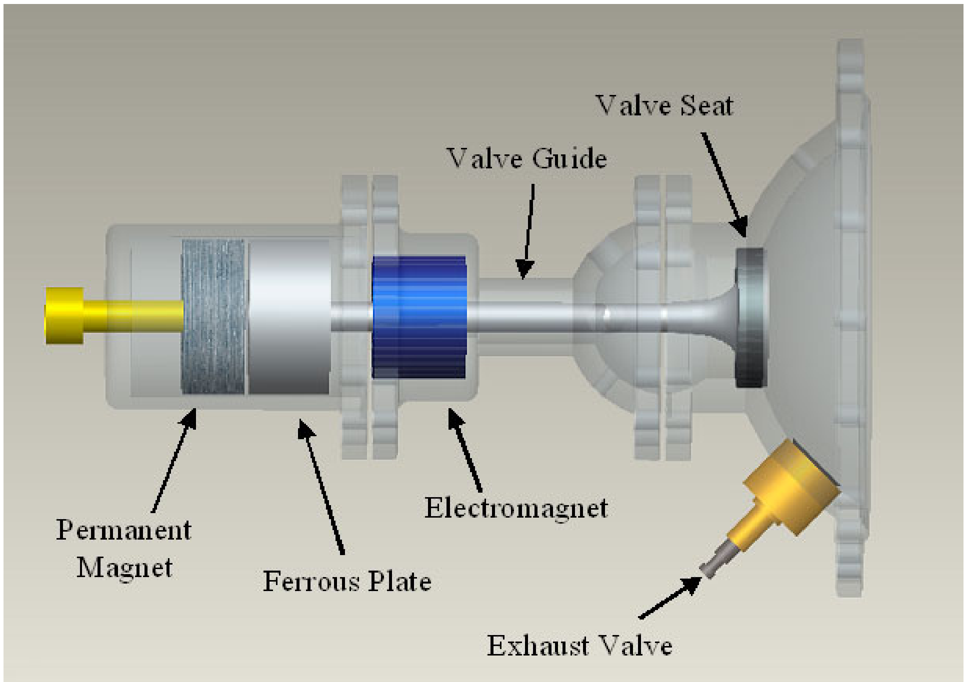

Figure 4-7: Drawing of Combustion Chamber Assembly.

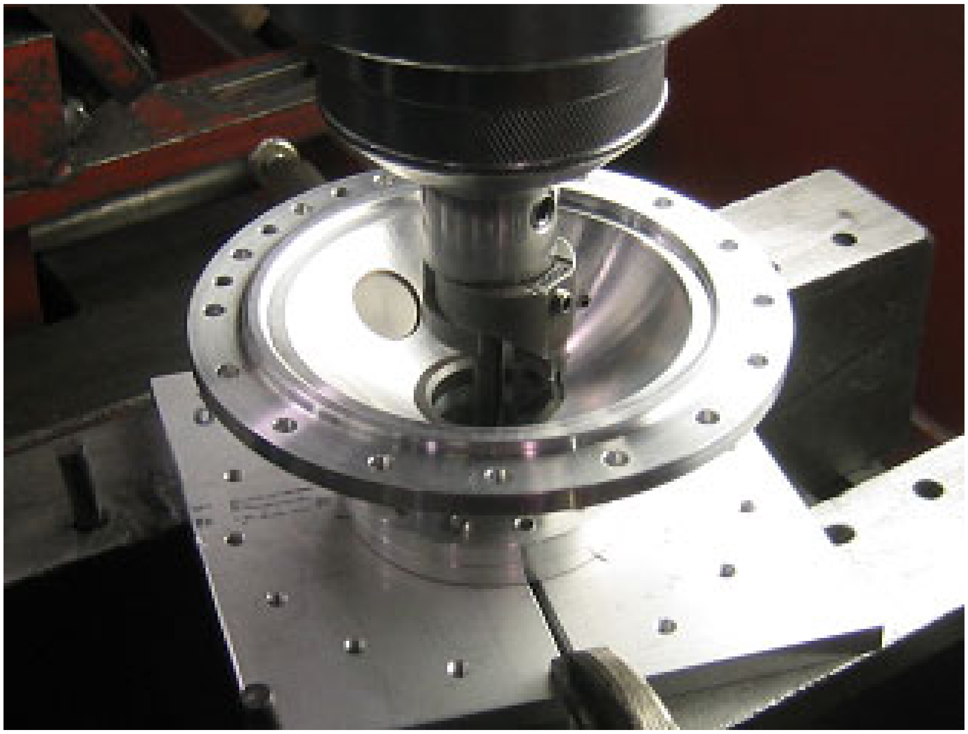

Figure 4-8: Cutting the Valve Seat.

Similarly, referring back to Figure 4-7, a valve guide was press fit to the left of the combustion chamber, to maintain proper valve alignment. As can be seen in Figure 4-9, the guide protrudes into the combustion chamber. This was a design choice needed due to length constraints, since the guide has an OEM nominal length. The radius of the combustion chamber was therefore adjusted before fabrication to account for an otherwise loss of volume. Since the combustion chamber was split into two components, an o-ring groove was carved on one of the mating surfaces to provide sealing. Also shown in Figure 4-9 are the press-fit guide and seat for the exhaust valve, taken from an RC engine, and a miniature spark pug, obtained from an independent RC enthusiast. Similarly, Figure 4-10 shows the combustion chamber assembly next to the fluid chamber. The combustion valve head can be seen shut while the exhaust valve is seen open.

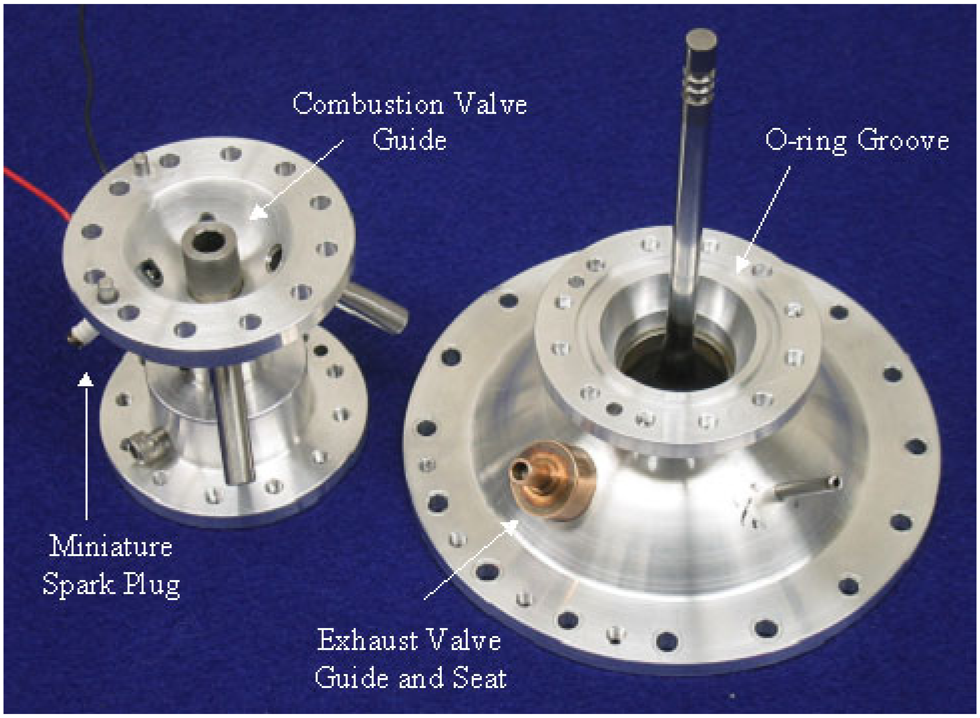

Figure 4-9: Constituents of Combustion Chamber.

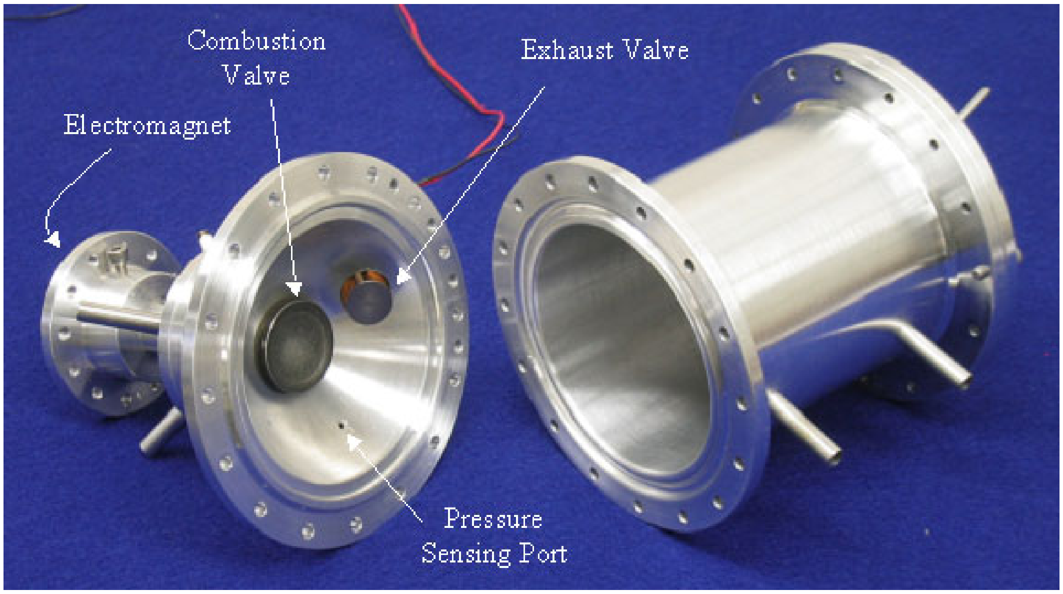

Figure 4-10: Combustion and Expansion Chambers (left) and Fluid Chamber (right).

Also shown in Figure 4-10 is the location of the press-fit electromagnet, which is 1 inch in diameter and has been bored out to make room for free sliding of the valve stem. Figure 4-11 shows a picture of this component.

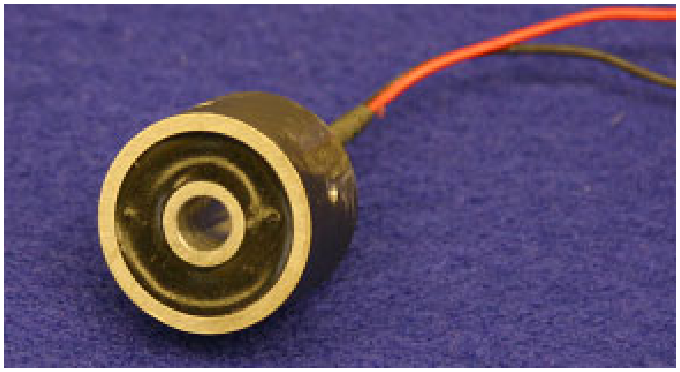

Figure 4-11: Electromagnet.

In order to attach a ferrous plate to the valve (i.e., one that will respond to magnetic fields), the OEM valve keepers were used and a round ferrous plate designed to attach to them. Similarly, keepers were used in the RC exhaust valve to attach a return spring. Figures 4-12 and 4-13 show both valves with their keepers detached and attached, respectively, and Figures 4-14 and 4-15 show these in their mounted configuration. Note that Figure 4-14 also shows the implemented exhaust solenoid and its mount.

Figure 4-12: Detached Valve Keepers

Figure 4-13: Attached Valve Keepers

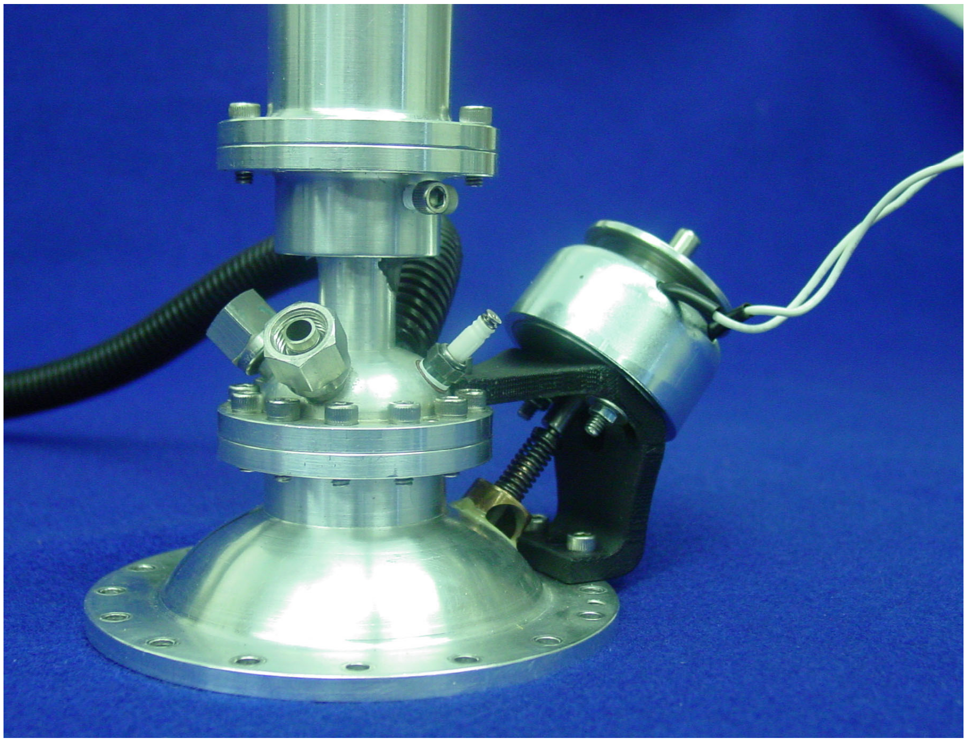

Figure 4-14: Exhaust Valve with Actuating Solenoid

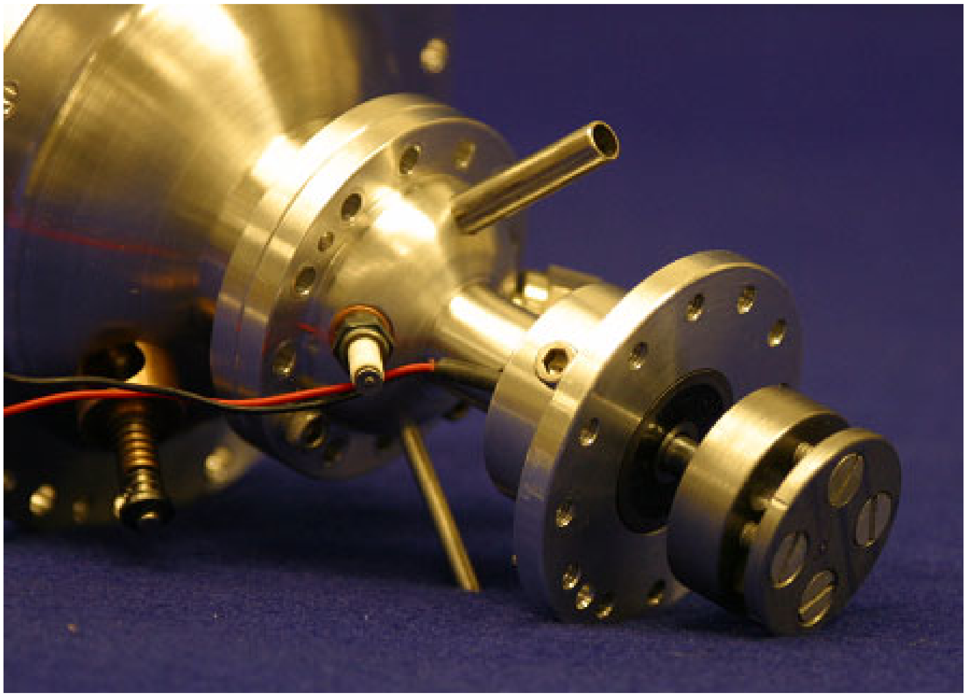

Figure 4-15: Implemented Combustion Valve Keeper. Note the Press-fit Electromagnet

Finally, the end cap, which covers the moving valve-keeper assembly, contains a neodymium-iron-boron magnet that pulls the combustion valve shut during injection. This mate also has a sealing o-ring in case there is any high-pressure leakage through the valve guide. Figure 4-16 shows a picture of this end cap containing the magnet, and Figure 4-17 shows a picture of the magnet.

Figure 4-16: End Cap with Magnet

Figure 4-17:Neodymium-Iron-Boron Magnet

In addition to the press-fit components described (exhaust valve seat, combustion valve seat, combustion valve guide and electromagnet), both the combustion and expansion chambers are ported for pressure sensing. Furthermore, the combustion chamber is ported for intake, breathe-in, pressure sensing, and spark plug.

4.4 Experimental Arrangement

Air/Fuel Injection

For preliminary experimental assessment, the air used for injection comes from an external supply, whereas the fuel source is a 0.5-kg bottle of Coleman® propane, which at room temperature has a vapor pressure of about 1 MPa (140 psig) [21]. In addition to injection pressure, there are two essential criteria that must be met in order to achieve proper combustion: 1) mixture quantity, in terms of having a near stoichiometric mass ratio of air-to-fuel (15.63 for propane); and 2) mixture quality, in terms of proper mixing of the two substances. Finally, from a systems-level perspective, the injection process has to be fast enough to comply with the desired operational frequency of the device. In the previous design by Riofrio and Barth [19], the flow of air and propane was each controlled by a Parker® Series-9 on/off valve. These valves would allow each substance to enter a relatively large mixture line, which was internally rugged to create turbulence, and hence proper mixing. Trial and error determined the appropriate opening time duration for each valve, so that a nearly stoichiometric ratio was achieved. These valves have a nominal response time of 12 milliseconds, and their opening time durations were between 8-12 milliseconds for the fuel valve and 50-80 milliseconds for the air valve. The low resolution of the fuel valve, combined with slight variations of its response time resulted in frequent firing inconsistencies. Figure 4-18 shows a schematic of this arrangement.

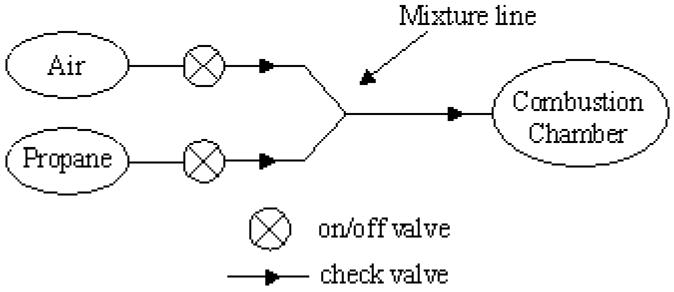

Figure 4-18: Fuel Injection Scheme of Previous FPC.

With this previous configuration, air/fuel injection took up as much as 100 milliseconds. For the new FLPC, however, it is desired to have a much faster fuel injection scheme. Recall that since the "separated" combustion chamber decouples the fuel injection from the liquid-piston dynamics, the potential to achieve higher frequencies will depend on the slowest of these two. Furthermore, simulation demonstrated that the FLPC can achieve much higher frequencies than those dictated solely by the mass-spring passive dynamics.

A simpler and more effective fuel injection scheme has been implemented, with achieved injection durations as short as 20 milliseconds. Its operational principle is as follows: air and fuel are streamed into a common mixture line, at the end of which there is an on/off valve that allows a pressurized mixture into the combustion chamber. For adequate air/fuel mixture quantity, properly adjusted metering valves placed in both the air and fuel lines maintain the fuel flow smaller than the air flow, such that this flow difference yields stoichiometric air-to-fuel ratio into the mixture line at all times. Figure

4-19 shows a schematic of this new configuration, and Figure 4-20 shows a picture of the Parker® Series-9 on/off valve and the Parker® HR-Series metering valve.

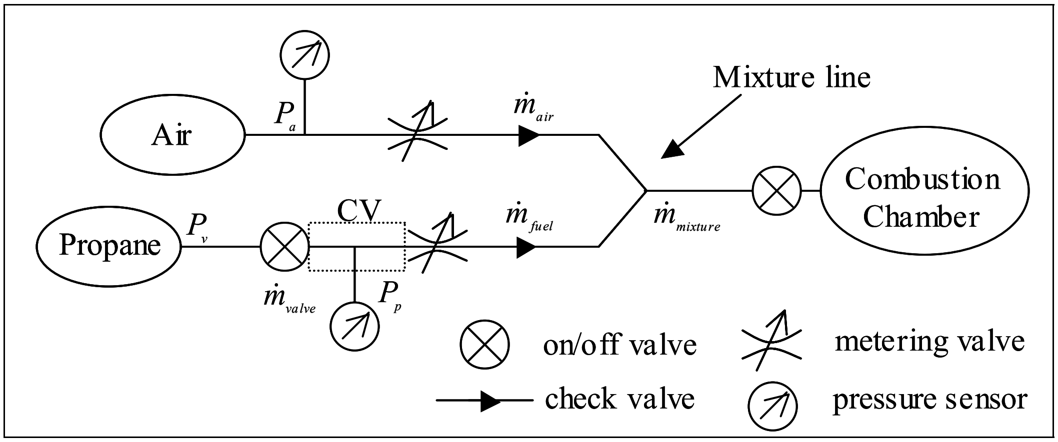

Figure 4-19: Schematic of New Fuel Injection Configuration

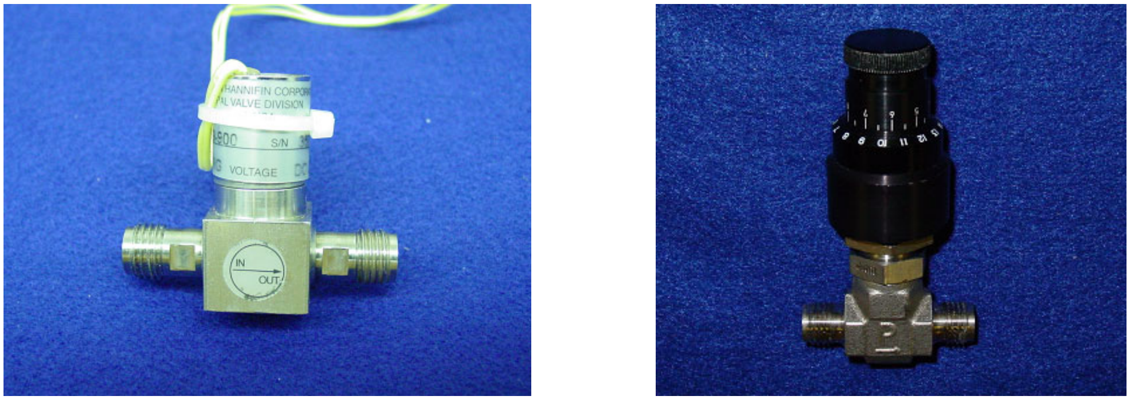

(a) (b)

Figure 4-20: Parker® Series-9 valve (a) and HR-Series Metering Valve (b)

From Figure 4-19, $\dot{m}_{air}$, $\dot{m}_{valve}$, $\dot{m}_{fuel}$, and $\dot{m}_{mixture}$ are the mass flow rates through the air line, propane on/off valve, propane metering valve, and mixture line, respectively, and P_a, P_v and P_p are the air pressure, vapor pressure of propane, and regulated propane pressure, respectively. Since the vapor pressure of propane is much higher than the target injection pressure, a simple feedback control loop was implemented so that the upstream propane pressure (i.e., in the control volume, as defined by dashed space in Figure 4-19) is the same as the air pressure. Essentially, this fuel pressure regulator looks at the pressure in the pre-mixture air line, and regulates the pressure in the control volume (CV) by controlling an on/off valve between the propane bottle (at high vapor pressure) and the CV. The mass flow rate through the metering valve, $\dot{m}_{fuel}$ essentially constitutes a disturbance in the loop, since pressure dynamics in the control volume depend on the net mass flow rate. Figure 4-21 shows the block diagram of this pressure regulator.

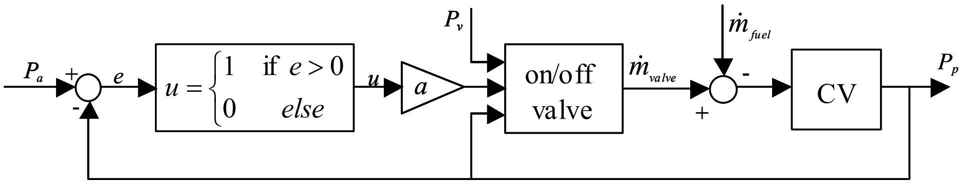

Figure 4-21: Block Diagram of Propane Pressure Regulator.

Recalling from Equation (3.7), the mass flow rate through a valve can be characterized by the following expression:

$$\dot{m} = a\psi(P_u, P_d) \tag{4.1}$$

where a is the effective cross-sectional flow area of the valve orifice, and $\psi(P_u, P_d)$ is a nonlinear function of upstream and downstream pressures across the valve, and its discharge coefficient. Furthermore, the mass flow rates through the air and propane lines can be related in the following way:

$$\dot{m}_{mixture} = \dot{m}_{air} + \dot{m}_{fuel} \tag{4.2}$$

To achieve a stoichiometric ratio in the air/fuel mixture, the following condition must be met:

$$\frac{\dot{m}_{air}}{\dot{m}_{fuel}} = 15.63 \tag{4.3}$$

Combining Equations (4.1) and (4.3), and noting that by virtue of the fuel pressure regulator the upstream and downstream pressures are the same for both the air and fuel lines, we obtain:

$$\frac{\dot{m}_{air}}{\dot{m}_{fuel}} = \frac{a_{air}}{a_{fuel}} = 15.63 \tag{4.4}$$

This demonstrates that the mass flow-ratio between the air and propane are dependent only on the ratio of their effective flow areas. Therefore, provided that the air and fuel lines have equal upstream and downstream pressures, a properly adjusted metering valve in the fuel line suffices in order to achieve a continuous stoichiometric air-to-fuel ratio.

Ignition

Ignition is carried out with a traditional coil and spark plug. Miniature ignition components (ignition coil, spark plug and spark plug cable) were acquired from an independent RC enthusiast, and proved to be very adequate for our application. A computer-signaled transistor induces a current through the primary wire in the coil, and is suddenly stopped after a very short duration of time. This "instantaneous" current drop in the primary wire (which results in a sudden change in the magnetic field) induces a very high voltage in the much longer secondary coil, which is finally discharged across the spark plug gap. A 6-volt battery powers the small coil, and an opto-isolator separates the computer input signaling from the high-current coil circuit. Figure 4-22 (below) shows a picture of the ignition components, and Figure 4-23 (next page) shows a picture of the experimental arrangement of the fuel injection and ignition scheme.

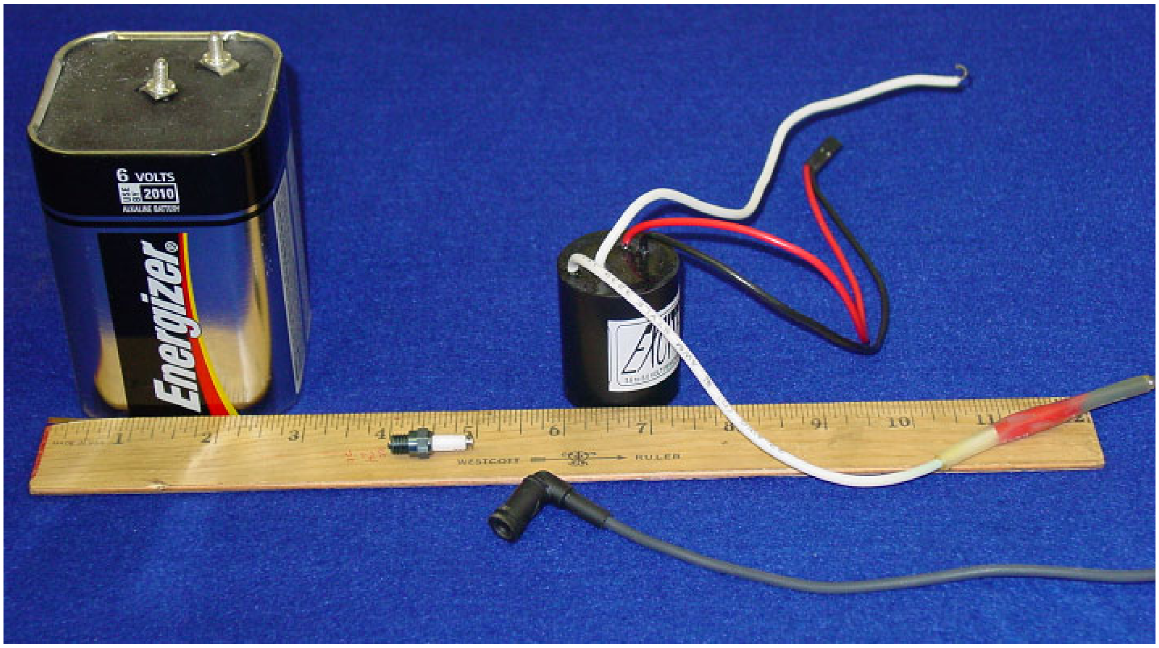

Figure 4-22: Ignition Components: Battery, Coil, Spark Plug and Cable

Instrumentation

Omega® pressure sensors are used for the expansion and pump chambers, while a combustion-specific high-pressure Optrand® sensor is used in the combustion chamber. For adequate resolution, the sensors in the expansion and pump chambers are rated for pressures in the 0 to 1.4 MPa range (0-200 psi), while the combustion pressure sensor can read up to 6.9 MPa (1000 psi).

External electrical supply is provided for pressure sensors, exhaust solenoid, on/off valves, electromagnet (if needed), and analog signal conditioners and operational amplifiers. Similarly, external supply of compressed air is used for various experimental testing, though an eventual finalized FLPC would use all the air it needs directly from its reservoir. Finally, Matlab's Simulink is used for signal controlling, interfaced with the FLPC through a National Instruments NI 6024E A/D data acquisition card.

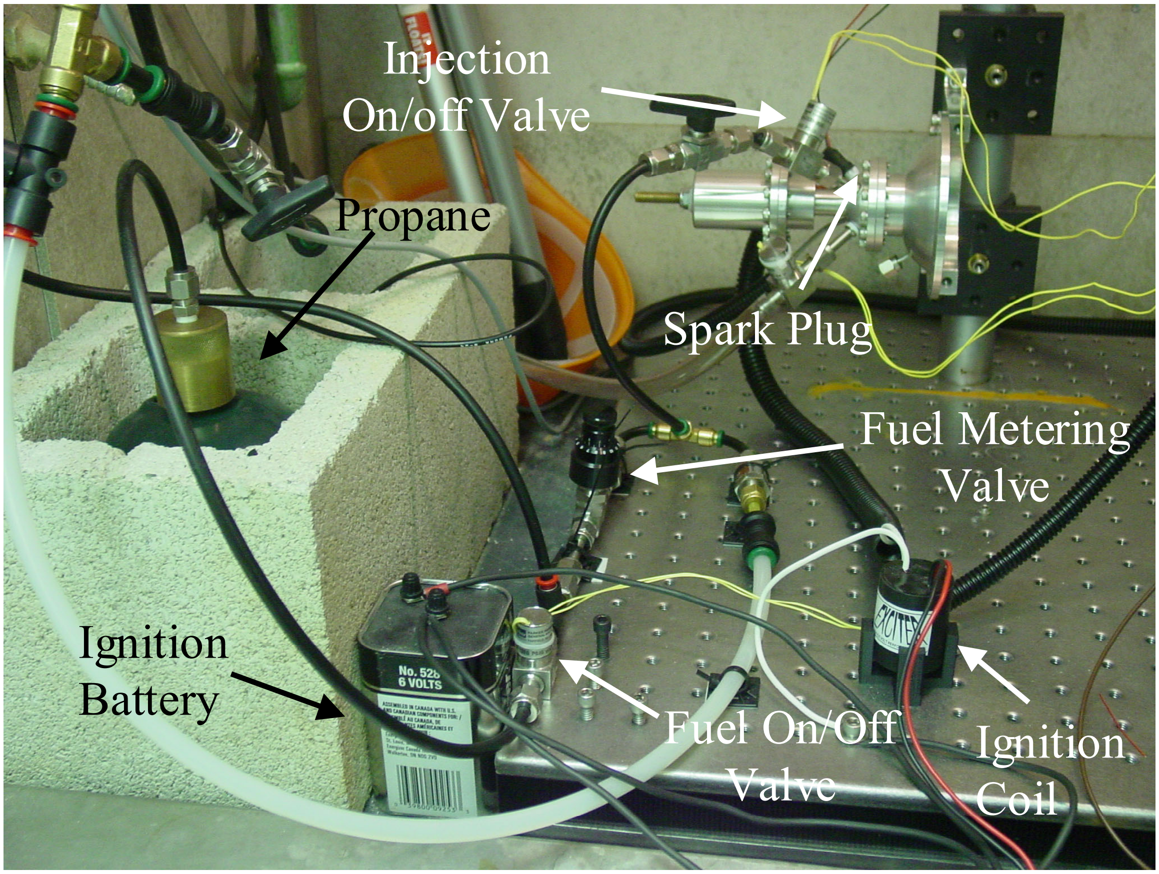

Figure 4-23: Experimental Arrangement of Fuel Injection and Ignition

A fully instrumented experimental FPLC is shown in Figure 4-24, with most pressure sensors and on/off valves visible.

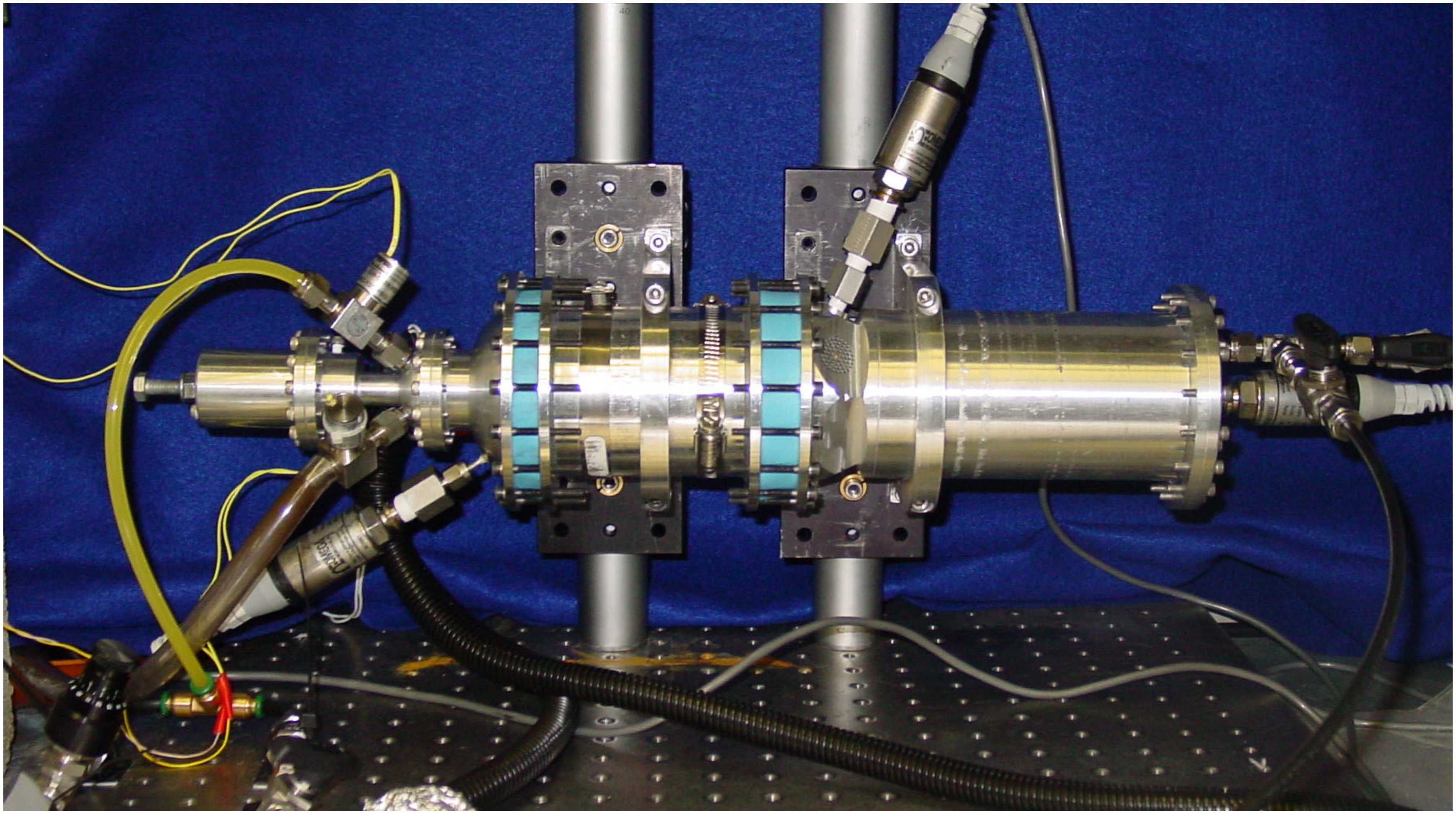

Figure 4-24: Fully Instrumented Experimental FPLC Prototype

CHAPTER V

EXPERIMENTAL RESULTS AND MODEL VALIDATION

5.0 Combustion Scheme Validation

The first series of experiments consisted of careful validation of the principle of operation of the combustion scheme. The first immediate concern was to ensure that the combustion valve being held shut by the magnet could provide adequate sealing at the valve seat. This was tested by injecting pure air into the combustion chamber at the maximum target injection pressure of 650 kPa (around 80 psig). After proper tuning of the magnet adjustment screw, minimal leakage through the valve was observed. The fuel injection scheme presented in Chapter IV was then implemented, and the air and fuel metering valves were adjusted by trial and error until optimal combustion was achieved ("optimal" in relative terms of repeatability and yielded combustion pressures).

The next concern involved valve behavior. It was desired for the combustion valve to "throw" open immediately upon combustion, and stay open (ideally by its own dynamic response) long enough to allow for the pressure in the combustion chamber to vent all the way down to atmospheric pressure. To verify and measure this, a series of "open combustion" tests was undertaken, in which the fluid chamber, compressor and reservoir were removed. No actuated exhaust would be necessary in this configuration since the combustion products leaving the combustion chamber would go directly into the atmosphere as soon as the combustion valve opens. Figure 5-1 shows a picture of this experimental configuration.

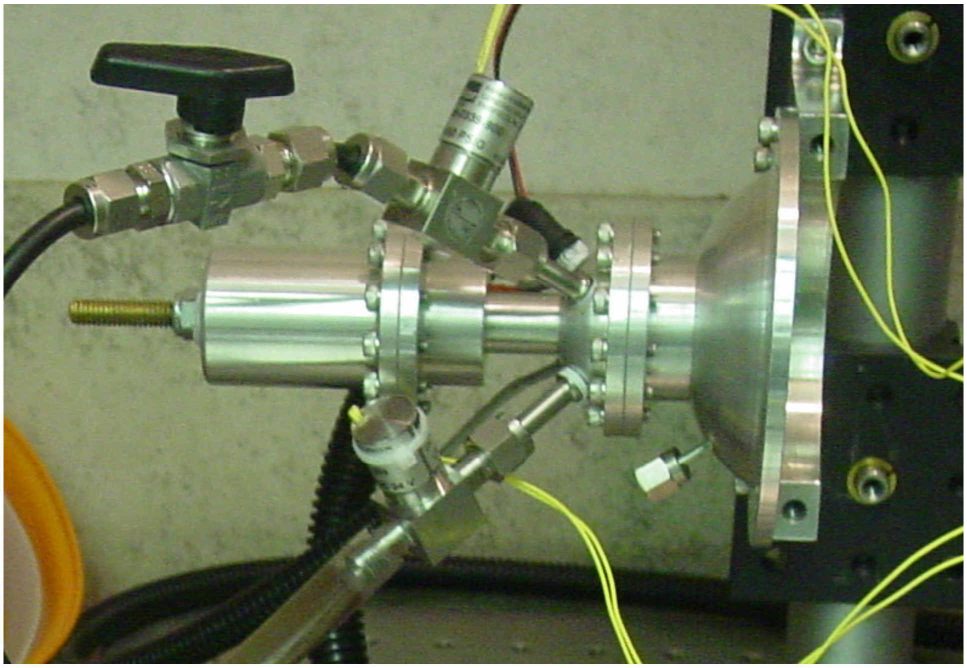

Figure 5-1: Open Combustion Arrangement.

For the open combustion tests, the air used for the injection mixture was provided directly from the wall, regulated at any desired pressure. This would allow us to test the combustion scheme for a wide array of injection pressures, determined by some combination of air supply pressure and injection valve opening duration. A second on/off valve was added to the combustion chamber as a temporary exhaust valve, primarily used to exhaust pressurized mixtures in the event of a misfire, which typically happens a few times before the first successful firing, since the proper air/fuel mixture needs to travel through the mixture line before entering the combustion chamber. Given the length of the mixture line, this typically takes 5 to 10 cycles on a settled engine ("settled" in terms of having had some elapsed time after the last series of firings). After this typical transient period of misfirings, continuous consistent combustion cycles are achieved. Figure 5-2 shows an experimental plot of a typical combustion cycle, displayed in terms of recorded pressure in the combustion chamber. For this combustion cycle, the air from the wall was regulated at 653 kPa (80 psig), and the air/fuel injection valve was commanded to open for 30 milliseconds. As a result, the achieved injection pressure was around 550 kPa (65 psig). The pressure signal in Figure 5-2 clearly shows the 30-millisecond injection, and, immediately after spark, the combustion peak. Once the combustion valve begins to open, the pressure quickly drops as the combustion gases vent through the valve orifice. Note that the time axis is modified such that $t = 0$ coincides with the instant of spark.

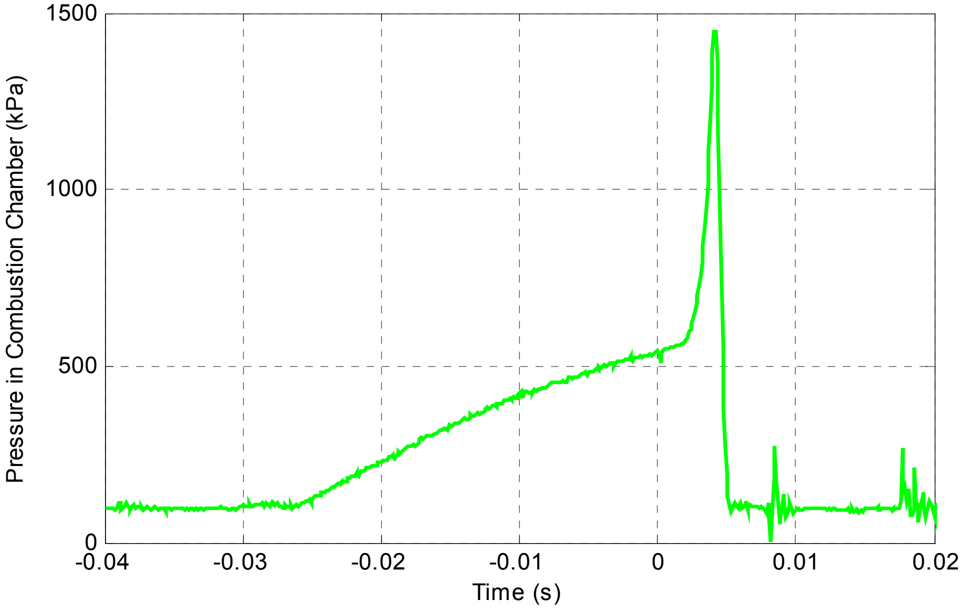

Figure 5-2: Typical Combustion Cycle.

Since the injection and combustion spike portions of the graph in Figure 5-2 are not included in the model shown in Chapter III (recall that our model starts with instantaneous high pressure in the combustion chamber), a recently developed combustion model by Yong et al [23] can be appended to our dynamic model in order to obtain a full "open combustion" simulation. Experimental data can then be used to fully validate the model. Yong's combustion model is based on the "rate at which heat is released by combustion in the combustion chamber," which is given by:

$$\dot{Q}_c = e\dot{m}_{cc} \tag{5.1}$$

where m_{cc} is the mass of the combustion products (which is zero at the instant of spark and increases thereon) and ϵ, recall, is the specific energy density of the air/fuel mixture computed from the lower heating value of the fuel, as specified in Equation (2.17). Combining Equation (5.1) with the reaction rate of the combustion process (a first-order process, as given by the well-accepted Arrhenius Law) and a spatial flame-propagation process (also assumed first order), a second-order model can be derived. From a systems dynamics perspective, this model contains an effective damping ratio and natural frequency. As per Yong's method, this model represents the overall heat release rate of combustion:

$$\ddot{Q}_c = E_c\tau_c^2 - 2\xi\tau_c\dot{Q}_c - \tau_c^2 Q_c \tag{5.2}$$

where E_c is the total initial energy contained in the air/fuel mixture, ξ is the effective damping ratio of the reaction process, and τ_c is a temperature-dependent natural frequency from Arrhenius Law given by:

$$\tau_c = Ke^{-E_a/R_cT_c} \tag{5.3}$$

where K is a constant pre-exponential factor, E_a is the effective activation energy (modeled as a constant lumped parameter), R_c is the average gas constant in the combustion chamber, and T_c is the varying temperature in the combustion chamber. The values of the constants E_a and K, found at wide ranges in the literature, may account for unmeasurable factors such as irregular combustion geometries, irregularities and impurities in the air/fuel mixture, heat losses through the combustion walls, leakage, and perhaps other unknown phenomena that, for practical purposes, can be lumped together.

In order to apply this combustion model to the FLPC, the constants E_a and K are tuned empirically so that a set value of these constants can result in adequate matching between the model and the experimentally obtained data for any given injection pressure. Finally, Yong's model also includes an additional input to the combustion chamber for the fuel injection pressure dynamics, consisting of a constant upstream pressure and an on/off valve modeled based on our Parker injection valve. Thus, the fuel injection pressure dynamics can easily be captured, and included in an "open combustion" simulation. Figure 5-3 shows the same open combustion data from Figure 5-2, along with the properly calibrated simulated data, which combines Yong's combustion model with our dynamic model.

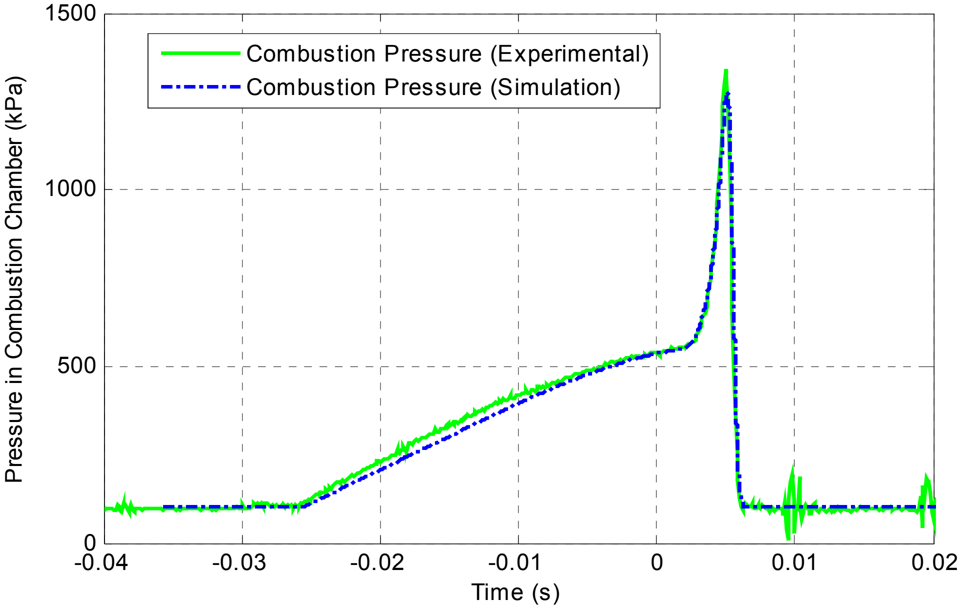

Figure 5-3: Open Combustion Model Validation.

It should be noted that the heat release dynamics model described by Equation (5.2) is mostly concerned with the pressure rise characteristics from the instant of spark until the "peak" combustion value, but not with the value of the peak itself. This peak is rather best defined by the holding capacity of the magnet, which was also adjusted in the model based on empirical observations.

5.1 Combustion Valve Model Validation

It is desirable to obtain experimental displacement data for the combustion valve in order to further validate its model (Equations 3.27 and 3.28). A Polytec® OFV 511 laser interferometer was used for this purpose, aimed directly at the combustion valve head during "open combustion". The laser signal from the interferometer is conditioned by a Polytec® OFV 2200 vibrometer controller, and then sent to MATLAB and converted to units of displacement. To show the valve displacement data in the appropriate context, open combustion data sets are shown in Figures 5-4 through 5-6, which include pressure in the combustion chamber and combustion valve displacement, both simulated and experimentally obtained. Each figure shows a data set for a different air supply pressure (which essentially results in different injection pressures). Figures 5-4, 5-5 and 5-6 correspond to air supply pressures of 653 kPa (80 psig), 515 kPa (60 psig) and 419 kPa (46 psig), respectively. As can be seen in the Figures, these supply pressures yield injection pressures of 545 kPa (64.3 psig) 435 kPa (48.3 psig) and 350 kPa (36 psig), respectively. It should be restated that the values of the constants from Equation (5.3) were only calibrated once, and used for all scenarios in model validation. All time axes were again modified such that zero corresponds to the instant of spark.

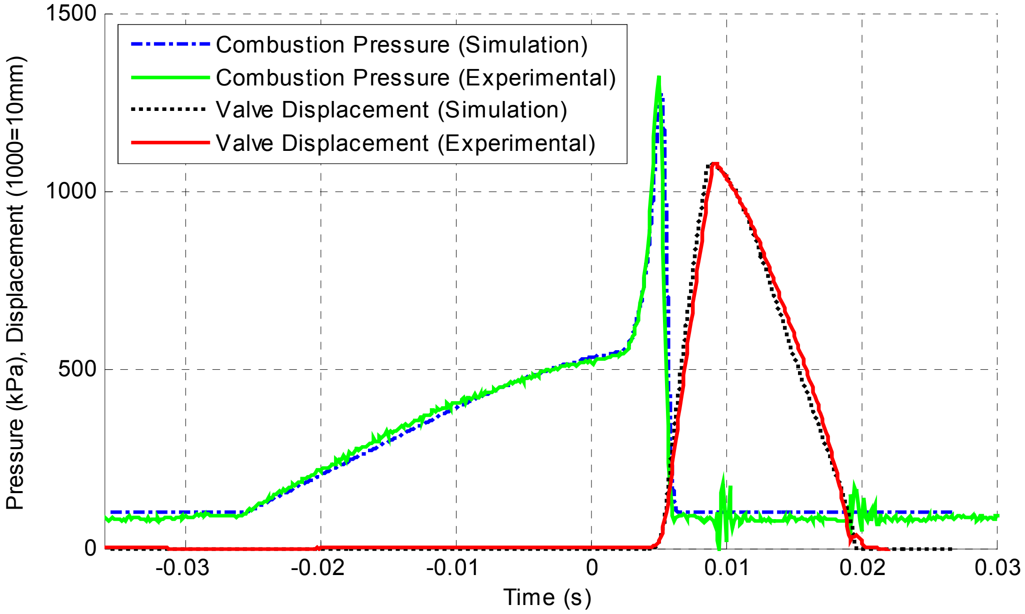

Figure 5-4: Combustion Pressure and Valve Displacement
for 653 kPa (80 psig) Supply Pressure.

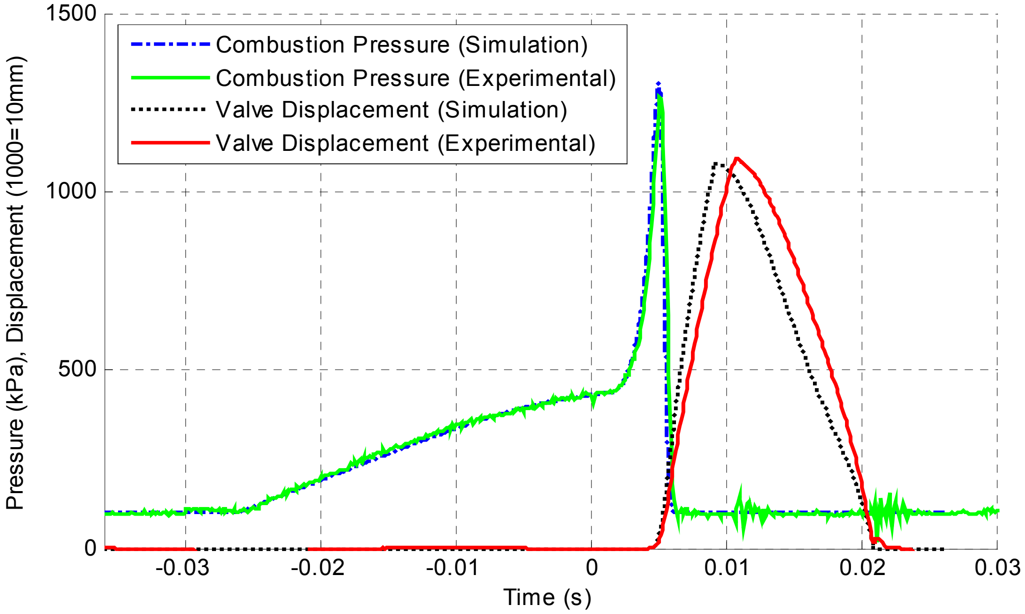

Figure 5-5: Combustion Pressure and Valve Displacement
for 515 kPa (60 psig) Supply Pressure.

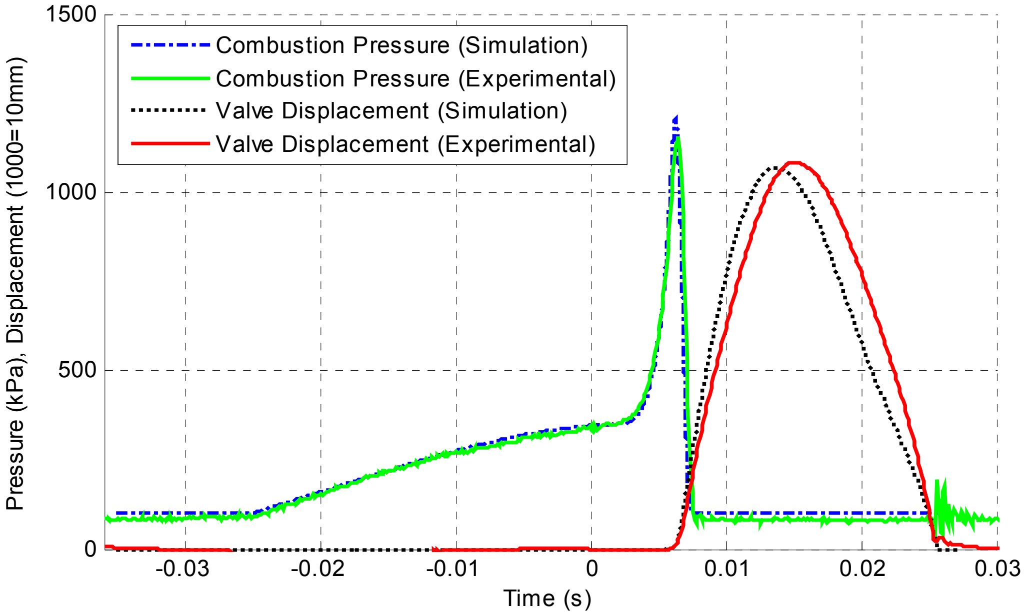

Figure 5-6: Combustion Pressure and Valve Displacement
for 419 kPa (46 psig) Supply Pressure.

Figures 5-4 through 5-6 show a very close match between simulated and experimental data, and demonstrate adequate fidelity in the combustion model (Equations 5.2 and 5.3) and combustion valve model (Equations 3.27 and 3.28). It should be noticed that in all cases the combustion pressure vents all the way down to atmospheric pressure well before the valve finishes its return stroke, which is a pre-requisite for over-expansion and breathe-in to be achieved in full FLPC operation. As previously mentioned, it was suspected that the relatively low combustion peaks are entirely due to limitations of the magnetic holding force (which was included in the model based on empirical observations). To verify this, we would like to examine the signals zoomed in around the instant where the valve begins its displacement. In addition to the combustion pressure signal, it is helpful to look at its first and second derivatives, which can give us valuable information based on their relative maxima and inflection points. Judging by the close resemblance between the modeled and experimental pressure plots, it should suffice to do this with the modeled data alone, which provides the convenience of numerically differentiating a noiseless signal. Figure 5-7 shows simulated valve displacement, combustion pressure, first derivative of combustion pressure, and second derivative of combustion pressure, respectively. The data shown stems from the simulated signals in figure 5-4 (80 psig supply pressure).

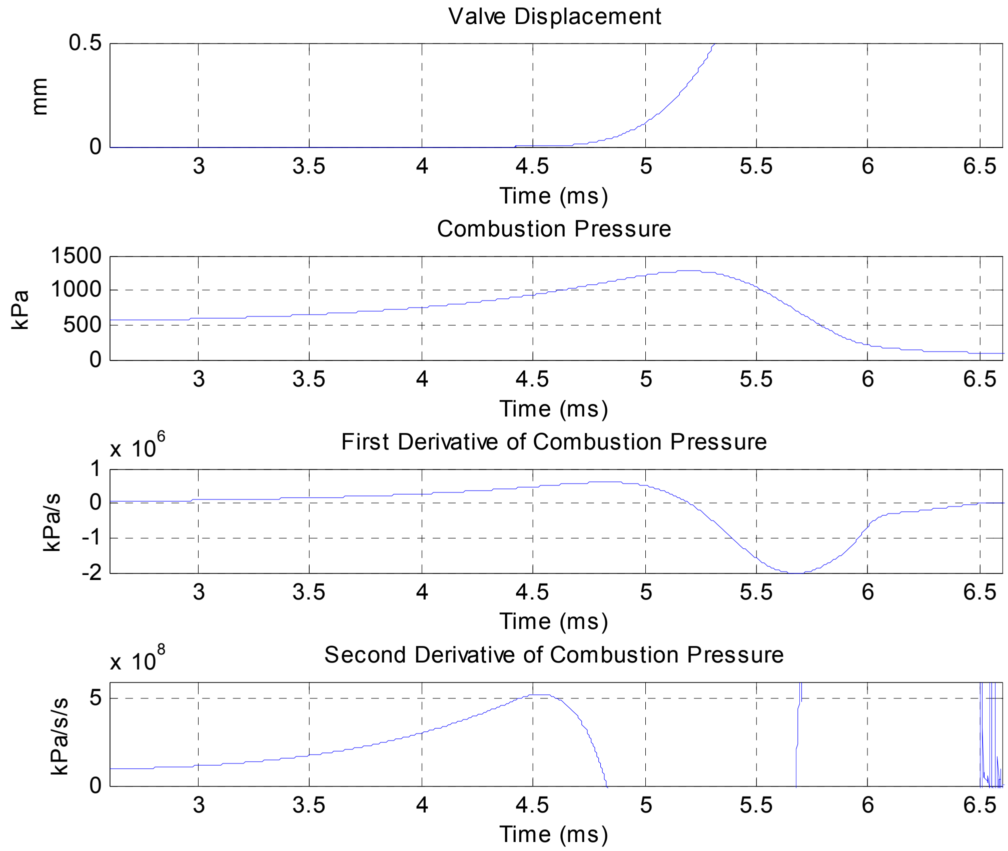

Figure 5-7: Magnetic Break-Away of Combustion Valve.

Figure 5-7 shows a precise time correlation between the beginning of the valve motion and a relative maximum in the second derivative of the combustion pressure at around 4.5 milliseconds. This indicates a drastic disruption in the second-order heat release dynamics described by Equation 5.2. Note that right before this disruption, the second derivative exhibits a positive slope, suggesting that if a stronger magnetic holding force could be achieved, stronger combustion peaks can be expected. As will be discussed later, this reveals one of the biggest drawbacks of this FLPC prototype: its need for a stronger permanent magnet.

High-Speed Video of Valve Motion

In addition to the valve displacement data taken with the laser interferometer, high-speed video of the valve in motion was obtained. A MotionScope$^{®}$ camera was used, taking video at 1000 frames per second (its fastest setting). Figure 5-8 shows a series of screen shots taken from the captured video, containing an complete valve cycle. The instant where the spark ignites is denoted as 0 milliseconds, and intervals of 2 milliseconds are shown. An LED was connected to the ignition command (i.e., the command sent to charge the ignition coil) and placed next to the valve so that the instant of spark could be known with respect to the valve motion. Therefore, this instant corresponds to the exact moment at which the LED becomes unlit.

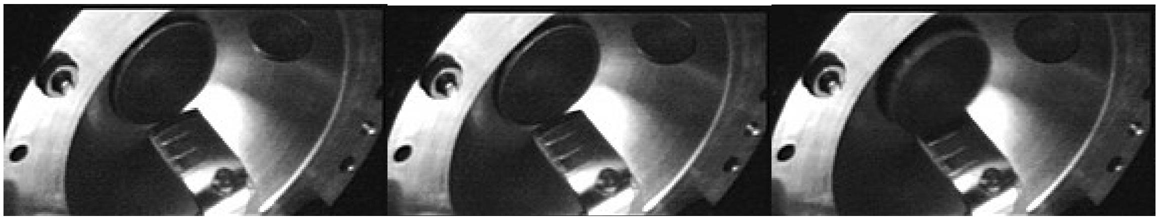

$t = 0\ \text{ms}\ (\text{spark})$ $t = 2\ \text{ms}$ $t = 4\ \text{ms}$

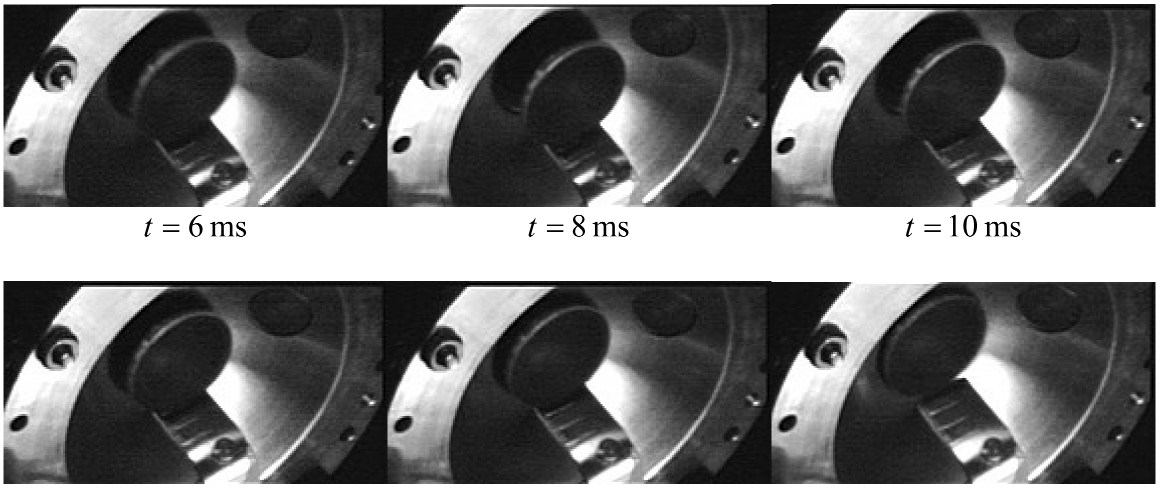

$t = 6$ ms $t = 8$ ms $t = 10$ ms

$t = 12$ ms $t = 14$ ms $t = 16$ ms

Figure 5-8: High-Speed Video of Combustion Valve.

Continuous Combustion

The open combustion configuration was also useful for tuning and testing continuous combustion cycles at various frequencies. Successful continuous combustion at up to 10 Hz was obtained. Figures 5-9, 5-10 and 5-11 show combustion cycles at 1, 5 and 10 Hz, respectively. Injection and exhaust durations were set to 30 milliseconds each. In order to preserve resolution, the time axes were shortened from 10 seconds (Figure 5-9) to 5 seconds (Figure 5-10) to 3 seconds (Figure 5-11). The variation in the combustion peaks can be explained by several factors, most notably slight variations in the air/fuel mixture (both quantity and quality), inconsistencies in the combustion process, variations in contact surface between the combustion valve and its valve seat, and the fact that the magnetic holding force is functioning at its limit.

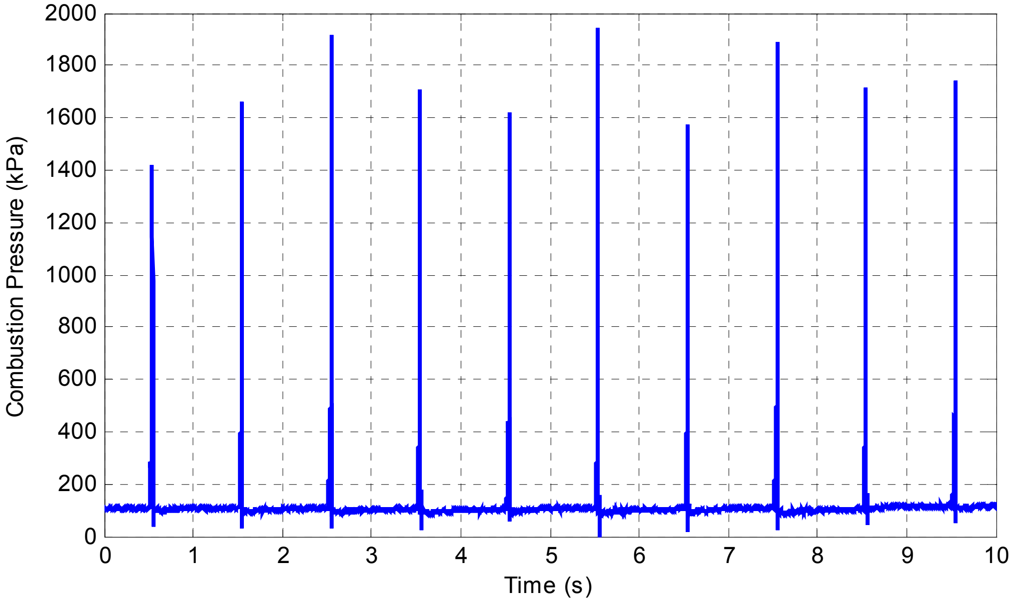

Figure 5-9: Continuous Open Combustion at 1 Hz.

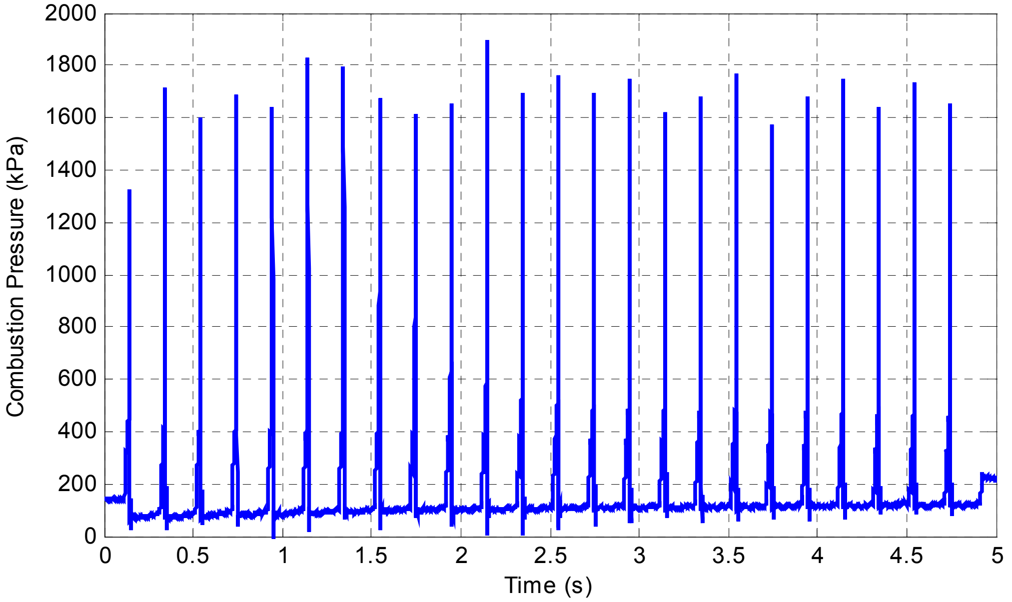

Figure 5-10: Continuous Open Combustion at 5 Hz.

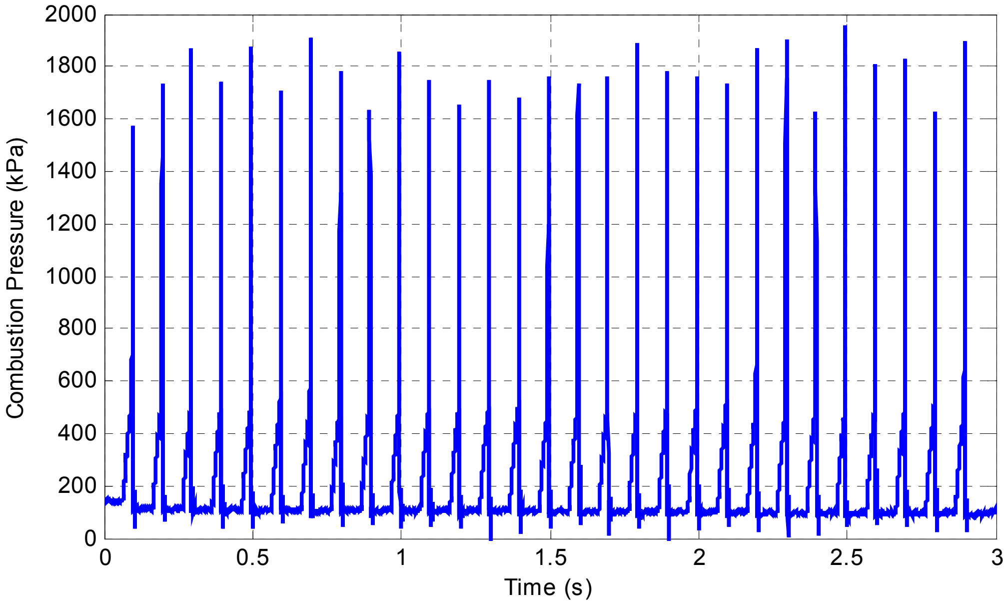

Figure 5-11: Continuous Open Combustion at 10 Hz.

5.2 Liquid-Piston

Another experiment was carried out to analyze the behavior of the liquid piston under no load on the pump side. The fluid chamber with a liquid-piston was connected to the expansion chamber, but this time the pump chamber was left disconnected. Thin, highly elastic commercially available silicone membranes were used for this experiment. High-speed video was taken to capture the response of the water slug to a combustion event. This is shown in Figure 5-12.

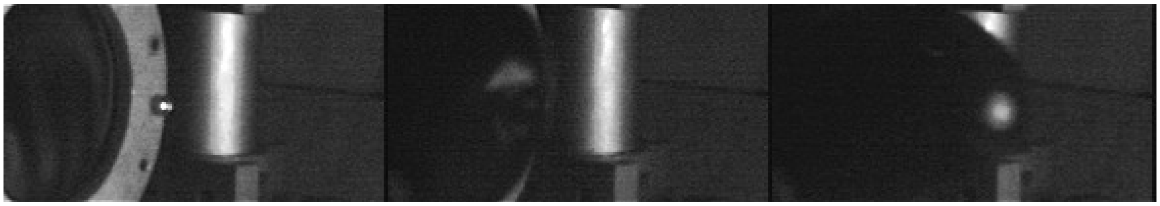
$t = 0$ ms $t = 5$ ms $t = 10$ ms

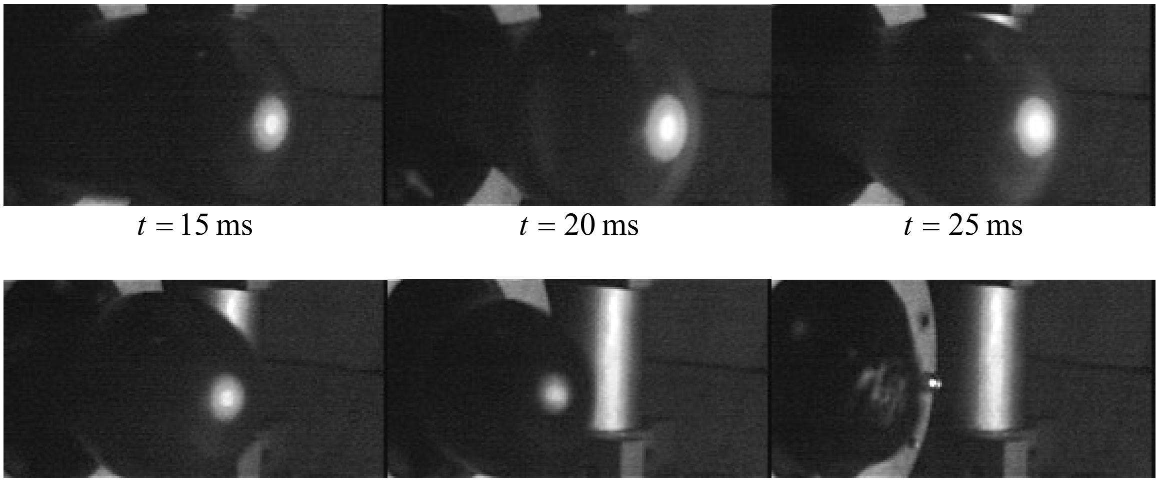

$t = 15$ ms $t = 20$ ms $t = 25$ ms

$t = 30$ ms $t = 35$ ms $t = 40$ ms

Figure 5-12: High-Speed Video of Liquid-Piston (with no load).

The extent of the inertial loading of the liquid-piston can be appreciated from looking at Figure 5-12. In addition, the diaphragms appeared unaffected, and it was proven that short-term thermal effects, as well as combustion-related phenomena, did not seem to affect the combustion-side diaphragm, since no signs of stress or irregularities in general were found. It is questionable, however, whether the liquid-piston would exhibit a similar behavior when exposed to a compressor load. Unfortunately, position sensing is not possible in the current FLPC design for full device operation, so we will have to rely on all pressure signals and the model itself to provide us with decipherable information.

5.3 Full Device Open Loop Operation

Experimental operation of the full FLPC device was first performed with external air supply – that is, without reinvesting pumped air from the reservoir for air/fuel injection. This is an important step because it allows us to test the "open loop" behavior of the system, and verify its performance against the model. The reservoir was first pre-

pressurized at 475 kPa (54 psig), and continuous running operation was attempted in order to test the pumping capability of the device. Since unexpected misfires can occur, the combustion exhaust on/off solenoid valve was kept in order to ensure that the uncombusted contents are exhausted and a new fresh mixture injected; otherwise, it is possible that the engine could stall, where the combustion chamber is unable to be reset in the event of a misfire. Again, the injection duration was set at 30 milliseconds, the "combustion exhaust" at 29 milliseconds, and the expansion solenoid exhaust also at 30 milliseconds. The command signal for this solenoid exhaust was fed through a "spike and hold" filter, so that the solenoid push force on the exhaust valve was strong enough to overcome any unexpected high-pressure in the expansion chamber, but could quickly come down to a steady-state force that requires less current to keep it open. Figure 5-13 shows an experimental dataset of open loop FLPC operation at 8 Hz. All four pressures (combustion, expansion, pump and reservoir) are shown. A close-up of a single cycle can show the combustion, expansion and pump pressures more in detail, but from this figure it can be seen that the reservoir pressure (turquoise) increases with every stroke, indicating pumping. Figure 5-14 shows a more zoomed-in view of the rising reservoir pressure, where an overall net increase of 90 kPa (13 psig) in 7 strokes (less than one second) can be seen. Based on Equation 2.17, this reveals a net energy transfer of 83 Joules (an average of 11.85 Joules per stroke), corresponding to an average pumped mass of 0.1 grams per stroke (only 51% of the total pumpable mass of an entire sweep volume, hereby defined as the pumping mass ratio). An in-depth analysis on this low pumping ratio will be provided later, after examining additional data.

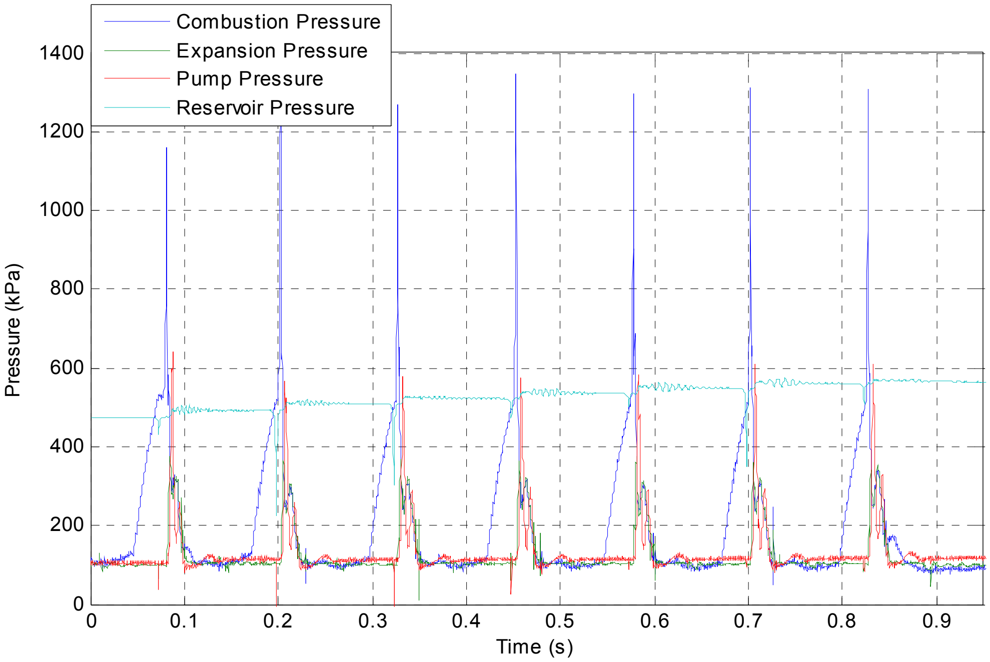

Figure 5-13: Continuous Open Loop FLPC Operation at 8 Hz.

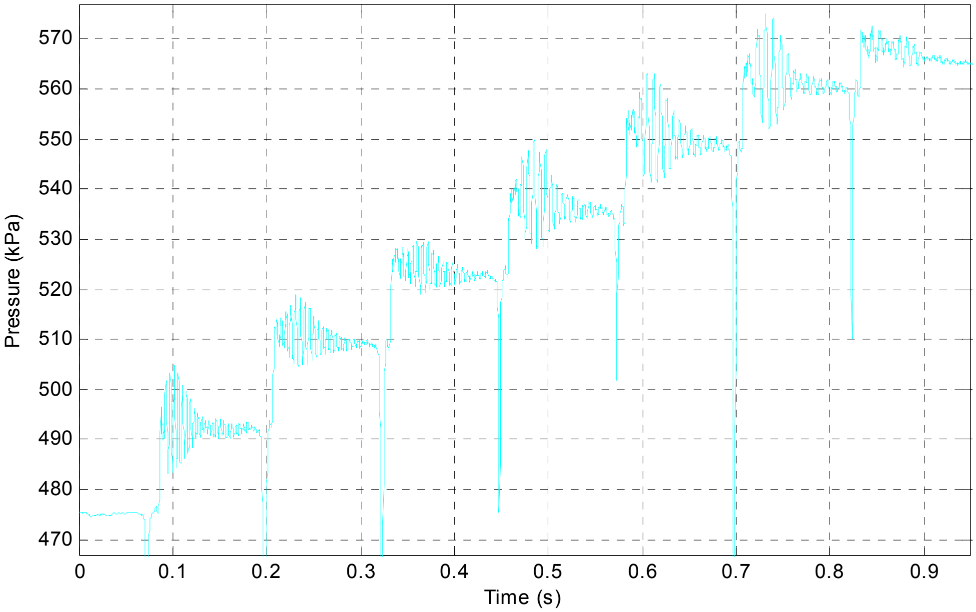

Figure 5-14: Zoomed-in View of Increasing Pressure in the Reservoir Due to Pumping.

Figure 5-15 shows a close-up of recorded experimental pressure signals for a full cycle of open loop FLPC operation. After a combustion peak of 1300 kPa (174 psig), it can be seen that the expansion pressure begins to rise and meets with the combustion pressure signal at about 400 kPa (43 psig), at which point the pump pressure has already begun to rise, indicating that the piston is somewhere in mid-stroke. Once the pump pressure exceeds the reservoir pressure of 535 kPa (62.9 psig), air is pumped and the reservoir pressure can be seen to rise to 550 kPa (65.08 psig), a net increase of 15 kPa (2.18 psig). The pump pressure peak can be correlated to the end of the stroke. It should be noticed that the combustion pressure does not reach atmospheric pressure; this is in part attributed to the fact that the piston does not complete a full stroke (revealed by the 51% pumping ratio), which is a direct consequence of the undesirable disruption in the heat release of combustion as the magnetic holding force is prematurely overcome, resulting in relatively weak combustions.

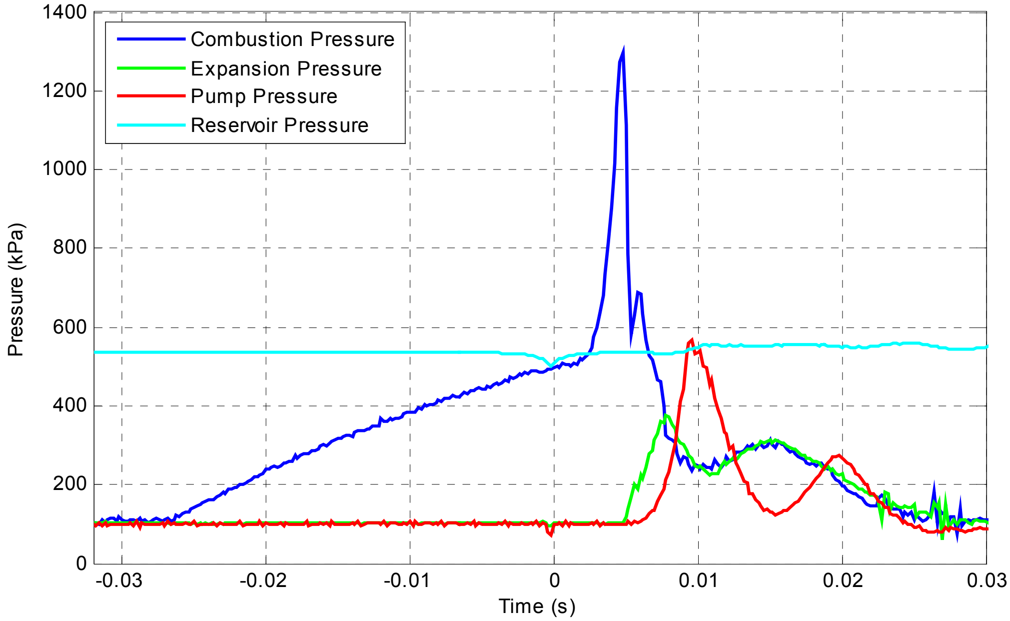

Figure 5-15: Close-up of Experimental Pressure Signals in Open Loop FLPC Operation.

Figure 5-16 shows the simulated equivalent to Figure 5-15, that is, a single-cycle from open loop FLPC operation, with the same experimental parameters. The close resemblance between both figures validates the dynamic model and its conjunction with Yong's combustion model, and reassures the usefulness of the model as a diagnostic tool. Since the model contains empirical information about the magnetic holding force and its effects on the combustion pressure dynamics, it confirms that the low yielded combustion pressure cannot complete a stroke with the current pumping load, thus being unable to achieve over-expansion. This will be discussed in more detail in Chapter 6.

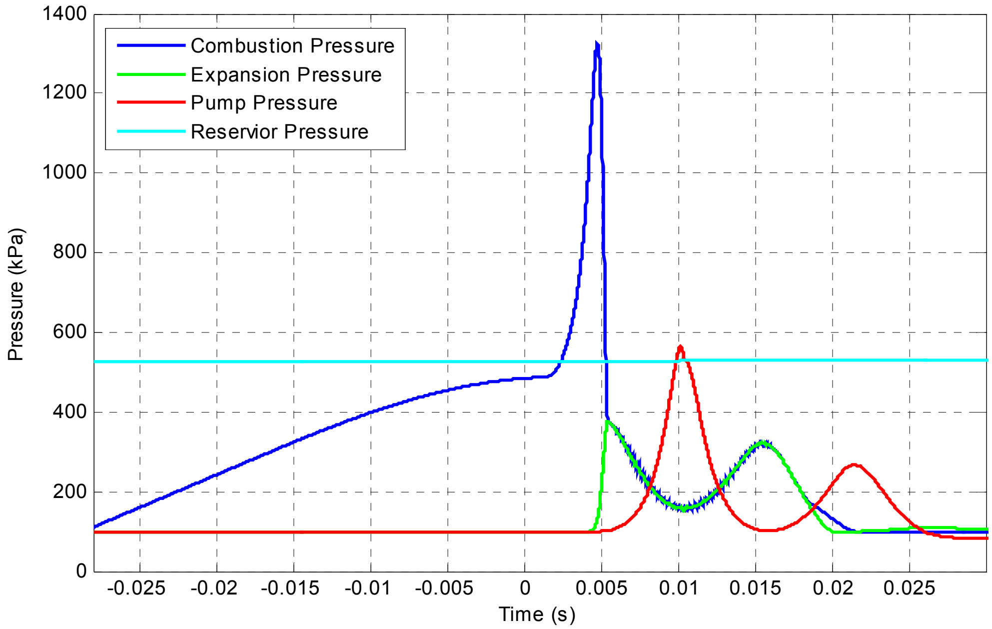

Figure 5-16: Close-up of Simulated Pressure Signals in Open Loop FLPC Operation.

To further demonstrate the model validation, the following figures show a side by side comparison of each modeled signal with its equivalent experimentally obtained counterpart: Figure 5-17 shows combustion pressure, Figure 5-18 shows expansion pressure and Figure 5-19 shows pump and reservoir pressures.

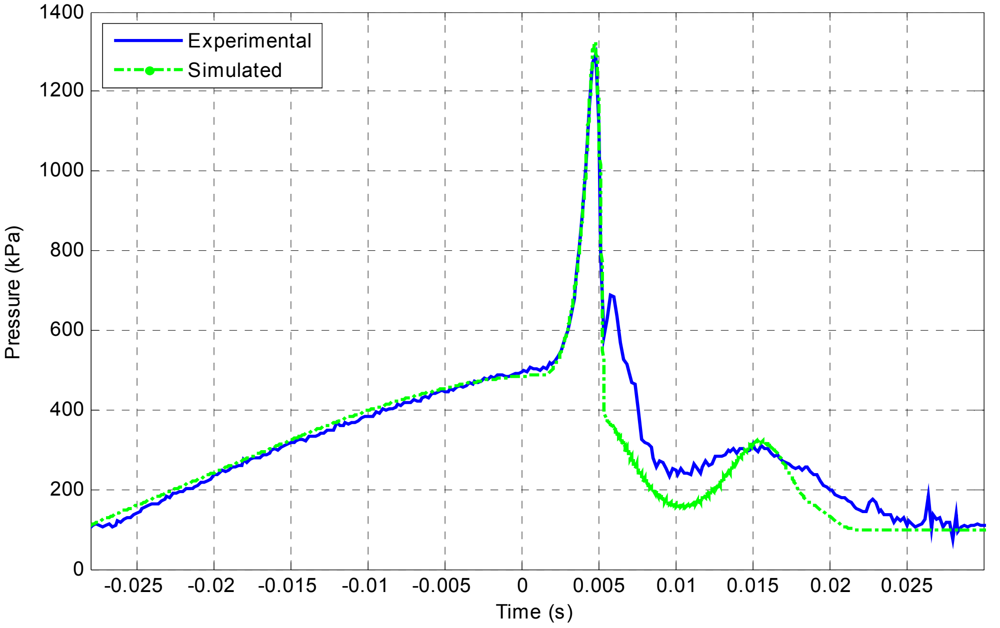

Figure 5-17: Experimental and Simulated Combustion Pressures.

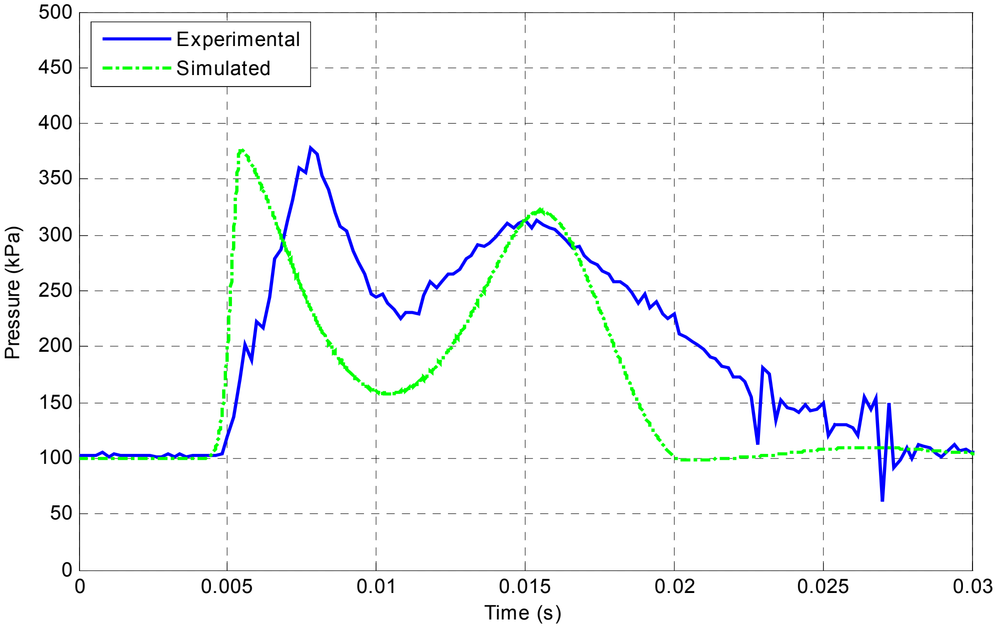

Figure 5-18: Experimental and Simulated Expansion Pressures.

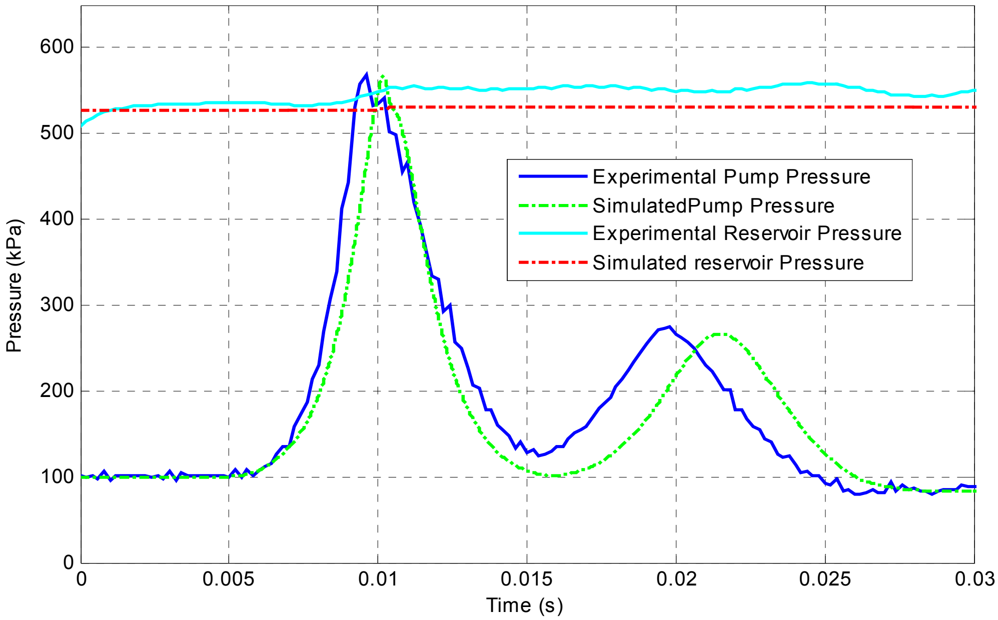

Figure 5-19: Experimental and Simulated Pump and Reservoir Pressures.

5.3 Full Device Closed Loop Operation

For closed loop operation of the FLPC, the reservoir was connected directly to the air injection line. In addition, a separate port in the reservoir was connected to external air supply through a ball valve, so that the reservoir could be pre-pressurized at any desired pressure. Also leaving this ball valve open would give us the option of running the engine with external air supply, which is useful for a variety of experiments. Typically, for a closed loop experiment, the ball valve would first be left open in order to fill the entire mixture line with pressurized stoichiometric mixture, and then shut off to yield true closed loop operation.

Achieving successful continuous closed loop operation – that is, delivering positive net pumps to the reservoir at every cycle – proved to be very difficult, perhaps due to the complications stemming from introducing a mechanical feedback loop into the system.

However, isolated events of successful net pumping were recorded, exhibiting nearly ideal operational characteristics. An example of such an event can be seen in Figure 5-20, which shows corresponding combustion, expansion, pump and reservoir pressures. This data looks very similar to the open loop data (Figure 5-15), except for the fact that the air for combustion is fed directly from the reservoir, which can be seen by the drop in reservoir pressure during the injection phase.

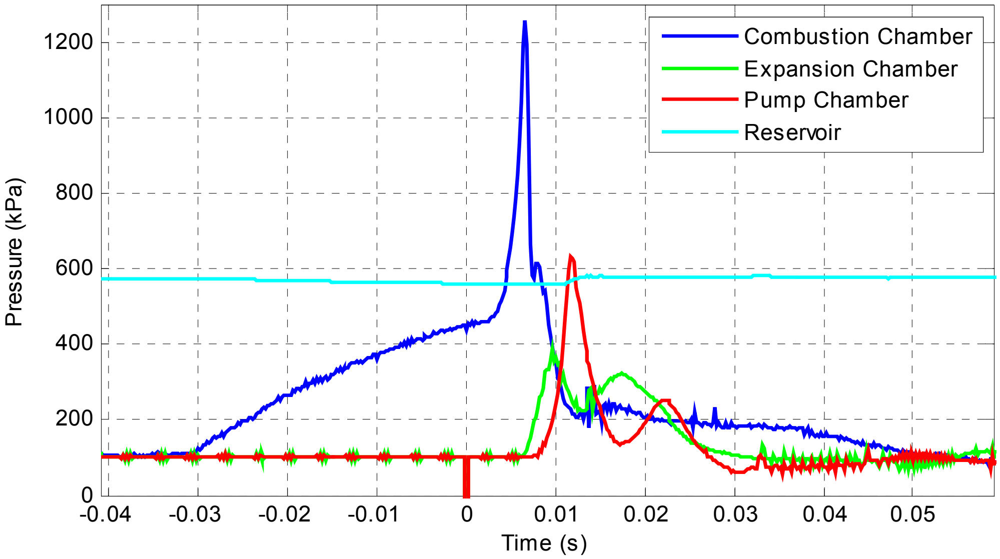

Figure 5-20: Experimental Pressure Signals for Closed Loop Operation

Similarly, Figure 5-21 shows a close-up of the reservoir pressure, which, as can be seen, exhibits a pressure drop corresponding to the injection phase (i.e., into the combustion chamber), followed by a rise corresponding to an enthalpy flow from the pump chamber.

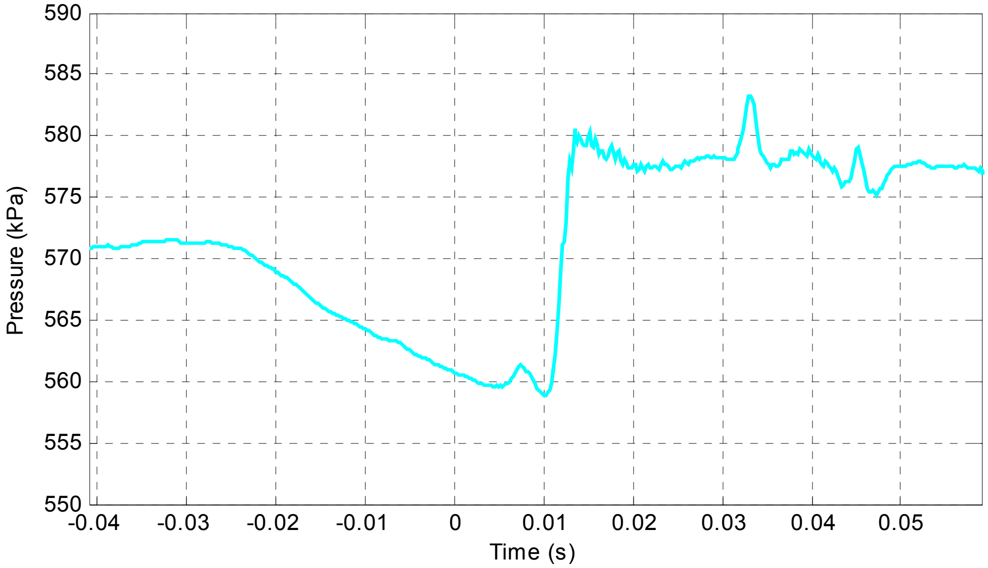

Figure 5-21: Close-up view of Experimental Reservoir Pressure

From the data shown in Figure 5-21, some approximations can be made regarding the energetic performance of the device. From the ideal gas law, assuming isothermal conditions in the reservoir (at ambient temperature), we can approximate the total amount of mass of air present in the reservoir at any given stage of this cycle based on its pressure: Prior to injection, the pressure of the 666-mL reservoir is about 570.99 kPa (corresponding to 4.397 grams of air); immediately after injection, its pressure is about 559.85 kPa (corresponding to 4.311 grams); and after the pump stroke (and some additional time to allow for settling, heat losses, etc), its pressure is about 576.51 kPa (corresponding to 4.439 grams). Knowing the mass of air in the reservoir at each stage, we can determine that the injection phase utilized 0.086 grams of air, and that the pump phase delivered 0.128 grams of air into the reservoir (66% pumping mass ratio).

If we assume that the injection mixture contains a stoichiometric ratio of air to fuel, we can approximate the overall amount of fuel that was used for this cycle:

$$m_{fuel} = \frac{m_{air\_inj}}{15.53} = \frac{0.086}{15.53} \approx 5.52 \times 10^{-3} \text{ grams} \tag{5.4}$$

Furthermore, we can determine the total initial amount of input energy based on the chemically stored energy of the fuel:

$$E_{in} = m_{fuel} e \tag{5.5}$$

where e, recall, is the specific energy density of propane, computed from its lower heating value:

$$e = 46{,}350{,}000 \frac{\text{J}}{\text{kg}} \tag{5.6}$$

and therefore, the total input energy is computed as,

$$E_{in} = \left(5.52 \times 10^{-6} \text{ kg}\right) \times \left(46{,}350{,}000 \frac{\text{J}}{\text{kg}}\right) \approx 255.9 \text{ Joules} \tag{5.7}$$

The net output energy is calculated as the net change in pneumatic potential energy in the reservoir; therefore, it suffices to look at the pre-injection and post-pump reservoir pressures. Applying Equation 2.11 for both these stages, we get:

$$\begin{aligned} E_f &= \frac{\left(576{,}505 \text{ Pa}\right)\left(666 \times 10^{-6} \text{ m}^3\right)}{1-\gamma_{air}} \left[\left(\frac{576{,}505 \text{ Pa}}{P_{atm}}\right)^{\frac{1-\gamma_{air}}{\gamma_{air}}} - 1\right] \approx 376.59 \text{ Joules} \\ E_i &= \frac{\left(570{,}990 \text{ Pa}\right)\left(666 \times 10^{-6} \text{ m}^3\right)}{1-\gamma_{air}} \left[\left(\frac{570{,}990 \text{ Pa}}{P_{atm}}\right)^{\frac{1-\gamma_{air}}{\gamma_{air}}} - 1\right] \approx 371.39 \text{ Joules} \end{aligned} \tag{5.8}$$

Hence, the total output energy is computed as,

$$E_{out} = E_f - E_i \approx 5.2 \text{ Joules} \tag{5.9}$$

Finally, the overall system efficiency obtained in this cycle can be approximated as the ratio of output to input energies:

$$\boxed{\eta_{cycle} = \frac{E_{out}}{E_{in}} \approx \frac{5.2}{255.9} \approx 2.03\,\%} \tag{5.10}$$

Even though a true measure of power capability cannot be obtained from an isolated event (in standard terms of pressure and volumetric flow rate), its potential can be approximated based on the net output energy (Equation 5.9) and the previously demonstrated 10-Hz capability. Therefore, the potential pneumatic power capability for this event is,

$$\boxed{\wp_{net} \approx 52\ \text{Watts}} \tag{5.11}$$

Table 5.1 shows a list of all relevant experimental parameters and results from this particular event.

Table 5-1: Experimental Parameters and Results From
Closed Loop Operation of Single Event.

Parameter	***Description***	***Approximate Value***
V_{res}	*Reservoir Volume*	**666 mL**
m_{c0}	*Total "pumpable" mass (contained in sweep volume)*	**0.196 g**
Δt_{inj}	*Ibjection Valve Opening Duration*	**35 ms**
Δt_{exh}	*Solenoid Exhaust Opening Duration*	**29 ms**
P_{s1}	*Reservoir Pressure Before Injection*	**571 kPa**
P_{s1}	*Reservoir Pressure After Injection*	**559.9 kPa**
P_{s1}	*Settled Reservoir Pressure After Pump*	**576.5 kPa**
m_{s1}	*Mass of Air in Reservoir Before Injection*	**4.397 g**
m_{s2}	*Mass of Air in Reservoir After injection*	**4.311 g**
m_{s3}	*Mass of air in Reservoir after Pump*	**4.439 g**
m_{air_inj}	*Mass of Air used During Injection*	**0.086 g**
m_{fuel}	*Mass of Propane used During Injection*	**0.00055 g**
E_{out}	*Net Energy Delivered to Reservoir*	**5.2 Joules**
f_0	*Operating Frequency*	**10 Hz**
$\wp_{net}$	*Net Power Delivered to Reservoir*	**52 W**
η	*Overall Efficiency*	**2.03 %**

CHAPTER VI

DEVICE LIMITATIONS, MODEL-BASED DIAGNOSTICS, AND SUGGESTIONS FOR FUTURE DESIGNS

6.0 General Discussion

Chapter V presented experimental results obtained both in open loop and closed loop configurations. While continuous closed loop operation was not attained with the FLPC's current configuration, experimental open loop operation showed good pumping capability at target reservoir pressures, and more importantly, it demonstrated the high fidelity of the model and its usefulness as a diagnostic tool for future improvements of this device as well as future new designs.

Failure to achieve continuous closed loop operation can be attributed to several reasons. It must be acknowledged that some of these may be unmodeled phenomena, in particular dealing with the piston dynamics. For instance, recall from Equation 3.27 that the liquid piston was modeled as a linear mass-spring-damper system. While this may be an adequate geometric linearization assuming a uniform spherical-segment shape in the diaphragms, in reality these have their own internal resonant dynamics which may affect the overall behavior of the system.

However, some other important reasons pertaining to the lack of closed loop success can and should be explored within the context of the model. In addition, the experimental data itself contains patterns and trends that should not be overlooked This chapter will examine some of these reasons, both from the model and the experimental data.

6.1 Exhaust Gas Flushing

The closed loop experimental data exhibits a very strong correlation between isolated events achieving successful pumping and preceding combustion misfires. In other words, directly after a misfire, an event achieving positive net pumping is very likely to occur. Take, for example, the dataset shown in Figure 6-1. It shows combustion and reservoir pressures for a typical closed loop dataset, where six clear net pumps can be seen (all marked with a red circle), five of which occur directly after misfires. Other datasets exhibit this correlation as well.

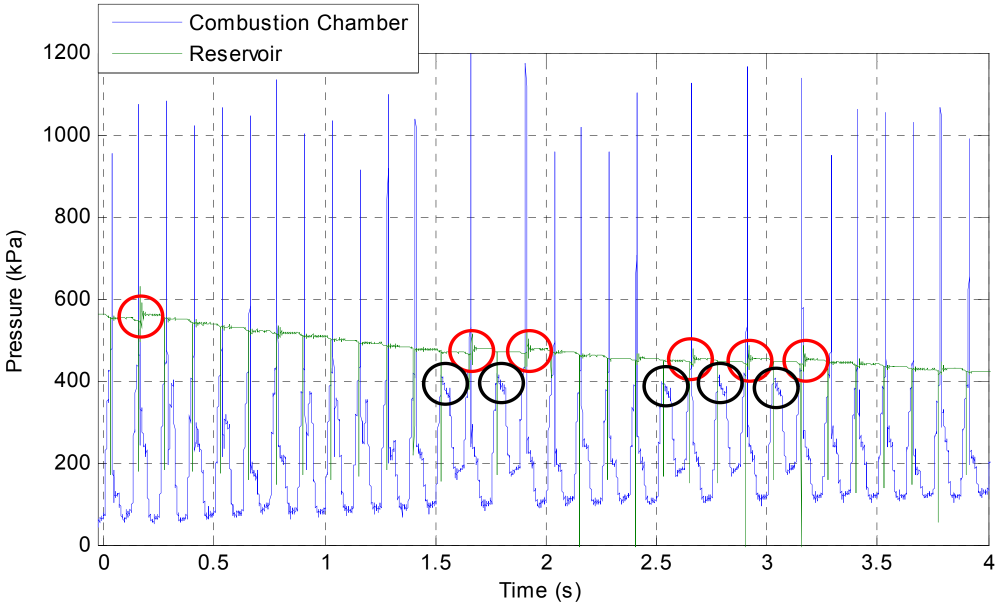

Figure 6-1: Closed Loop Experimental Dataset.

Red circles indicate net pumps; black circles indicate misfires.

Another detail worth noticing from Figure 6-1 is that the five strongest combustion peaks also occur directly after the five misfires in the set. This is very likely caused by the fact that a misfire tends to flush out the contents of the combustion chamber, particularly products from previous combustion. Since the device is not exhibiting over-expansion and its associated breathe-in benefits (an issue that will be discussed later in this chapter), it is assumed that after a regular combustion cycle a certain amount of previous combustion products remain in the combustion chamber and mix with the next incoming air/fuel mixture, thus decreasing the amount of combustible contents and perhaps even affecting the quality of the mixture. Needless to say, this would translate into sub-par combustion characteristics.

In some cases, however, the combustion peaks after the misfires are not necessarily the strongest in the set, and the qualitative difference between a typical fire (no pump) versus one that occurs after a misfire (pump) becomes more difficult to see. Figure 6-2 shows two events from another dataset where this is the case. Pressure signals from both events are shown, the solid corresponding to a post-misfire event (which pumped), and the dashed corresponding to a regular event (which did not pump). From the combustion and expansion pressure signals (blue and red signals, respectively) it is very difficult to notice any distinction which could indicate a difference in input power. However, the pump signals (green) do display an important qualitative difference. Figure 6-3 show a close up of the pump signals, and it can be seen that the solid line exhibits a steeper slope in its rise than its dashed counterpart. This reveals a higher acceleration of the piston which indicates higher input power in the post-misfire event.

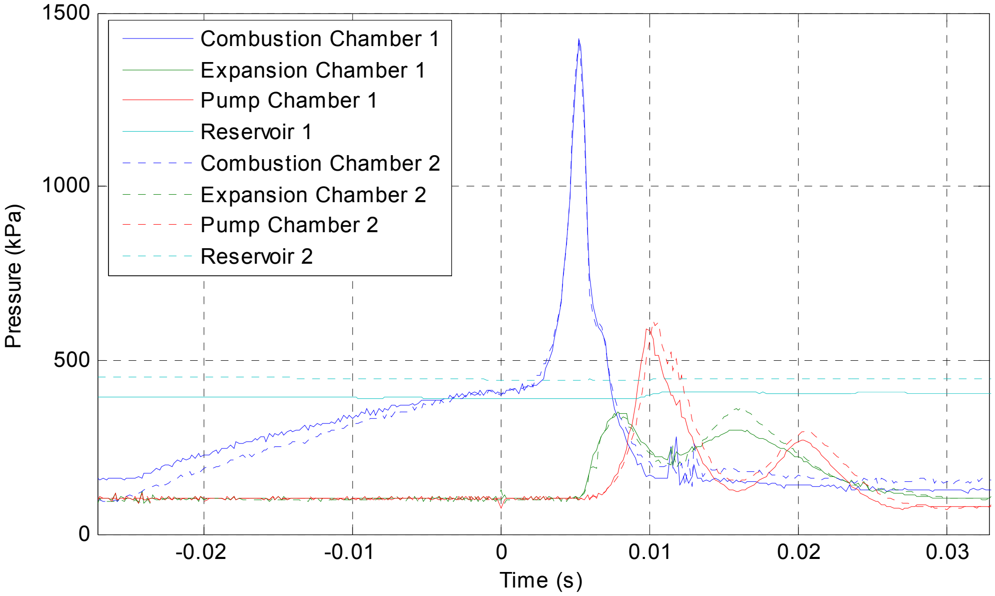

Figure 6-2: Side-by-side Comparison Between Post-Misfire Event and Regular Event.

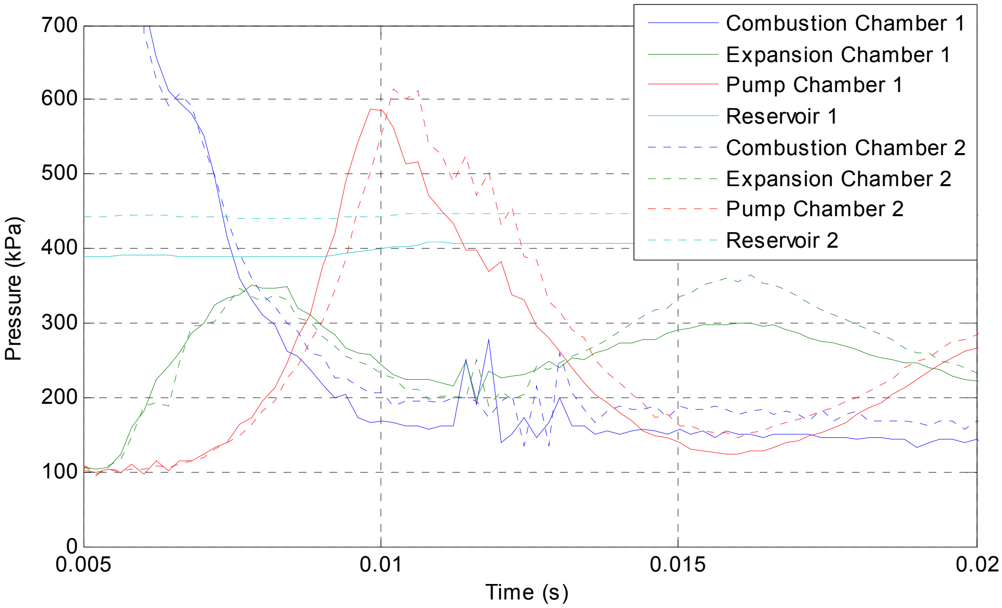

Figure 6-3: Close-up View of Side-by-side Pump Signals.

6.2 Geometric Constraints

From the misfire analysis it can be concluded that complete exhaust in the combustion chamber is necessary in order to achieve good combustion. In the case with this constant-volume combustion chamber, complete exhaust (i.e., via on/off exhaust valve) would still leave a certain amount of combustion products in the chamber (whatever mass can fit in the volume at atmospheric pressure). Recall that the original design accounted for a certain amount of breathe-in after over-expansion, which would both cool down the combustion chamber and flush its contents with fresh air. In order to satisfy over-expansion and breathe-in, Equation 2.9 has to be met, which specifies a precise volumetric ratio between total piston sweep volume and combustion chamber volume required to efficiently match the combustion energy to the load of the compressor. Experimentally, however, these volumetric constraints have proven difficult to maintain, at least in the current FLPC prototype.

Initial Expansion Chamber Volume

Recall that the sweep volume of the liquid-piston is the sum of the "relaxed" volumes of the expansion and pump chambers. Therefore, in order for the piston to complete a full sweep, it needs to start completely receded against the expansion chamber walls, which is an unstable position. The original design intended for this to be achieved dynamically – that is, to ignite the charge in the combustion chamber at the precise instant that the piston completes the dynamic overshoot of its passive return stroke. In addition to this being a requirement for over-expansion, it is also a requirement for meeting the work balance described by Equation 2.4. Therefore, since the system starts at equilibrium, the first cycle of every run is not expected to produce much (if any) net energy output, but rather drive the system towards its limit cycle. Figures 6-4 and 6-5 show pressure signals and piston displacement, respectively, for a simulated 2-cycle run that demonstrates this concept.

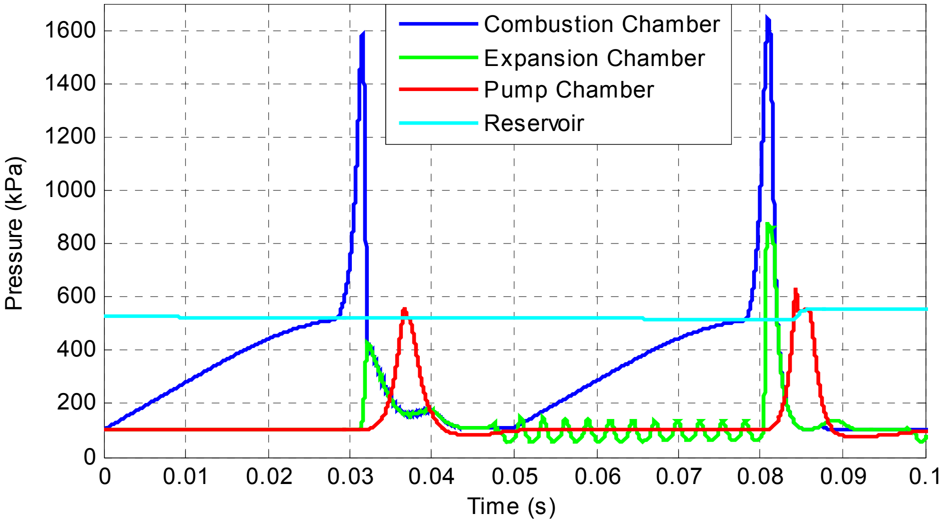

Figure 6-4: Simulated 2-Cycle Run of FLPC.

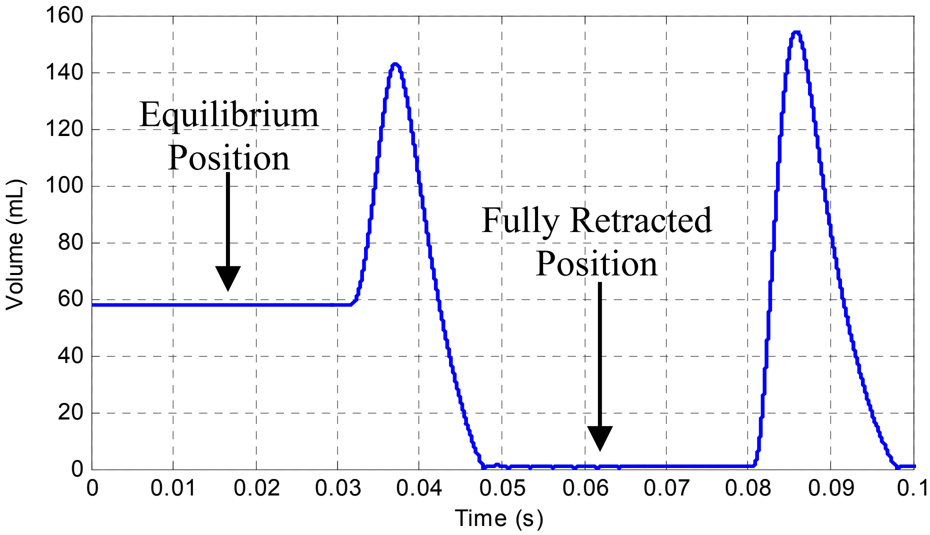

Figure 6-5: Simulated Piston Displacement.

As can be seen from Figure 6-5, the initial position of the piston is at its equilibrium point, roughly 60 mL away from desirable. This has two effects on its stroke: first, the potential sweep volume is much lower, so there is less "pumpable" air in the pump chamber; and secondly, the expansion chamber will have to spend energy to bring its volume up to a pressure capable of performing appreciable PV work on the piston. All in all, this stroke hardly takes advantage of the inertial loading of the free piston, and consequently, as seen in Figure 6-4, it results in a no-pump event for the first cycle. After the end of the first stroke, however, it can be seen from Figure 6-5 that the piston is capable of returning all the way to its desirable initial position, and so the second cycle exhibits a more ideal profile. Referring back to Figure 6-4, it can be seen that the expansion pressure signal jumps significantly higher upon the combustion valve opening. (This should make sense considering there is very little volume to for the combustion gases to fill in the expansion chamber, compared to the case in the first cycle). Subsequently, a more pronounced rise in the pump signal can be seen, indicating better power transfer through the inertial loading, and finally, a very strong pump can be seen by the rise in the reservoir signal.

Due to the fast dynamics of the system, it's experimentally difficult to time the injection and ignition commands to fire precisely at the desired moment. This is especially true in the case with open loop control (note: from control theory, NOT 'open loop' in the context of air routing), because the relative timeframes between important events (spark, pressure peaks) vary from cycle to cycle. Therefore, a robust closed-loop control platform would be necessary to continuously and reliably achieve this. In addition, the simulation reveals that the piston return stroke is much faster than dictated solely by its passive dynamics. This is not surprising considering that the unpumped air after each power stroke acts like a stiff spring and greatly increases the true natural frequency of the system. As a consequence, it seems implausible that by the end of the return stroke there could be a fresh new air/fuel mixture in the combustion chamber waiting to be ignited, as there is simply not enough time.

The inclusion of this relaxed expansion volume is perhaps the most limiting design choice made. Its original purpose was to allow for an overshoot of the underdamped passive dynamics of the piston (and its associated energy savings) and to increase the sweep volume length-wise so that the overall diameter could be kept smaller. In hindsight, it is learned through experimental characterization (and with the help of the model) that the small energy savings that could be achieved by allowing the overshoot of the piston are greatly outweighed by the complications of proper signal timing in such a dynamically complex system (slight imperfections of which can cause energy losses far more impacting than the presumed gains). It is therefore strongly suggested for a future design revision to flatten the expansion chamber walls such that its relaxed volume coincides with the piston equilibrium point, and in turn regain the desired sweep volume by either increasing the radius of the pump hemisphere or its depth (bullet-like shape).

Combustion Chamber Volume and Leakage

Having an accurate combustion chamber volume is also tricky. Since this volume is much smaller than the sweep volume, small deviations are likely to compromise the required volumetric ratio of Equation 2.9. These deviations, however, are almost inevitable when dealing with ports and fittings, which introduce irregular dead volumes.

In addition, leakage at high pressures was observed, both through the combustion valve and through the valve guide towards the back side. The leakage observed through the combustion valve is not too large, and can be reduced by having a stronger permanent magnet. However, the leakage through the valve guide was found to be more significant, and more difficult to address. Figure 6-6 shows a pressure signal in the combustion chamber for a square wave, where pressurized air entered the chamber via on/off solenoid injection valve, and exited similarly through a similar exhaust valve. Below the pressure signal, the valve command signals are shown. Leakage out of the combustion chamber can be observed by the drop in pressure directly after the injection valve closes (at 1 and 3 seconds). More importantly, however, it can be seen that upon closing of the exhaust valve (2.25 and 4.25 seconds), the pressure rises, indicating reverse leakage through the valve guide.

(a) Pressure in Combustion Chamber

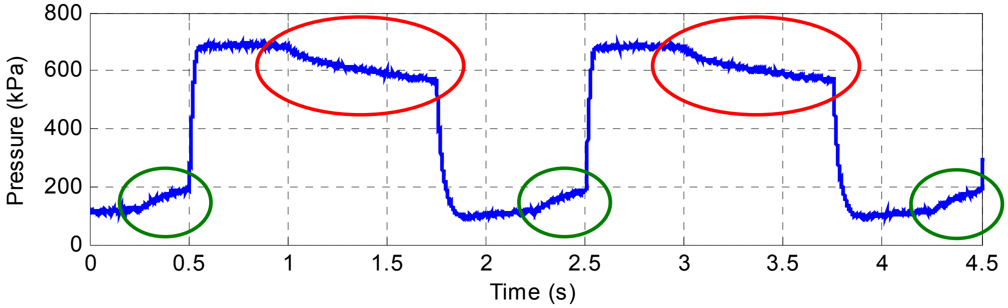

(b) Injection and Exhaust Valve Command Signals

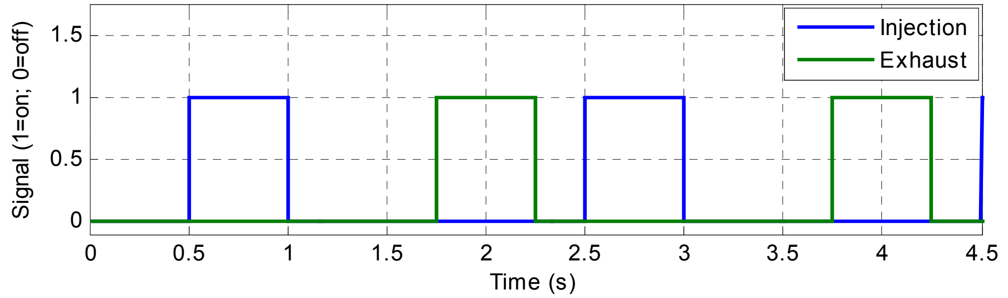

Figure 6-6: Experimental Leakage Test.

Red circles indicate leakage from chamber; green circles indicate reverse leakage.

Leakage in the combustion chamber is undesirable for the obvious reason that more air and fuel would need to be used in order to achieve a certain injection pressure (or alternatively, if injection is based on a set valve-opening duration, the actual injection pressure would be lower than desired). However it is less obvious (and probably more important) that leakage through the valve guide essentially increases the effective volume of the combustion chamber, since the back side (i.e., end cap) has non-negligible dead space. Some of this space has been filled with incompressible silicone, but some others, especially the sweep volume of the ferrous plate, cannot be removed. The full effects of this back-leakage are difficult to quantify (though they are not expected to be too significant), but future designs should remove any unnecessary dead space in the back side, and if possible tighten the valve guide tolerance.

6.3 Magnetic Holding Force

It was mentioned in Chapter V that one of the biggest drawbacks of this FLPC prototype was its need for a stronger permanent magnet. This statement was made in the context of observing that the magnetic holding force was being overcome prematurely – that is, before the combustion reactants could fully release all of their heat. This hypothesis can be examined more in detail with the help of the model, by evaluating the system behavior for slightly different magnetic holding forces. Three cases are considered: The first has a holding capacity of about 520 kPa (roughly highest desirable injection pressure); the second one has a more desirable holding capacity of about 1400 kPa, and the third one can hold up to 1600 kPa. Two graphs are shown for each dataset, the first one showing all pressure signals and the second one shows the pneumatic potential energy in the reservoir (which quantitatively shows pumping performance). Finally, each dataset is shown with two simulated cycles. Figures 6-7 and 6-8 show the first set. It can be seen that the pressure peaks in Figure 6-7 are similar to those obtained experimentally in our device. Figure 6-8 shows an net energy increase in the reservoir, though relatively small.

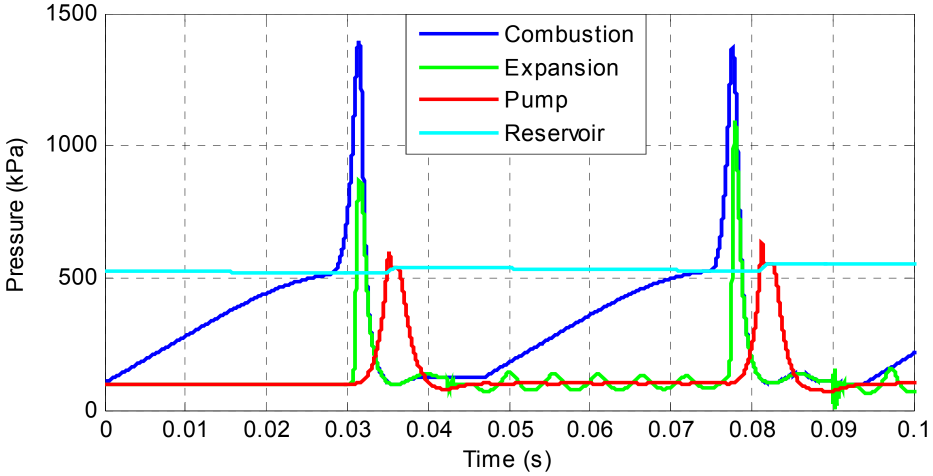

Figure 6-7: Simulated Pressure Dataset With 520-kPa Holding Capacity.

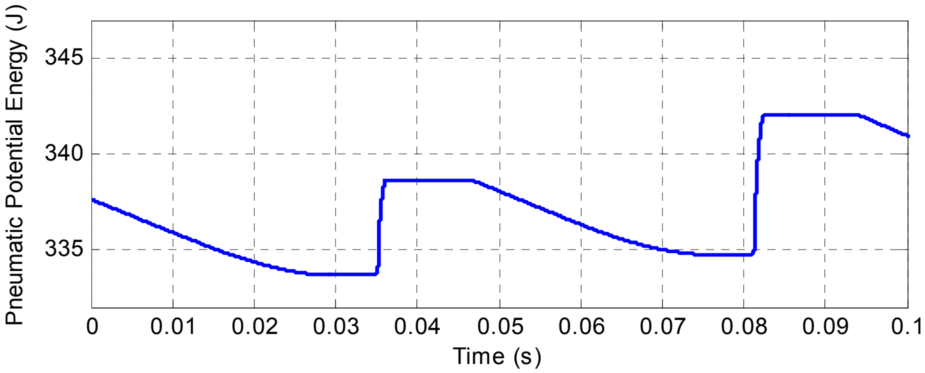

Figure 6-8: Simulated Pneumatic Potential Energy in Reservoir.

This next data set shows a more desirable performance obtained with 1400-kPa holding capacity. The combustion peaks in Figure 6-9 are significantly higher, but it is otherwise difficult to see much qualitative difference from Figure 6-7. The energy plot in Figure 6-10, however, demonstrates a significantly better energetic performance is achieved with this higher magnetic holding force.

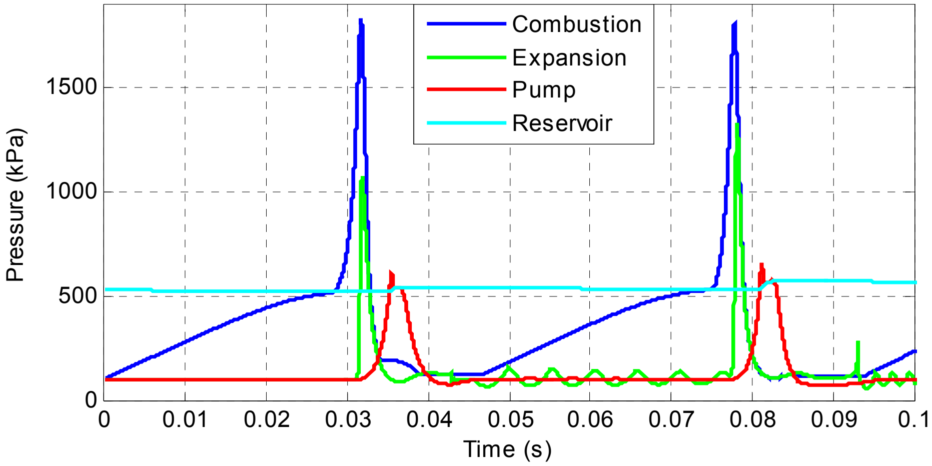

Figure 6-9: Simulated Pressure Dataset With 1400-kPa Holding Capacity.

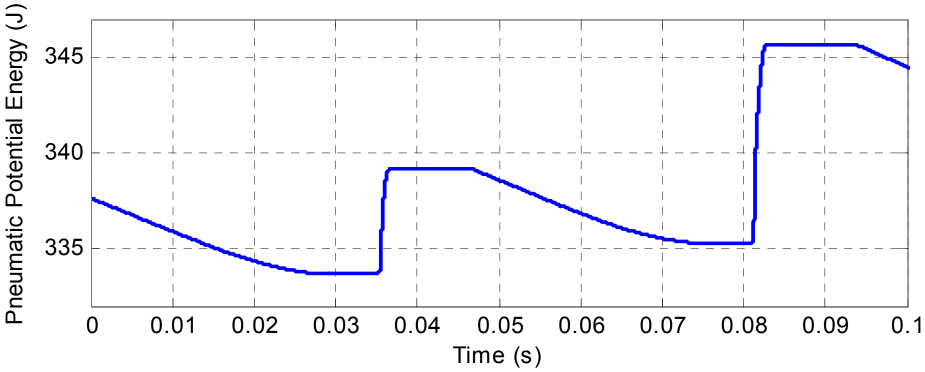

Figure 6-10: Simulated Pneumatic Potential Energy in Reservoir.

Finally, an even higher holding capacity of 1600 kPa is shown in Figures 6-11 and 6-12, where it can be seen that the performance is much worse than in either previous case. It can be seen from Figure 6-11 that the combustion pressure stays significantly above atmospheric by the end of each cycle. This is due to the fact that too strong of a magnetic holding force will not allow for the combustion valve to fully break away, but will rather keep its displacement and opening duration very small. Similarly, Figure 6-12 shows the consequential poor pumping performance.

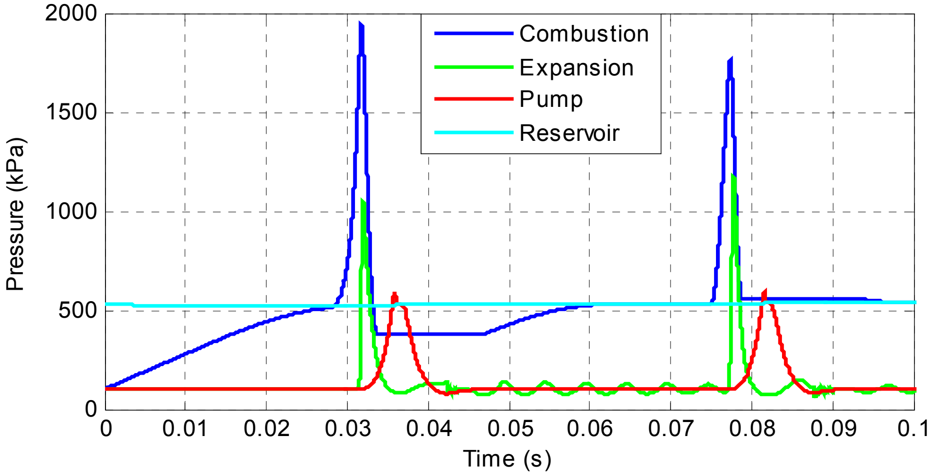

Figure 6-11: Simulated Pressure Dataset With 1600-kPa Holding Capacity.

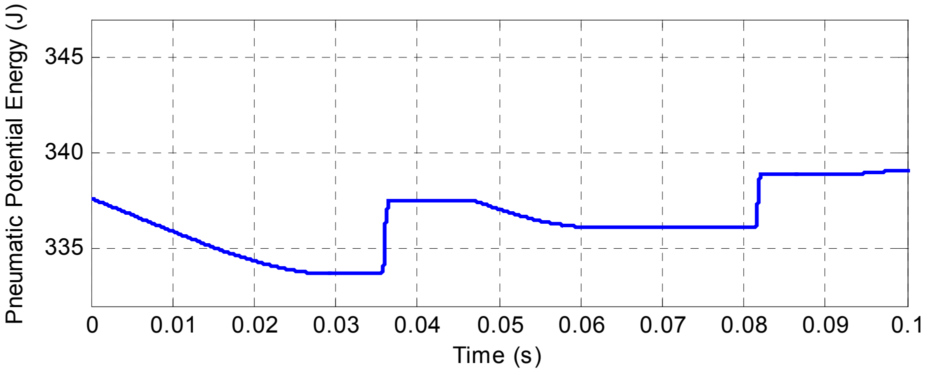

Figure 6-12: Simulated Pneumatic Potential Energy in Reservoir.

Proper magnetic holding force is, therefore, a tunable parameter. The experimentally observed holding force resembles most the one shown in Figure 6-7, which is clearly below par. Therefore, it is recommended for future designs that a much stronger permanent magnet be used, which would involve obtaining a custom magnet and re-designing its end cap housing.

6.4 Membrane Deformation

As previously mentioned, the liquid-piston is believed to have unmodeled internal dynamics that could hinder the overall device performance if not addressed properly. Chapter V showed a high-speed video of the "free response" of a water slug trapped between thin elastic diaphragms (Figure 5-12), which had a reasonably regular displacement profile. However, with the liquid-piston under load, its effective natural frequency is expected to be significantly higher (which is verifiable both experimentally and with the model). In order to assess whether a loaded device would exhibit a different displacement profile, another free response high-speed video was taken for an elastic piston with a much higher natural frequency. The piston consists of a thick silicone membrane, with no water. The idea is to analyze any qualitative differences between these two, within the context of the true loaded liquid-piston. Figure 6-13 shows screenshots of the displacement profile of this silicone slug, in response to a combustion input. It can be seen that the diaphragm first deforms annularly, with its center lagging behind. This displacement profile resembles that of the (0,2) vibrational mode of a circular membrane [24], shown in Figure 6-14.

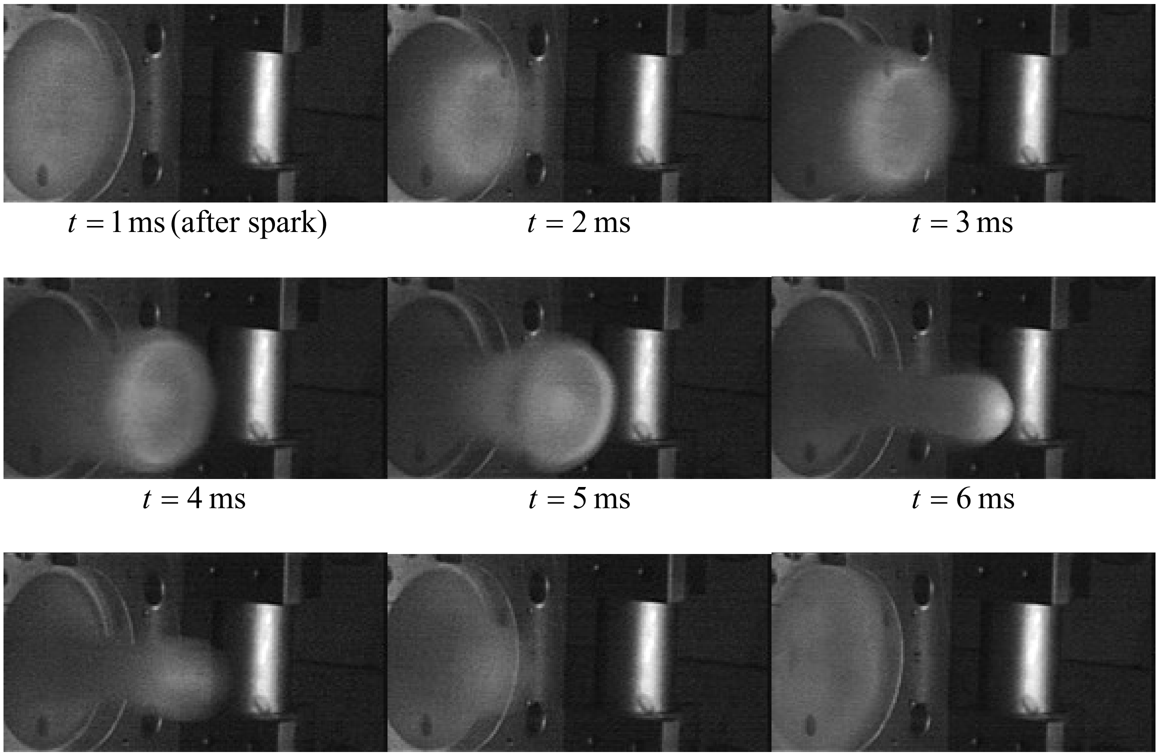

$t = 1\,\text{ms}$ (after spark) $t = 2\,\text{ms}$ $t = 3\,\text{ms}$

$t = 4\,\text{ms}$ $t = 5\,\text{ms}$ $t = 6\,\text{ms}$

$t = 7\,\text{ms}$ $t = 8\,\text{ms}$ $t = 9\,\text{ms}$

Figure 6-13: High-Speed Video of Silicone-Rubber Piston (with no load).

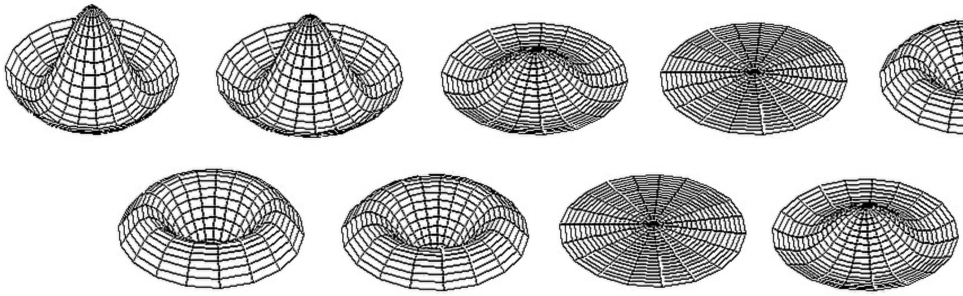

Figure 6-14: (0,2) Vibrational Mode of a Circular Membrane.

It is unclear precisely what the displacement profile of a loaded liquid-piston really looks like, or how much of an effect an irregular displacement profile would have on the device performance. However, some experimental data suggests that this should be investigated further. Figure 6-15 shows pressure signals of one cycle of an experimental dataset, where both the expansion and pump pressure signals saturate at around 300 kPa. The mere fact that the reservoir pressure signal shows that pumping occurred reveals that this saturation cannot be real, and strongly suggests that there is blockage of the pressure ports, which could happen if the liquid-piston had an irregular displacement profile.

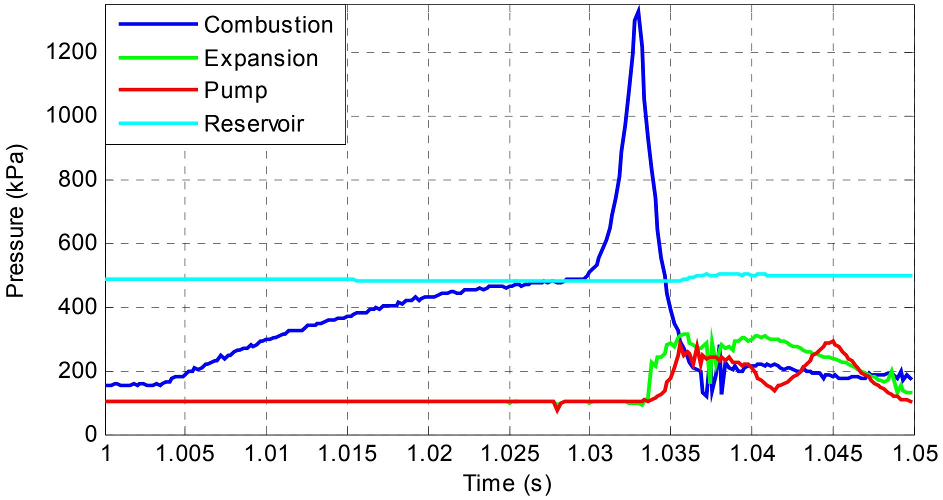

Figure 6-15: Experimental Saturation of Expansion and Pump Pressure Signals.

The main reason as to why the liquid-piston might exhibit an irregular vibrational mode is likely linked to flow direction of the combustion gases entering the expansion chamber. As the combustion valve opens, it reveals an annular flow orifice, which may induce localized flow forces on the membrane and trigger undesired vibrational modes on the liquid-piston. Since our model assumes homogeneous pressure dynamics in the control volumes, these localized flow forces cannot be investigated with the current platform. A computational fluid dynamics approach, thought outside the scope of the modeling effort hereby presented, might be necessary if one wished to accurately model this behavior; however, an experimental approach might be just as productive. A suggestion for future work is to remake the fluid chamber (and/or the pump chamber) with a of see-through material such as acrylic or polycarbonate, and characterize the true vibrational dynamics of the liquid-piston under load with the help of a high-speed video camera. Based on the observed dynamics, the silicone diaphragms could be cast in certain shapes such that the localized flow forces acting on them are neutralized. Figure 6-16 shows an example of membranes cast with different suggested shapes: concave(top), wavy (left) and convex (right).

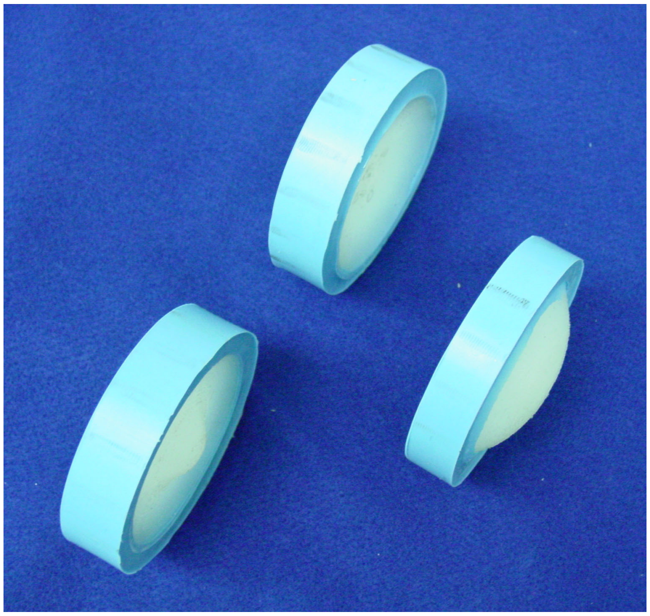

Figure 6-16: Silicone Membranes Cast With Different Shapes.

CHAPTER VII

CONCLUSIONS

This dissertation presented the design, modeling, simulation, fabrication, and experimental characterization and model validation of a free liquid-piston engine compressor (FLPC). The FLPC is a combustion-driven air compressor proposed as a portable power source candidate for untethered pneumatic robots of up-to human-scale power (100 Watts). The combined factors of high energy density of hydrocarbon fuels, high energy conversion efficiency (relative to comparable small-scale internal combustion engines and air compressors), compactness and low weight of the device, and its intended ability to drive power dense pneumatic actuators (relative to DC motors), are projected to provide at least a twofold increase in systems-level energy and power densities over state-of-the art electromechanical human-scale robotic systems.

It has been shown that a free-piston engine configuration with an over-expanded engine cycle can yield high efficiency with quiet and low temperature operation. This is due to the fact that a free-piston with a compressor load offers very low output impedance to the rapid-expanding combustion gases, and can thus efficiently transduce their energy into kinetic energy of the free piston, which in turn can efficiently provide the work required to compress air and pump it into a reservoir.

A custom design was presented in Chapter II. The free liquid-piston consists of a slug of water trapped between custom-made elastic silicone membranes. This configuration eliminates typical blow-by leakage through piston rings, as well as energy losses associated with sliding friction. In addition, the liquid-piston configuration allows for a hemispherical compressor design, which ideally matches the spherical-segment contour of the piston expansion profile, and allows for minimal dead volume in the pump chamber. In addition, an integrated reservoir was included, and custom low-profile inlet and outlet check valves were built into the pump chamber.

Perhaps the most notable design contribution presented in this work is the inclusion of a separated combustion chamber. In short, this is a constant-volume chamber where combustion occurs, and whose high-pressure combustion gases are quickly and effectively flowed into an expansion chamber in which they perform PV work on the free-piston. A magnetically-held high-flow passive "combustion valve" dictates the flow conditions: remain fully closed during air/fuel injection, and quickly open immediately after ignition. This combustion scheme decouples the fuel injection dynamics from the free-piston dynamics allowing for high frequency operation. The implementation of this separated combustion chamber solves the problem of scavenging (typical of 2-stroke engines) and issues associated with starting and stopping the engine, since there is no idle.

A dynamic model of the device was introduced in Chapter III, most notably treating thermodynamic relations in a time-varying context, thereby coupling them to inertial and other dynamic elements of the system. This unusual approach allowed for a full dynamic model that can relate the thermodynamic states of the system to the rapidly changing valve and piston dynamics. Experimental results showed a very close match to the model in Chapter V, and demonstrated the usefulness of the model as a reliable diagnostic tool as well as a valuable asset for future research. Consequently, in Chapter VI, the model was used precisely as a diagnostic tool to evaluate the issues that hindered the achievement of reliable continuous operation, and most importantly, design recommendations for future research endeavors were postulated, and hereby summarized:

- **"Flattened" Expansion Chamber –** The expansion side was originally designed as a spherical segment in order to accommodate for an overshoot in the return (exhaust) stroke. Careful timing needs to be achieved in order to coincide a combustion event with the precise moment at which the liquid piston reaches the leftmost point in its stroke, otherwise resulting in inefficient cycles. It is strongly advised to re-fabricate the expansion side with no room for overshoot, in order to eliminate the need for careful timing and thus have a more robust experimental platform. Overshoot space might be considered again in the future once other control issues are solved.
- **Stronger Magnet –** The NdFeB magnet implemented in the FLPC was a readily available commercial product, which initially was thought to provide adequate holding force capacity. However, upon analyzing the experimental behavior along with the validated model, it was determined that a stronger magnet should be used. This would require a custom design for both a strong encased magnet and a magnet housing (i.e., "end cap"). If the new magnet requires a larger diameter, then a new ferrous plate would also need to be designed for the valve keeper.
- **Clear Walled Fluid Chamber –** The fluid chamber should be re-fabricated with a clear (i.e., "see-through") material, in order to observe the vibrational dynamics of the liquid piston. This could be done with a high-speed video camera, and based on the observed vibrational mode of the piston, new shapes could be devised for the

diaphragms that can counterbalance any undesired dynamics, and result in a smooth spherical segment volumetric displacement.

Finally, successful experimental high-pressure pumping was achieved (though somewhat scattered throughout the data) and shown in Chapter V, both in "open loop" (air for combustion externally supplied) and "closed loop" (air for combustion supplied from its own reservoir) configurations. An isolated closed loop event that achieved positive net pump was examined and its overall power potential and efficiency were characterized at 50 Watts and 2%, respectively.

APPENDIX A

CIRCUIT SCHEMATICS

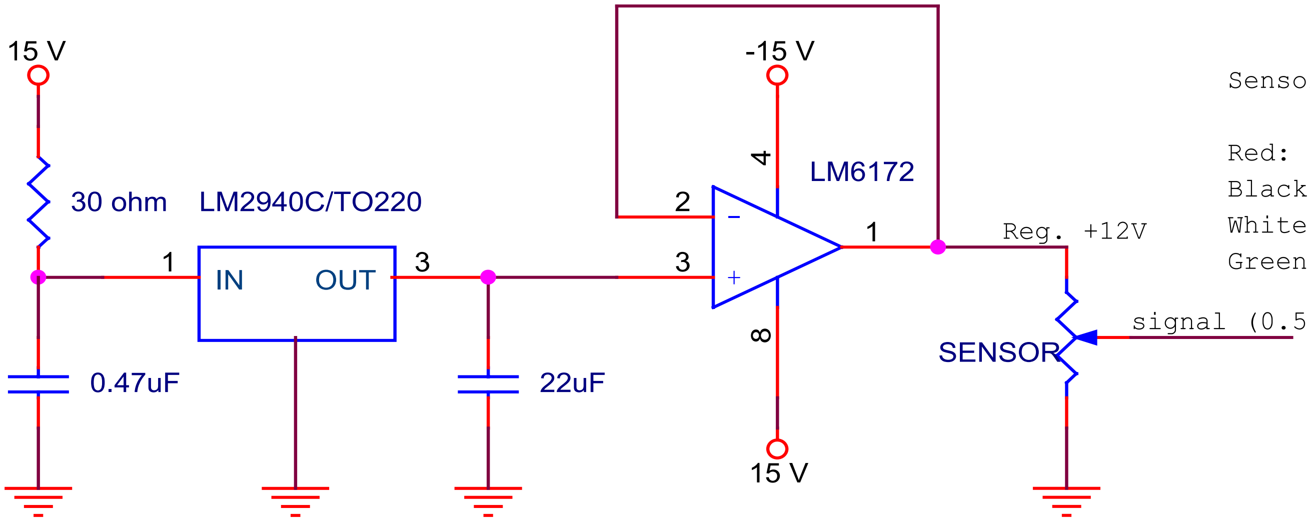

Sensor Wiring

Red: Supply
Black: Gnd
White: Signal
Green: Diagnostic (not needed)

Figure A-1: Signal Conditioning Circuit Schematics for Optrand Pressure Sensor

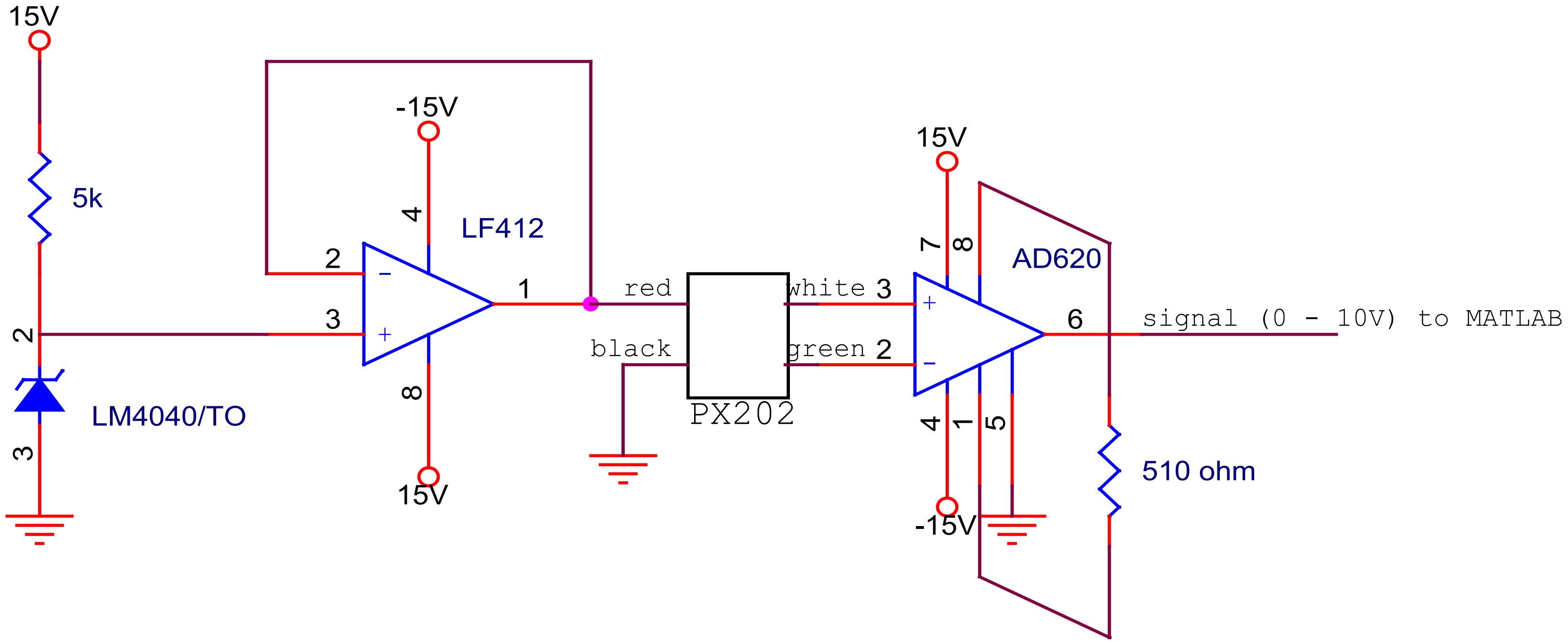

Figure A-2: Signal Conditioning Circuit Schematics for Omega PX202 Pressure Sensor

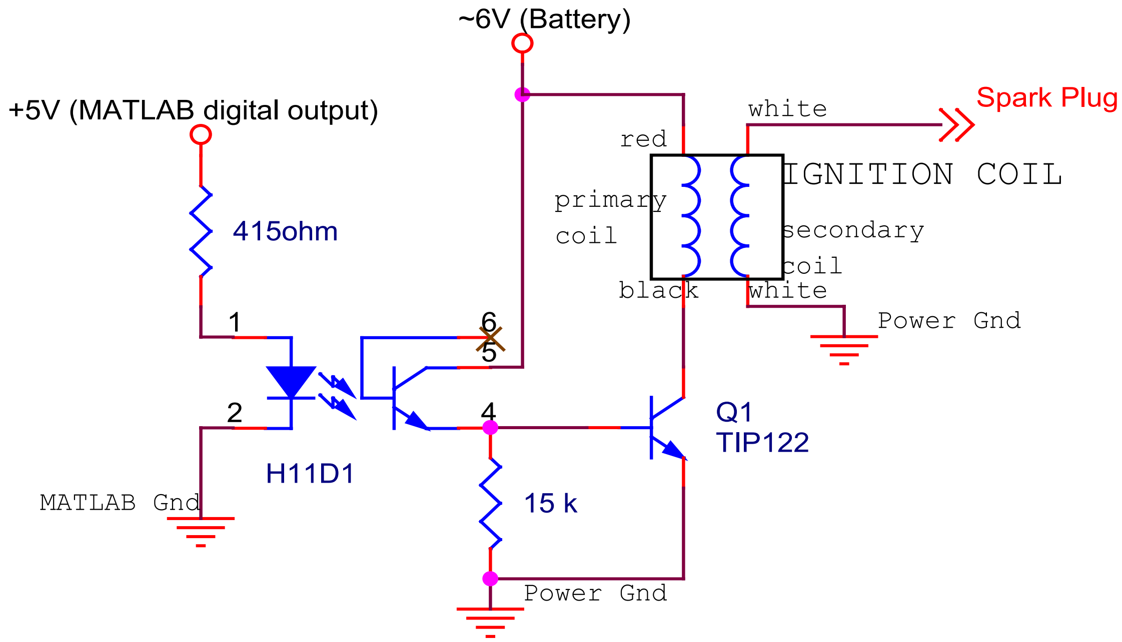

Figure A-3: Circuit Schematics for Ignition System

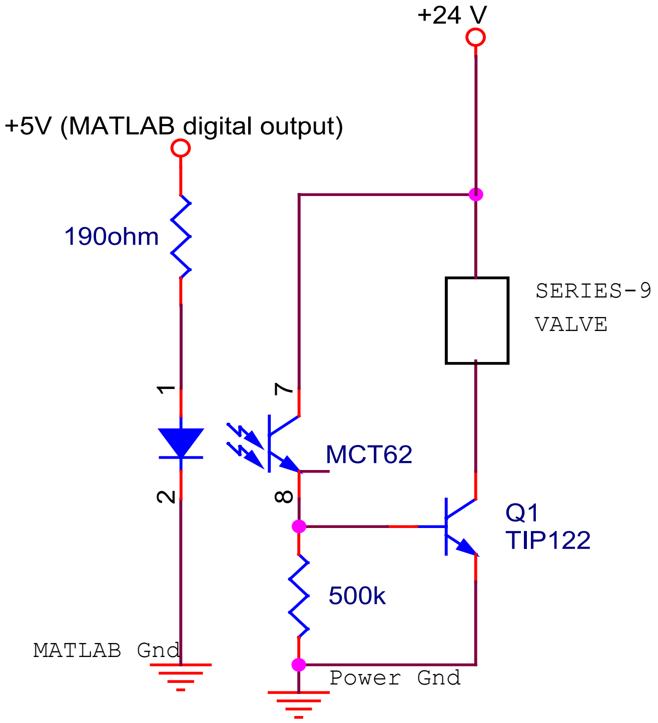

Figure A-4: Circuit Schematics for Series-9 Valve

APPENDIX B

SIMULATION DIAGRAMS

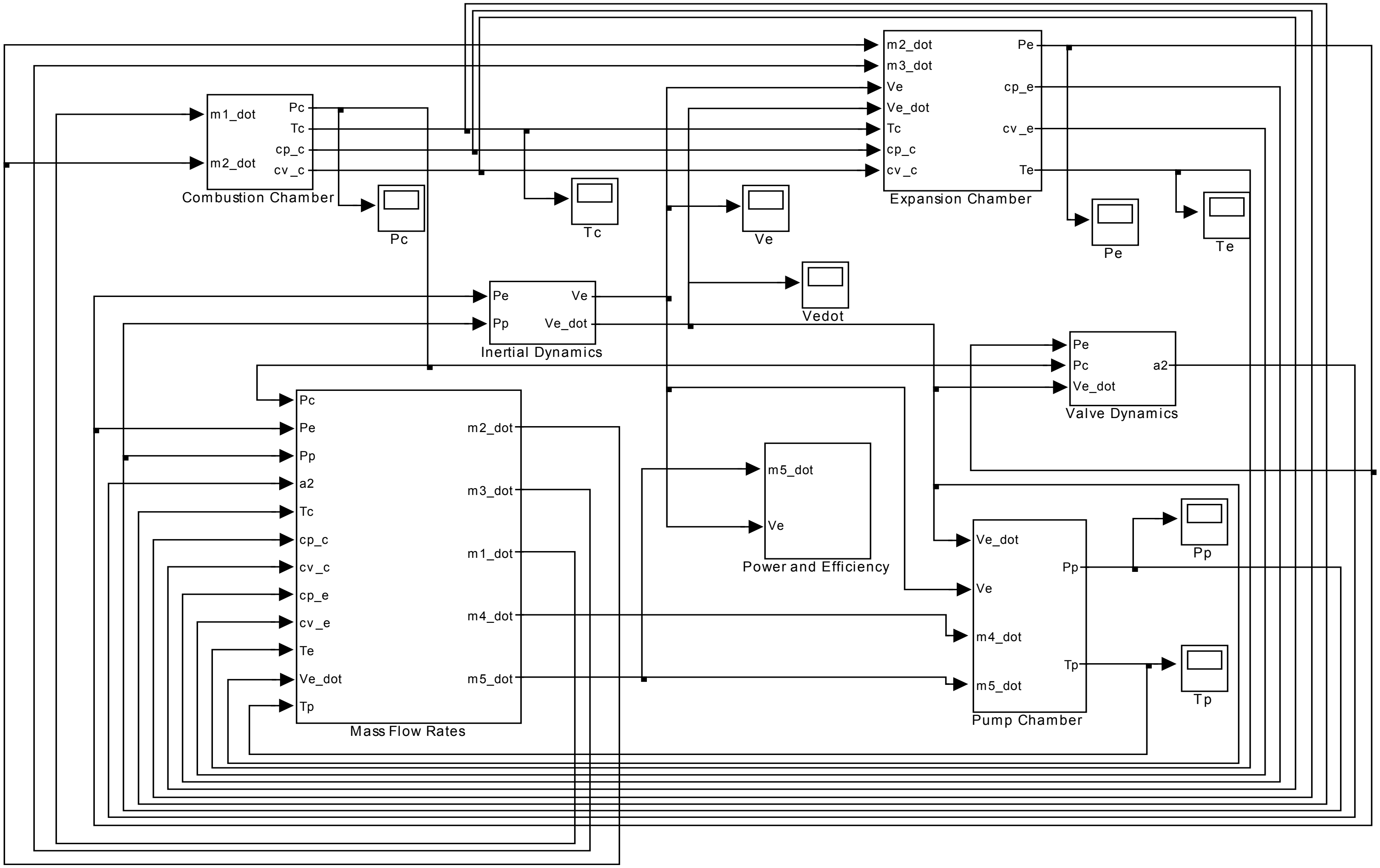

Figure B-1: Simulink Block Diagram of FLPC Simulation

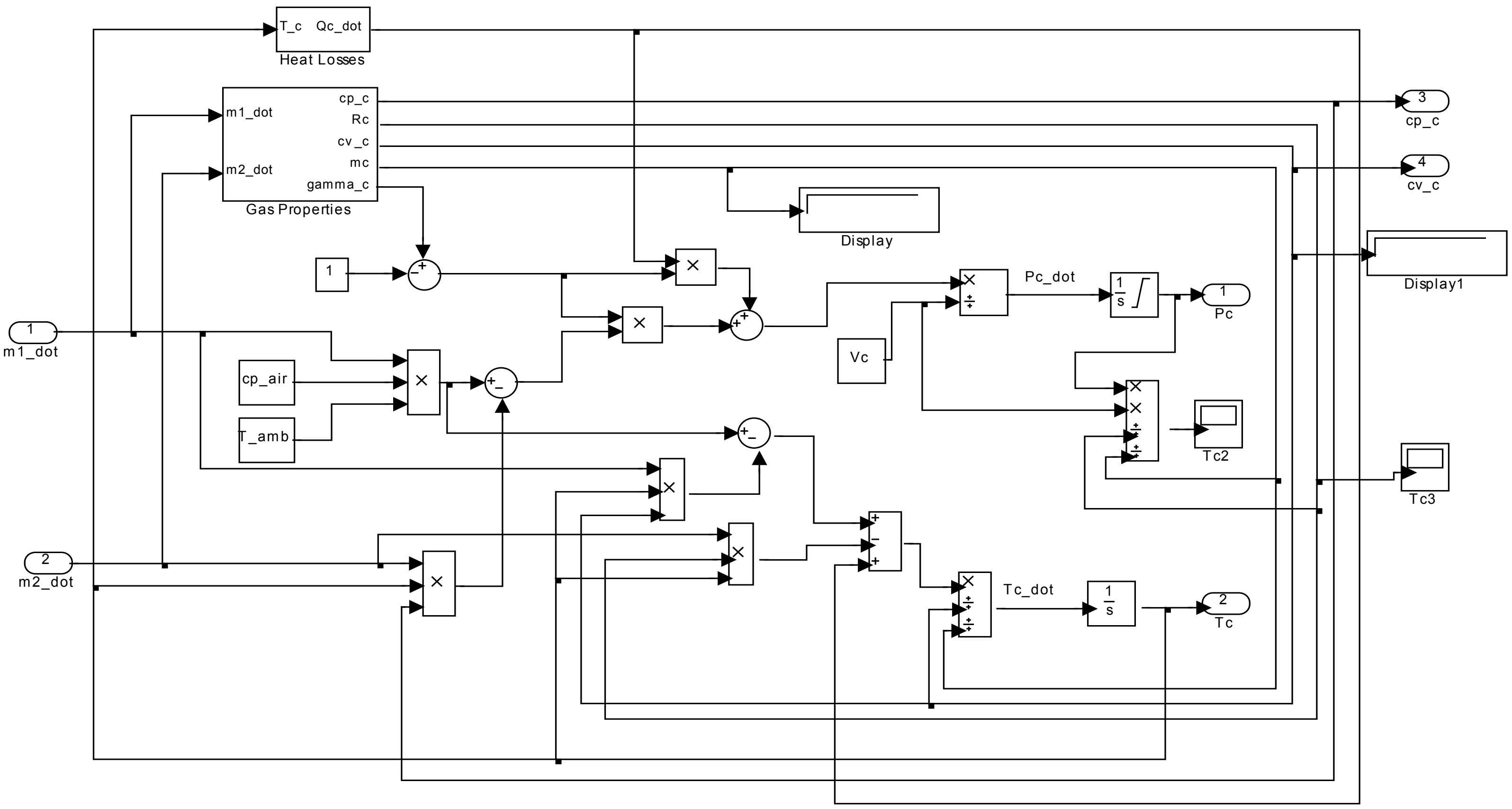

Figure B-2: Contents of Sub-Block "Combustion Chamber"

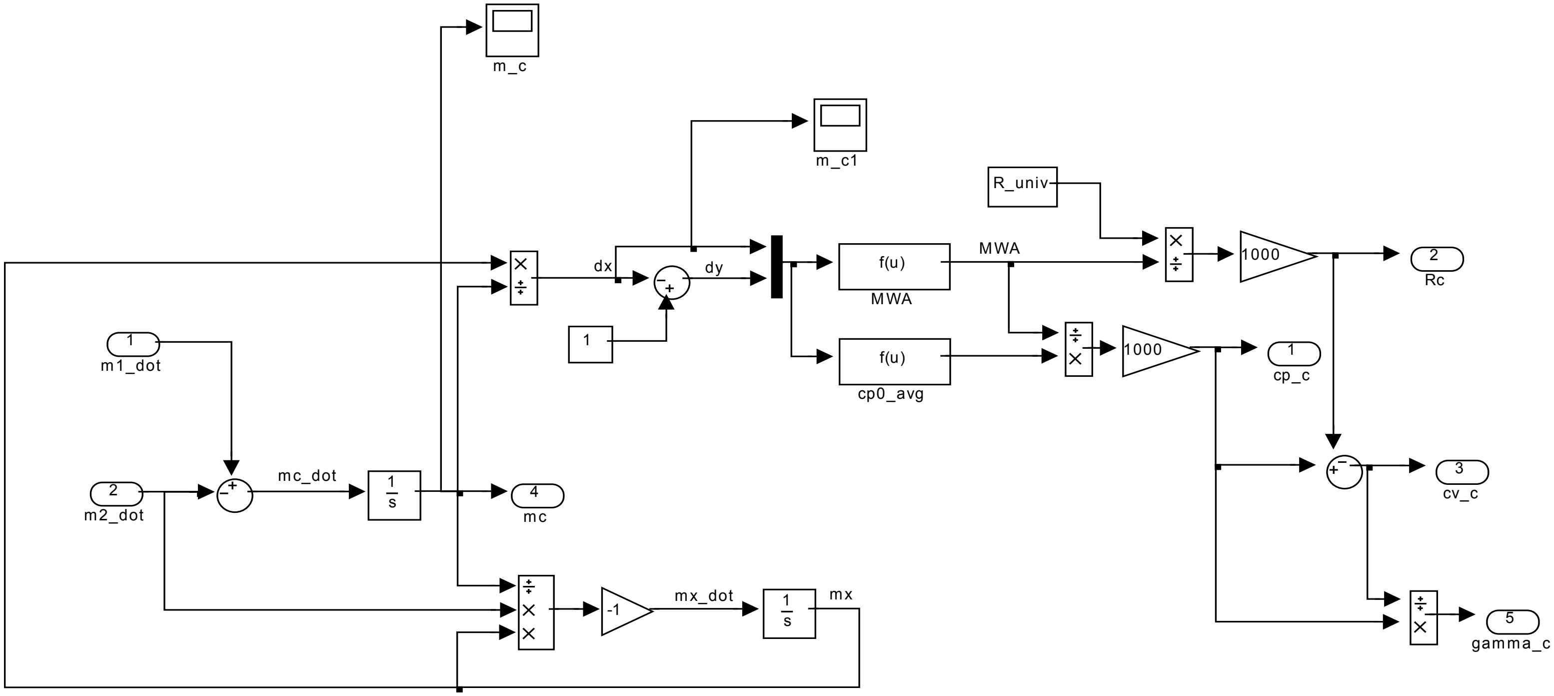

Figure B-3: Contents of Sub-Sub-Block "Gas Properties"

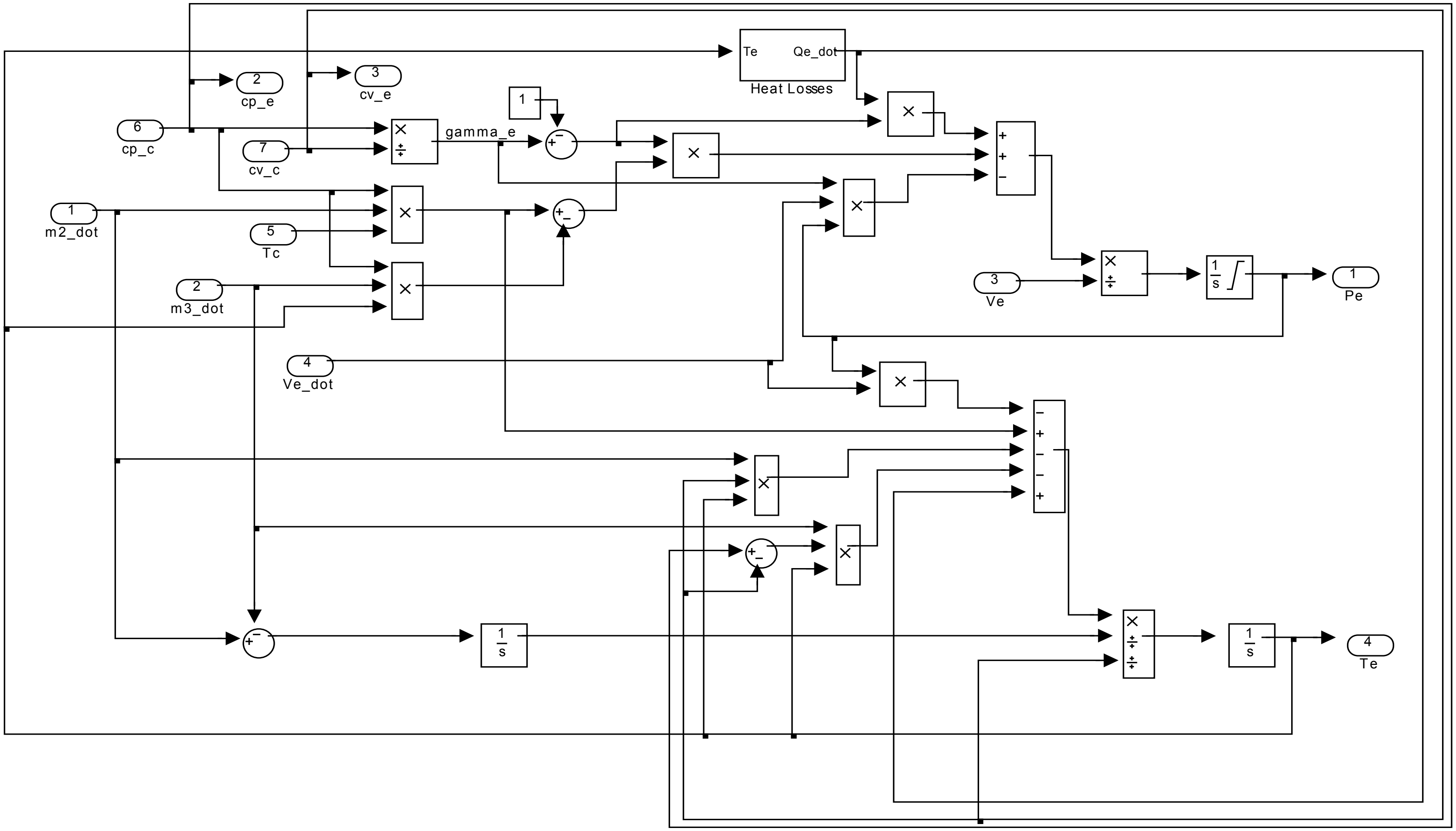

Figure B-4: Contents of Sub-Block "Expansion Chamber"

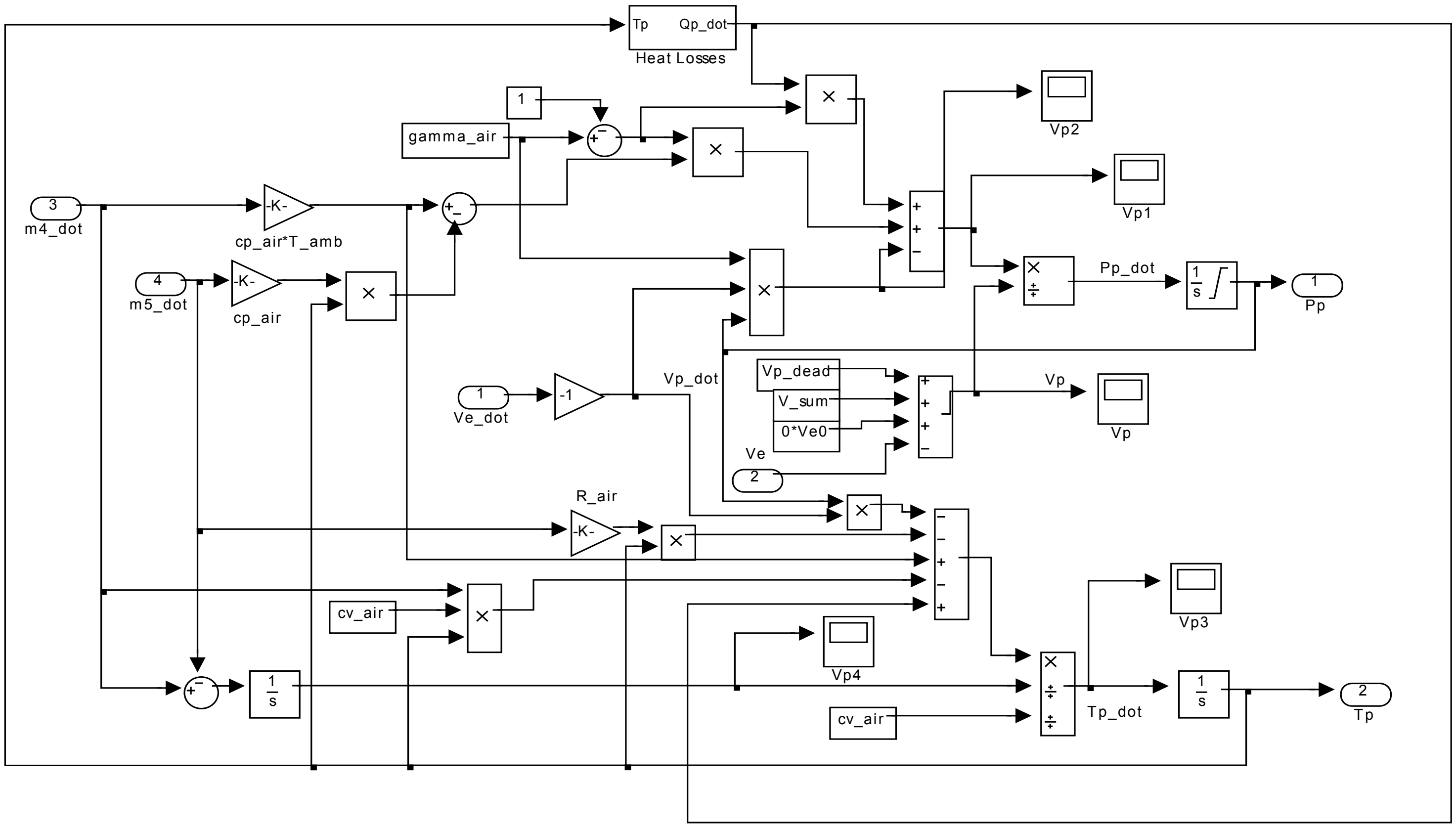

Figure B-5: Contents of Sub-Block "Pump Chamber"

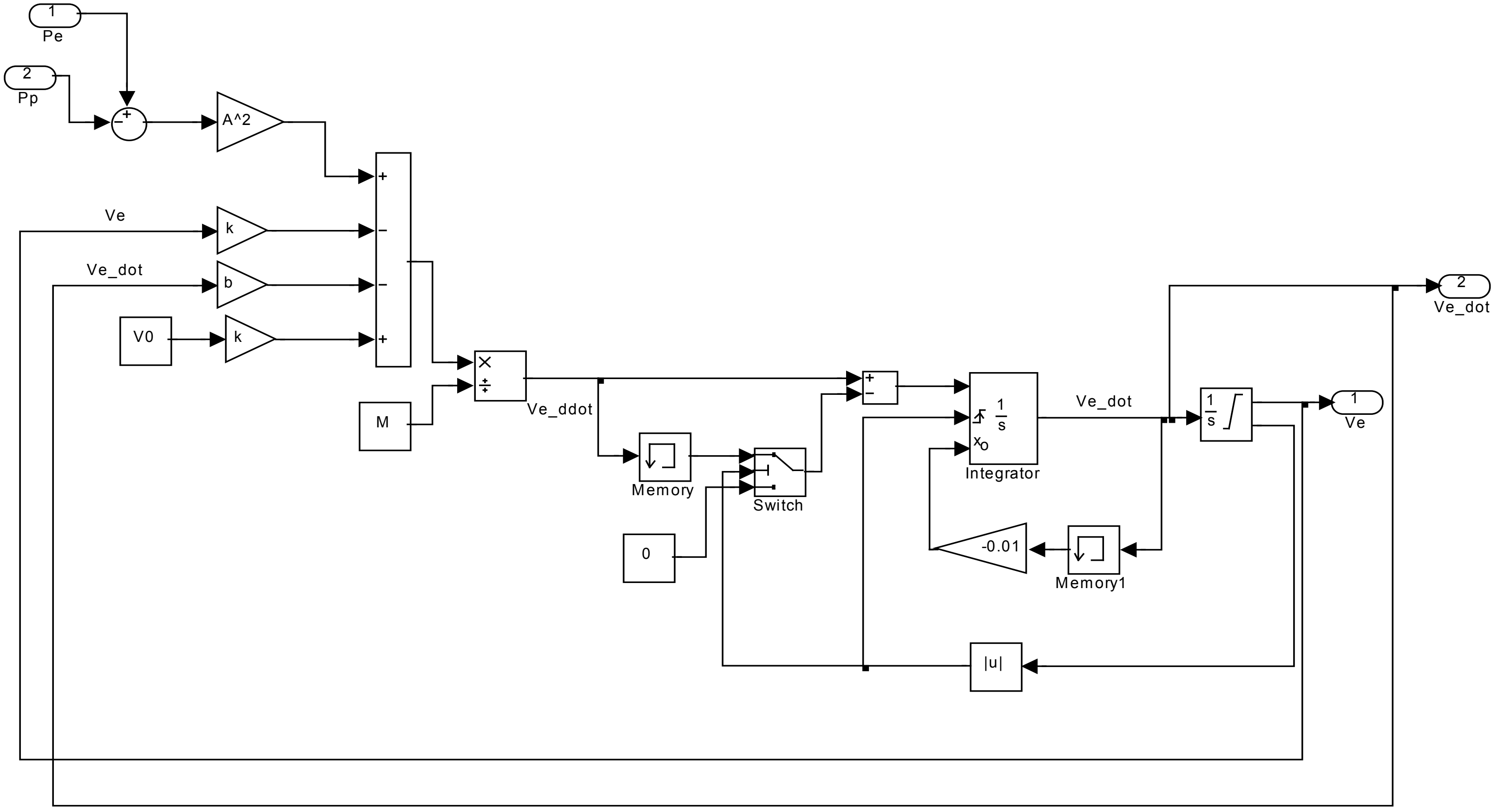

Figure B-6: Contents of Sub-Block "Inertial Dynamics"

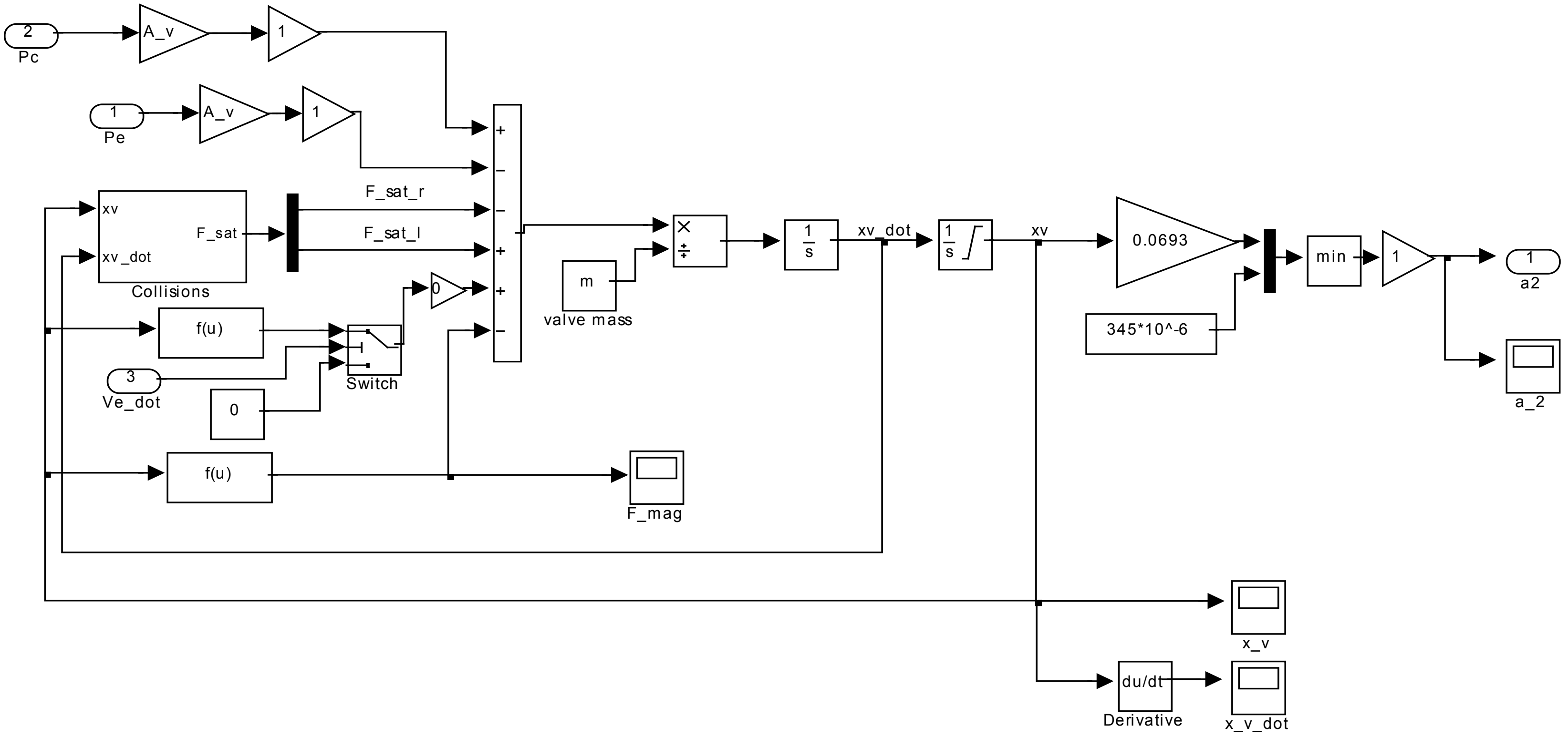

Figure B-7: Contents of Sub-Block "Valve Dynamics"

`

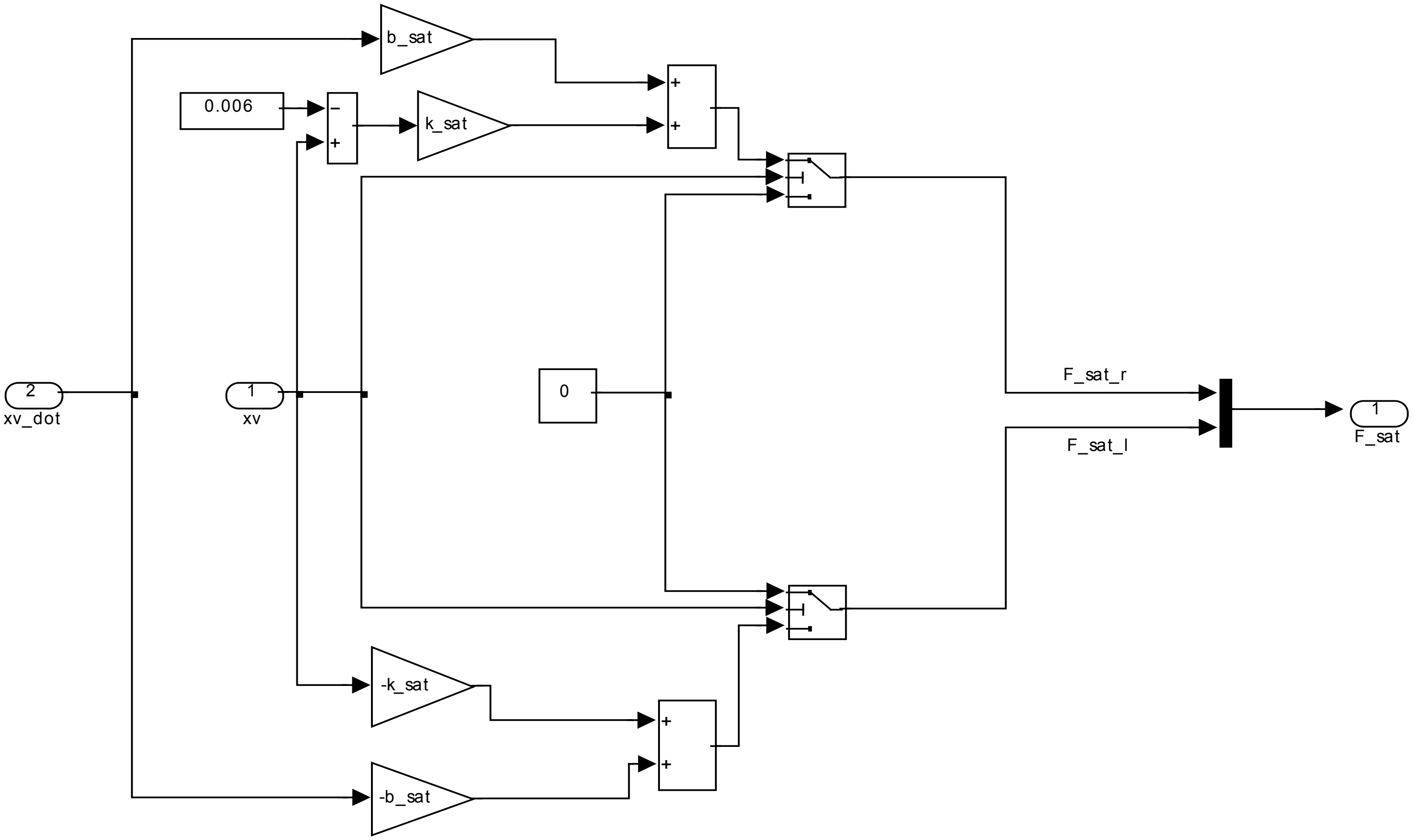

Figure B-8: Contents of Sub-Sub-Block "Collisions"

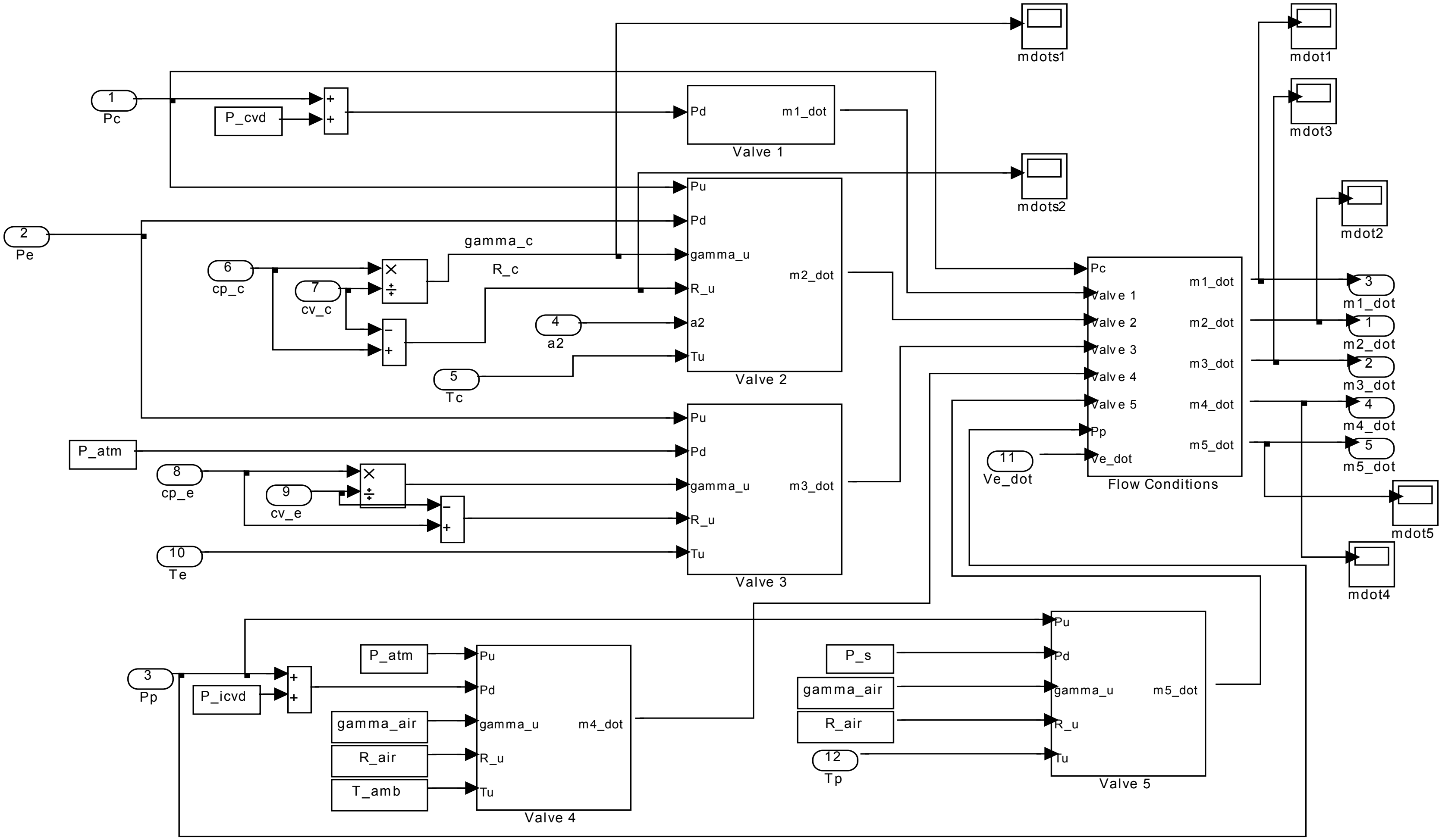

Figure B-9: Contents of Sub-Block "Mass Flow Rates"

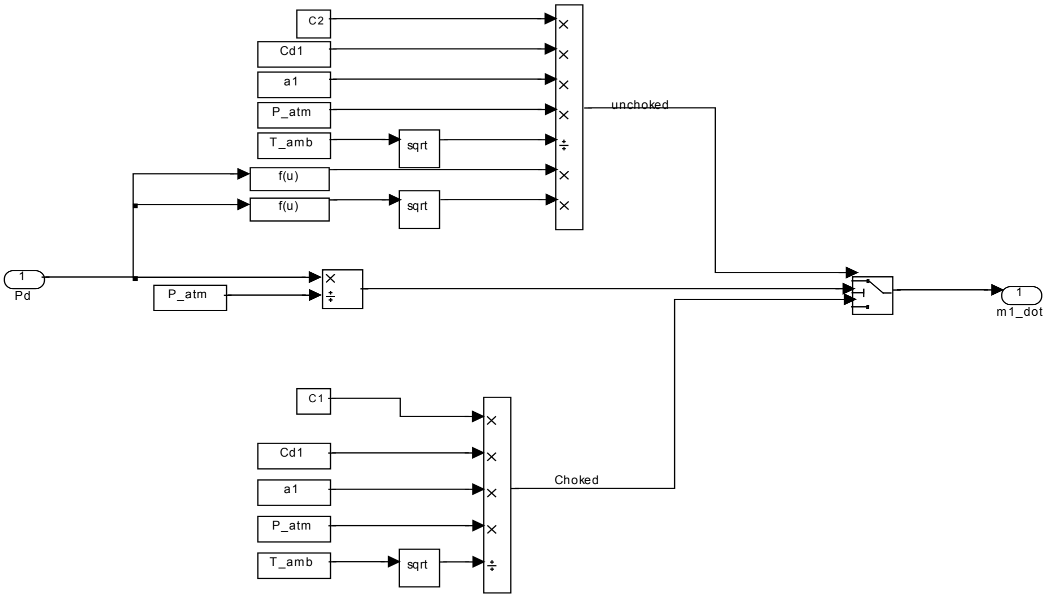

Figure B-10: Contents of Sub-Sub-Block "Valve 1"

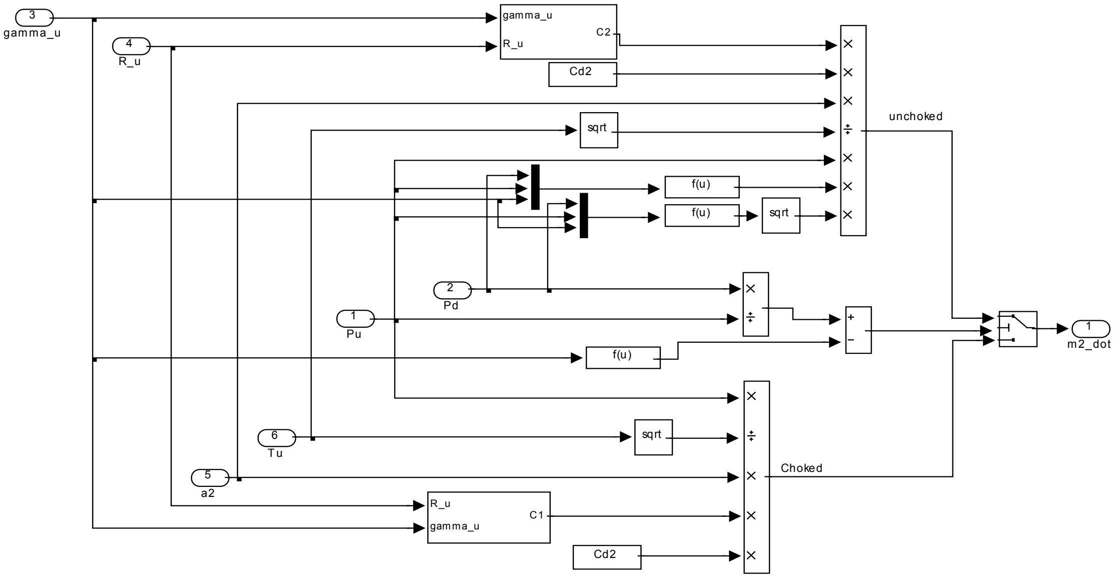

Figure B-11: Contents of Sub-Sub-Block "Valve 2"

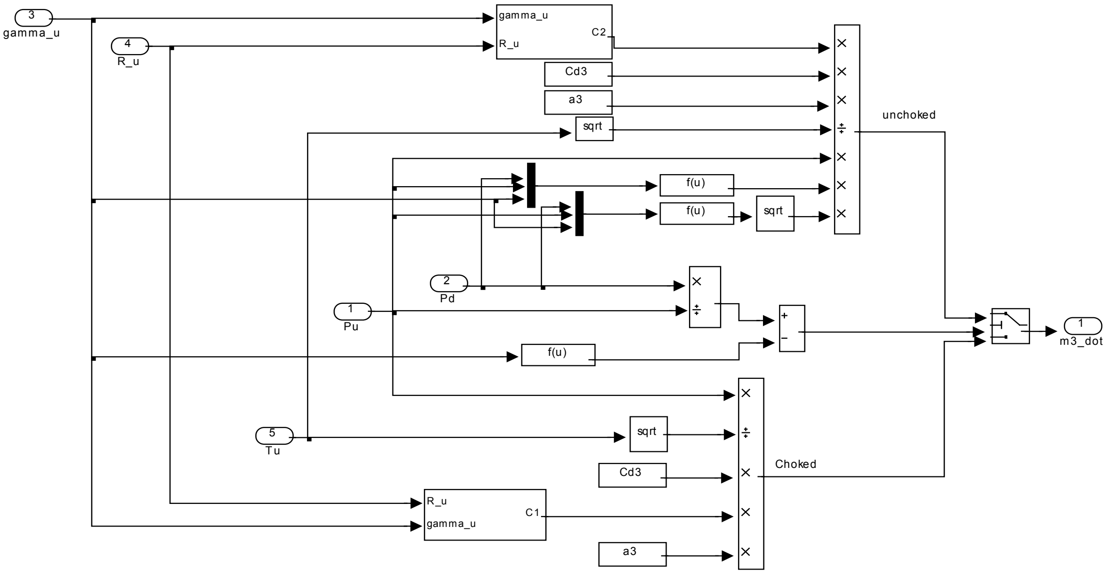

Figure B-12: Contents of Sub-Sub-Block "Valve 3"

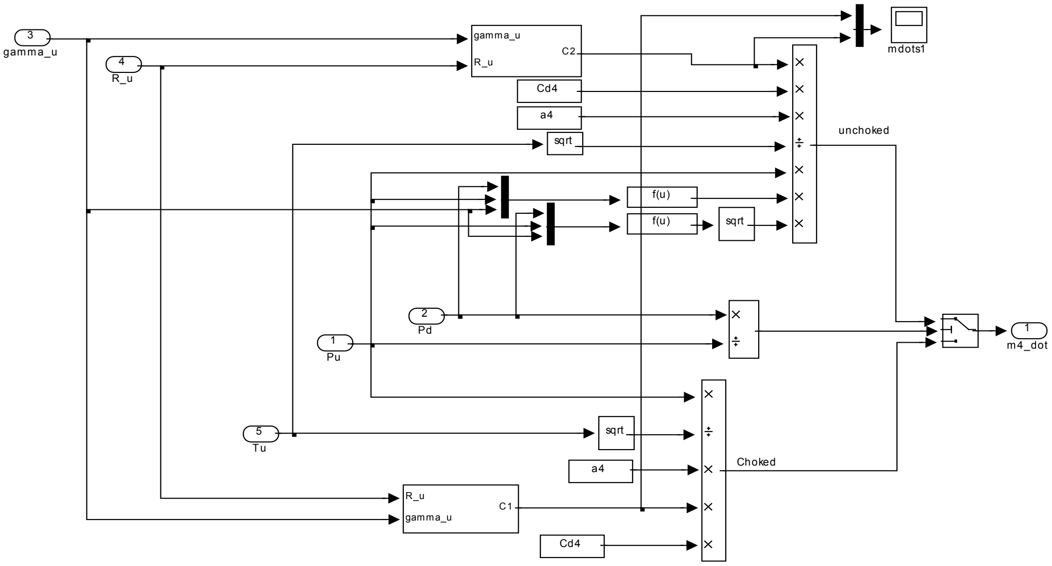

Figure B-13: Contents of Sub-Sub-Block "Valve 4"

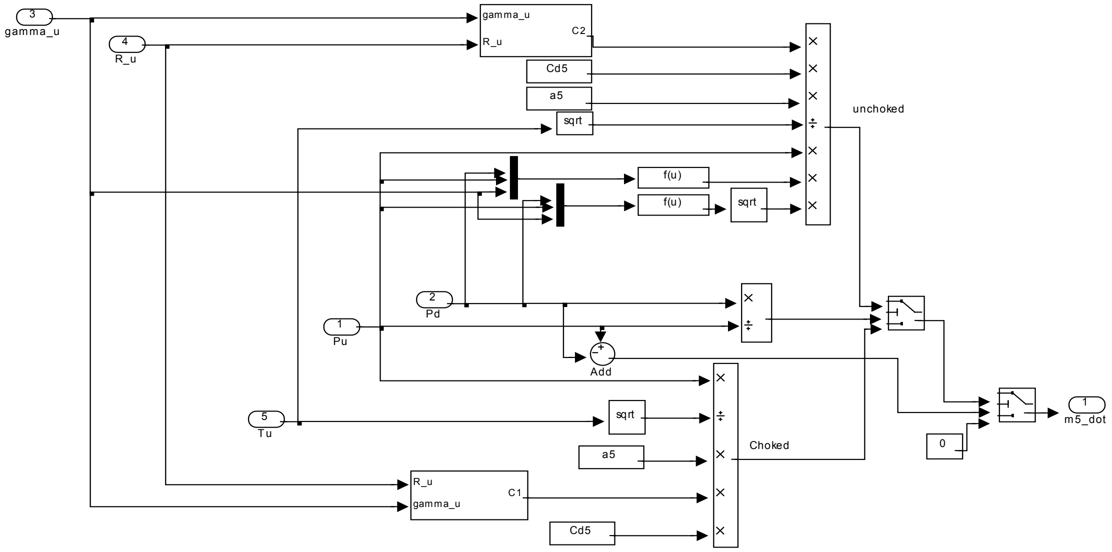

Figure B-14: Contents of Sub-Sub-Block "Valve 5"

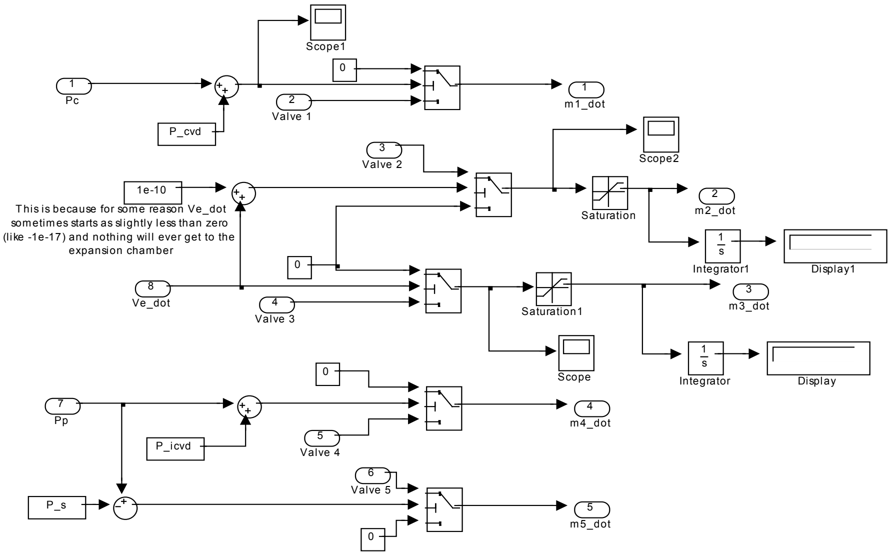

This is because for some reason Ve_dot sometimes starts as slightly less than zero (like -1e-17) and nothing will ever get to the expansion chamber

Figure B-15: Contents of Sub-Sub-Block "Flow Conditions"

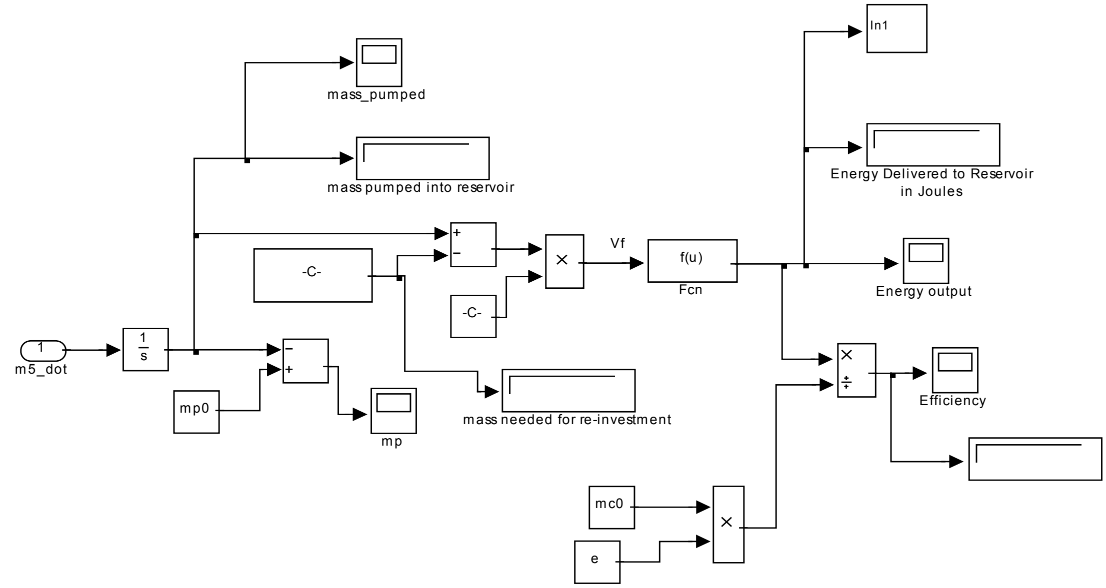

Figure B-16: Contents of Sub-Block "Power and Efficiency"

APPENDIX C

REAL-TIME WORKSHOP DIAGRAMS

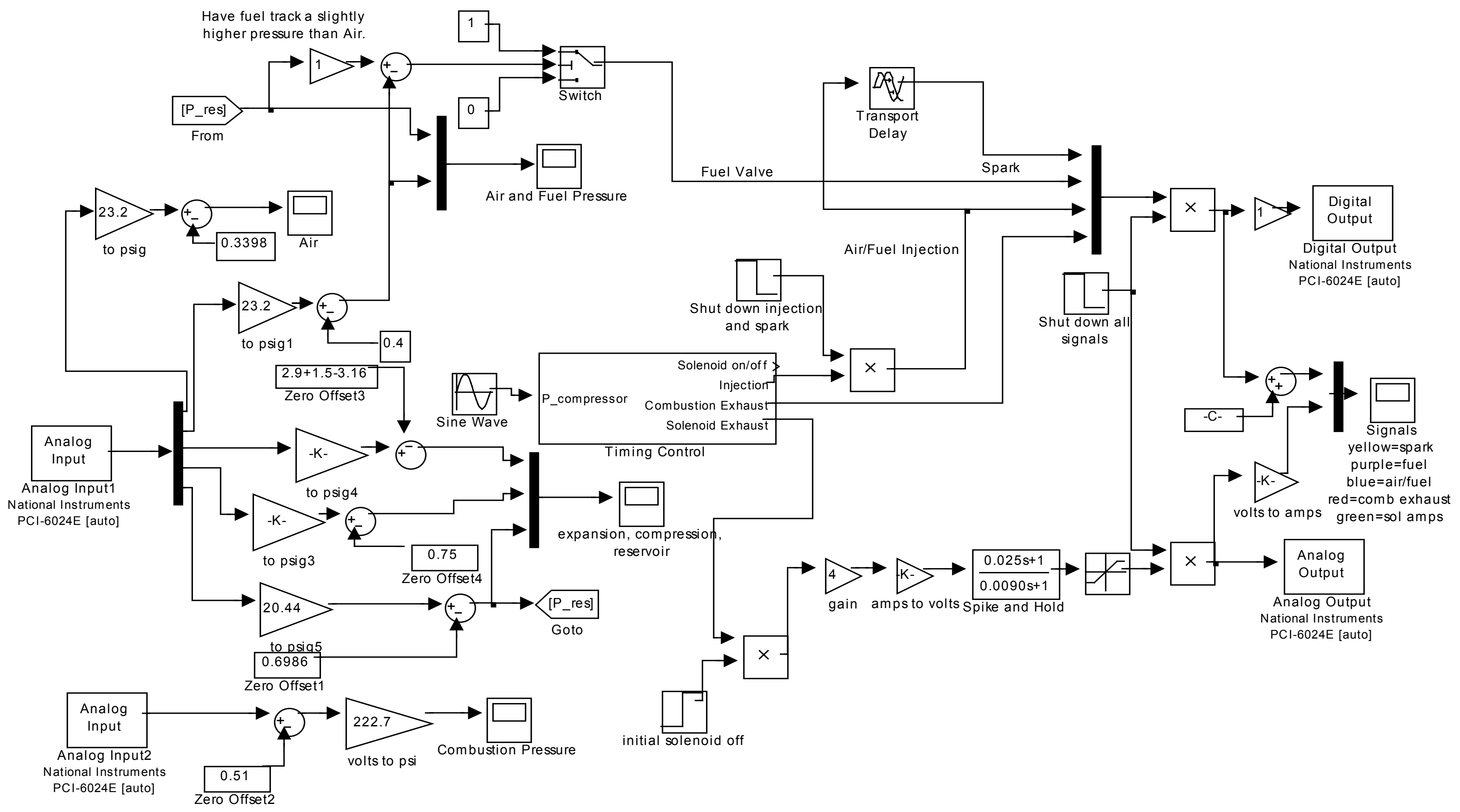

Figure C-1: Real-Time Workshop Diagram for Full Device Open Loop Operation ("Full_Device_OLcontrol.mdl")

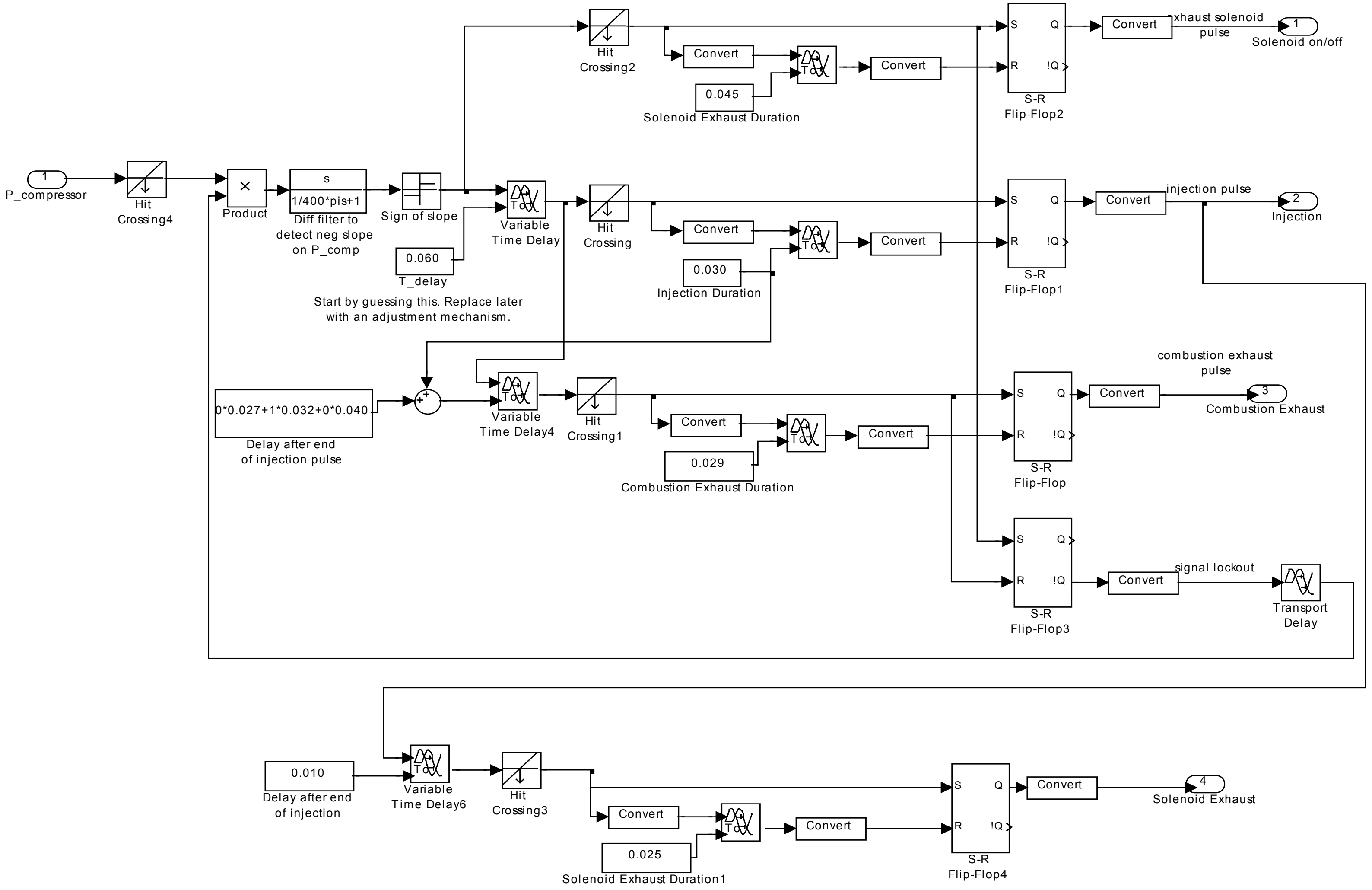

Figure C-2: Contents of Sub-Block "Timing Control"

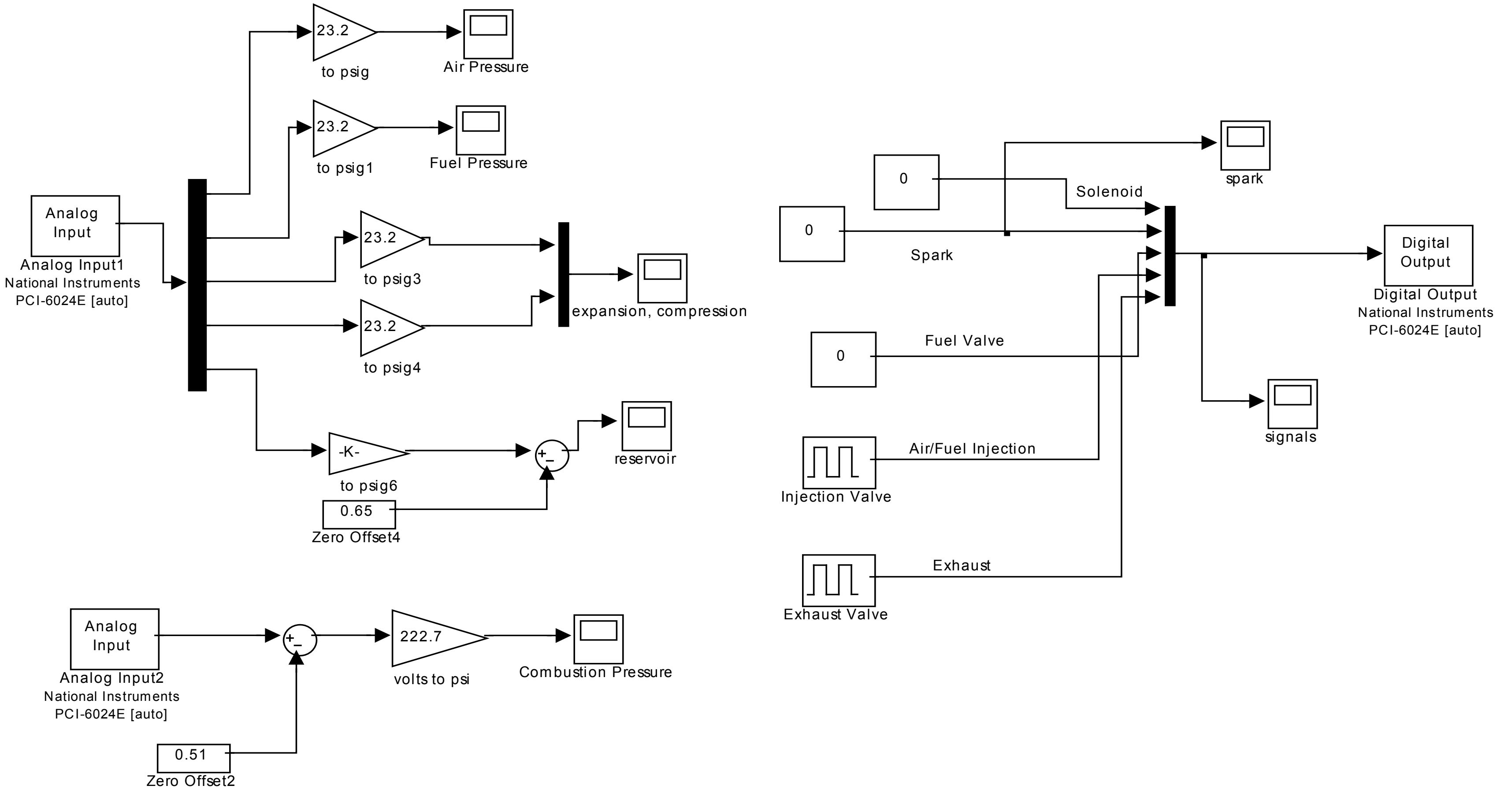

Figure C-3: Real-Time Workshop Diagram for Leak Test ("Full_leak_test.mdl")

APPENDIX D

MATLAB CODE

MATLAB m-file "ECEFP_init_dissertation.m"

This m-file initiates sets values for all simulation parameters used in the simulation model ("Simulation_Model_Dissertation.mdl").

```
clear all;


%% General Thermodynamic Constants

P_atm=101353; %Atmospheric pressure (in Pa)
T_amb=295; %Ambient temperature (in K)
T_aft=2250; %Adiabatic Flame Temperature (in K)
R_univ=8.3145; %Average gas constant (in J/mol/K)

%% Valve Constants

P_cvd=(1/3)*6895; %crack pressure of Parker check valves (in Pa) (from
1/3 psi)
P_icvd=0; %crack pressure of low-profile integrated check valve (in Pa)
a1=40*pi*((4.7/1000)/2)^2; %flow area of Parker check valve (in m^2)
(from 4.7 mm dia)
a3=1.27*58.6/(1000^2); %flow area of exhaust valve (in m^2) (from 58.6
mm^2)
a4=42*(pi*((0.055*0.0254)/2)^2); %flow area of low-profile integrated
check valve (in m^2) (from 42 0.055 dia holes)
a5=396*(pi*((0.055*0.0254)/2)^2); %flow area of pump outlet check valve
(in m^2)
Cd1=0.5; %discharge coefficient of Parker breathe in check valve (no
dim)
Cd2=0.95; %discharge coefficient of combustion valve (no dim)
Cd3=0.95; %discharge coefficient of exhaust valve (no dim)
Cd4=0.95; %discharge coefficient of low-profile integrated check valve
(no dim)
Cd5=0.9; %Discharge coefficien of outlet check valve (no dim)
Cd6=0.95; %Discharge Coefficient of combustion exhaust


%% Inertial and Geometrical Constants

M=0.5; %mass of liquid piston (in kg)
k=2000; %effective diaphragm stiffness (in N/m)
zeta=0.21; % question: does the free trapped liquid slug really have a
zeta this low?
b=sqrt(4*zeta^2*k*M); %effective viscous friction (in N*s/m)
r=1.5*0.0254; %radius of cross-section (in m) (from in.)
V0=1/3*pi*r^3; %volume in expansion chamber at which diaphragms are
relaxed (in m^3)
A=pi*r^2; % cross-sectional area of fluid chamber (in m^2)
V_sum=pi*r^3; %constant sum of expansion and pump volumes (in m^3)
m=0.1048; %mass of combustion valve (in kg)
m_ex_valve = 0.2;%mass of expansion exhaust valve (in kg)
A_v=pi*(0.028/2)^2; %Area of combustion valve head (in m^2) (from 28 mm
dia)
A_v_rod = pi*(0.005/2)^2;
k_sat=1e9; %collision stiffness (in N/m)
```

```
b_sat=1e6; %collision damping (in N*s/m)
%P_s=94.7*6895; %Pressure in reservoir (in Pa) (from 94.7 psi)
P_wall=72.7*6895;%pressure of external air supply
C_mag=0.0014; %Permanent magnet proportionality constant (nominal
0.0008)

%% Gas Properties of Air

cp_air=1012; %constant pressure specific heat (in J/kg/K)
cv_air=723.7; %constant volume specific heat (in J/kg/K)
R_air=cp_air-cv_air; %gas constant (in J/kg/K)
gamma_air=cp_air/cv_air; %ratio of specific heats (no dim)
Cr_air=(2/(gamma_air+1))^(gamma_air/(gamma_air-1)); % Condition for
choked or unchoked flow

%% Gas Properties of Combustion Products

cp_prod=1473; %constant pressure specific heat (in J/kg/K)
cv_prod=1179; %constant volume specific heat (in J/kg/K)
R_prod=cp_prod-cv_prod; %gas constant (in J/kg/K)
gamma_prod=cp_prod/cv_prod; %ratio of specific heats (no dim)

%% Gas Properties of Injection Mixture

P_inj=635141; % injection pressure (in Pa)
e=46350000/16.63; %mass energy constant of propane/air mixture (in
J/kg)

%% Initial Conditions in Combustion Chamber

Vc=1.2290298*10^-5; %constant volume (in m^3) (from 0.75 in ^3)
Tc0=4.2/7.7821*T_aft; %combustion temperature (in K)
Pc0=Tc0/T_amb*P_inj; %combustion Pressure (in Pa)
%Pc0=2.54e6; %combustion Pressure (in Pa) (from 368.5 psi)
Rc0=R_prod; %initial gas constant(in J/kg/K)
%mc0=P_inj*V_inj/(R_inj*T_amb);
mc0=Pc0*Vc/(Rc0*Tc0); %initial mass of gases(in kg)

%% Initial Conditions in Expansion Chamber

Pe0=P_atm; %initial pressure (in Pa)
Te0=T_amb; %initial temperature (in K)
Ve0=0*V0+1e-6;%1e-5; %initial volume (in m^3) - note: start Ve0=0.99*V0
to study start-up, otherwise Ve0=1e-7
Re0=R_prod; %initial gas constant (in J/kg/K)
me0=Pe0*Ve0/(Re0*Te0); %initial mass of gases (in kg)

%% Initial Conditions in Pump Chamber

Vp_dead=1e-6; %dead volume in pump chamber
Pp0=P_atm; %initial pressure (in Pa)
Tp0=T_amb; %initial temperature (in K)
Vp0=V_sum-Ve0; %initial volume (in m^3)
mp0=Pp0*Vp0/(R_air*Tp0); %initial mass of air (in kg)
```

```
%% Initial Conditions in Reservoir

P_s=77.6*6895; %Pressure in reservoir (in Pa) (from 94.7 psi)
V_res = 6.66e-4; %Volume of the reservoir (in m^3)
m_s0=P_s*V_res/R_air/T_amb; %Mass of air in reservoir

%% 2nd Order combustion model

zeta_comb = 1;
Wn_comb = 0.05;
gamma_comb = 1.4;
```

MATLAB m-file "dissertation_plots.m"

This m-file plots simulation results with nominal parameters (m=0.5 kg, k=2000 N/m). These plots are Figures 3-3 through 3-7 in the document.

```
close all;
clear all;
load dissertation;

%% Pressure Plots
figure(1);
plot(P_combustion(:,1)*1e3, P_combustion(:,2)*1e-6,'k--
','LineWidth',2);
hold on;
plot(P_expansion(:,1)*1e3, P_expansion(:,2)*1e-6,'r-.','LineWidth',2);
hold on;
plot(P_pump(:,1)*1e3, P_pump(:,2)*1e-6,'LineWidth',2);
grid;
axis([0,15,0,3]);
title('Combustion, Expansion and Pump Pressures');
xlabel('Time (ms)');
ylabel('Pressure (MPa)');
legend('Combustion Chamber','Expansion Chamber','Pump Chamber');

%% Volume Plot
figure(2);
plot(V_expansion(:,1)*1e3, V_expansion(:,2)*1e6,'LineWidth',2);
grid;
title('Volume in Expansion Chamber');
xlabel('Time (ms)');
ylabel('Volume (cc)');
axis([0,25,0,165]);

%% Temperature Plots
figure(3);
plot(T_combustion(:,1)*1e3, T_combustion(:,2),'k--','LineWidth',2);
hold on;
plot(T_expansion(:,1)*1e3, T_expansion(:,2),'r-.','LineWidth',2);
hold on;
plot(T_pump(:,1)*1e3, T_pump(:,2),'LineWidth',2);
grid;
axis([0,15,200,1400]);
title('Combustion, Expansion and Pump Temperatures');
xlabel('Time (ms)');
ylabel('Temperature (K)');
legend('Combustion Chamber','Expansion Chamber','Pump Chamber');

%% Mass Flow Rate Plots

figure(4);
plot(m2dot(:,1)*1e3, m2dot(:,2),'k','LineWidth',2);
hold on;
plot(m5dot(:,1)*1e3, m5dot(:,2),'b-.','LineWidth',2);
grid;
```

```
axis([0,15,0,0.2]);
title('Mass Flow Rates: Combustion Valve and Pump');
xlabel('Time (ms)');
ylabel('Mass Flow Rate (kg/s)');
legend('Combustion Valve','Pump Outlet');

figure(5);
plot(m1dot(:,1)*1e3, m1dot(:,2),'k--','LineWidth',2);
hold on;
plot(m3dot(:,1)*1e3, m3dot(:,2),'r-.','LineWidth',2);
hold on;
plot(m4dot(:,1)*1e3, m4dot(:,2),'b:','LineWidth',2);
grid;
axis([0,25,0,0.018]);
title('Mass Flow Rates: Breathe-in, Exhaust and Pump Inlet');
xlabel('Time (ms)');
ylabel('Mass Flow Rate (kg/s)');
legend('Breathe-in','Exhaust','Pump Inlet');


%% PV-diagrams
figure(6);
P_adb=2.615e6*(1.239e-5./V_expansion(:,2)).^gamma_prod;
plot(V_expansion(:,2)*1e6+Vc*1e6,P_expansion(:,2)*1e-6,'k--
','LineWidth',2)
hold on;
plot(V_expansion(:,2)*1e6,P_adb*1e-6,'r-.','LineWidth',2);
hold on;
plot(V_expansion(:,2)*1e6+Vc*1e6,P_combustion(:,2)*1e-
6,'b:','LineWidth',2);
axis([0 200 0 3]);
grid;
title('PV Diagrams');
xlabel('Volume (cc)');
ylabel('Pressure (MPa)');
legend('1','2','3');

%% Pneumatic PE in combustion and expansion chamber
PE_comb_exp=((P_combustion(:,2)).*(V_expansion(:,2)+Vc)/(1-
gamma_prod)).*((P_combustion(:,2)/P_atm).^((1-gamma_prod)/gamma_prod)-
1);
%% Kinetic energy of free piston
KE_fp=0.5*M*(V_expansion1(:,2)./A).^2;
%% Kinetic energy of combustion valve
KE_cv=0.5*m*(x_valve_dot).^2;
%% Pneumatic PE in compression chamber
PE_comp=(P_pump(:,2)).*(V_pump(:,2))/(1-
gamma_air).*((P_pump(:,2)./P_atm).^((1-gamma_air)/gamma_air)-1);
%% Pneumatic potential put in reservior
%mass_pumped=mp0-P_pump1(:,2)-15.67/16.67*mc0; %removes investment for
next combustion
mass_res=mass_pumped;
index=0;
if 1,
    for j=1:1:length(pump_end_delay),
        if pump_end_delay(j,2)==max(pump_end_delay(:,2)),
            index=j;
```

```
            break;
        end
    end
end

if 1,
    for i=index:1:length(pump_end_delay);
        %mass_res(i,2)=mass_pumped(length(mass_pumped),2)-
15.67/16.67*mc0;
        mass_res(i,2)=0.0001;
    end
end
vf=mass_res(:,2)*R_air*T_amb/P_s; %partial volume pumped (with heat
losses)
PE_res=vf*P_s/(1-gamma_air)*((P_s/P_atm)^((1-gamma_air)/gamma_air)-1);

%PE_res(12300:length(V_expansion(:,1)))=PE_res(12300:length(V_expansion
(:,1)))+offset;
%% PE spring
PE_spring=0.5*k*((V_pump(:,2)-V0)/A).^2;
%% Plot all energies
figure(7)
plot(V_expansion(:,1)*1e3, PE_comb_exp,'b','LineWidth',2);
hold on
plot(V_expansion(:,1)*1e3, KE_fp,'r','LineWidth',2);
plot(V_expansion(:,1)*1e3, PE_comp,'g','LineWidth',2);
plot(V_expansion(:,1)*1e3, PE_res,'m','LineWidth',2);
plot(V_expansion(:,1)*1e3, KE_cv,'k','LineWidth',2);
plot(V_expansion(:,1)*1e3, PE_spring,'c:','LineWidth',1);
plot(V_expansion(:,1)*1e3,
PE_comb_exp+KE_fp+KE_cv(:,2)+PE_comp+PE_res+PE_spring,'k:','LineWidth',
2);
axis([0 20 -5 65]);
%legend('Pneumatic PE Combustion and Expansion Chambers','Kinetic
Energy of Free Piston','Kinetic Energy of Combustion Valve','Pneumatic
PE of Compression Chamber','Pneumatic PE in Reservoir (after heat
loss)','Total Stored Energy')
legend('Pneumatic PE Combustion and Expansion Chambers','Kinetic Energy
of Free Piston','Pneumatic PE of Compression Chamber','Pneumatic PE in
Reservoir (after heat loss)','Kinetic Energy of Combustion
Valve','Elastic PE of diaphrams')
xlabel('Time (msec)');
ylabel('Energy (J)');
```

MATLAB m-file "simulated_parameter_variation_analysis.m"

This m-file creates vectors containing information of overall efficiency and power for varying values of mass and spring constant. It also creates three-dimensional matrices containing information of efficiency and power for varying points in the k-M plane.

```
clear all;
close all;

load dissertation;

%% efficiency and power vs. mass
if 0,
q=0;
eff=0;
    for M=0.01:0.1:1.91,
        q=q+1;
        b=sqrt(4*zeta^2*k*M);
        sim Simulation_Model_dissertation;
        crosstime=max(cross_time(:,2));
            for i=1:length(cross_time),
                if cross_time(i,2)==crosstime,
                    index=i; %% index is the (:,1) number corresponding
to time series
                end
            end
        eff(q)=Efficiency(index,2);
        pow(q)=Energy(index,2)/crosstime;
        mass(q)=M;
    end
end
%% efficiency and power vs. mass and diaphragm stiffness.
    % This algorithm runs the simulation for every combination of
values of
    % M and k (see intervals below) and creates two-dimensional arrays
eff(q,p)
    % and pow(q,p), and vectors mass(q) and spring(p), for p,q=1:1:20.

if 1,
q=0;
eff=0;
pow=0;
    for M=0.01:0.1:1.91,
        q=q+1;
        p=0;
        for k=10:100:1910,
           p=p+1;
           b=sqrt(4*zeta^2*k*M);
           sim Simulation_Model_dissertation;
           crosstime=max(cross_time(:,2));
           for i=1:length(cross_time),
               if cross_time(i,2)==crosstime,
                   index=i; %% index is the (:,1) number corresponding
to time series
               end
           end
```

```
           eff(q,p)=Efficiency(index,2);
           pow(q,p)=Energy(index,2)/crosstime;
           spring(p)=k;
           [q,p]
        end
        mass(q)=M;
    end
end

%% efficiency and power vs. pump dead volume
if 0,
q=0;
eff=0;
    for Vp_dead=0:0.25e-6:10e-6,
        q=q+1;
        sim Simulation_Model_dissertation;
        crosstime=max(cross_time(:,2));
            for i=1:length(cross_time),
                if cross_time(i,2)==crosstime,
                    index=i; %% index is the (:,1) number corresponding
to time series
                end
            end
        eff(q)=Efficiency(index,2);
        pow(q)=Energy(index,2)/crosstime;
        dead_volume(q)=Vp_dead;
    end
end
```

MATLAB m-file "simulated_parameter_variation_analysis_plots."

This m-file takes the data collected from "simulated_parameter_variation_analysis.m" and generates plots. (Figures 3-8 through 3-12).

```
close all
load eff_n_pow_vs_m_n_k
%% 3D plots: efficiency and power as function of mass and spring.

for i=1:1:length(eff),      %this switches the rows of eff and pow
since
    for j=1:1:length(eff),   %the mesh comand plots the inverse.
        temp_eff(i,j)=eff(j,i);
        temp_pow(i,j)=pow(j,i);
    end
end

figure(1);
mesh(mass,spring,temp_eff*100) %3D plot: mass(x), spring(y) and
efficiency(z)
xlabel('Mass (kg)');
ylabel('Spring Constant (N/m)');
zlabel('Overall System Efficiency (%)');

figure(2);
mesh(mass,spring,temp_pow) %3D plot: mass(x), spring(y) and power(z)
xlabel('Mass (kg)');
ylabel('Spring Constant (N/m)');
zlabel('Output Power (W)');

%% 2D plot: efficiency and power as function of mass with nominal
spring

figure(3);
plot(mass,eff(:,11)*100,'--b','LineWidth',2);
hold on;
plot(mass,pow(:,11)/100,'g','LineWidth',2);
grid;
xlabel('Mass (kg)');
legend('Efficiency (%)','Output Power (x100 W)');
title('Power and Efficiency for Varying Mass');

%% 2D plot: efficiency and power as function of spring with nominal
mass

figure(4);
plot(spring,eff(11,:)*100,'--b','LineWidth',2);
hold on;
plot(spring,pow(11,:)/100,'g','LineWidth',2);
grid;
axis([0 2000 0 4]);
xlabel('Spring Constant (N/m)');
legend('Overall Efficiency (%)','Output Power (x100 W)');
title('Power and Efficiency for Varying Spring Constant');
```

```
%% 2D plot: efficiency and power as function of pump dead volume with
nominal mass

load eff_n_pow_vs_Vpdead;
figure(5);
plot(dead_volume*1e6,eff2*100,'--b','LineWidth',2);
hold on;
plot(dead_volume*1e6,pow2/100,'g','LineWidth',2);
grid;
xlabel('Dead Volume in Pump Chamber (cc)');
legend('Efficiency (%)','Output Power (x100 W)');
title('Power and Efficiency for Varying Pump Dead Volume');
axis([0 10 0 4]);
```

MATLAB m-file "Energy_plots."

This m-file generates plots that show energy storage as a function of time. it produces Figure 3-13 from the document as well as two others with lower piston mass.

```
close all;
clear all;
load dissertation;

%% Pneumatic PE in combustion and expansion chamber
%PE_comb_exp=((P_combustion(:,2)).*(V_expansion(:,2)+Vc)/(1-
gamma_prod)).*((P_combustion(:,2)/P_atm).^((1-gamma_prod)/gamma_prod)-
1);

%PE in Combustion Chamber
PE_comb=((P_combustion(:,2)).*(Vc)/(1-
gamma_prod)).*((P_combustion(:,2)/P_atm).^((1-gamma_prod)/gamma_prod)-
1);

%PE in Expansion Chamber
PE_exp=((P_expansion(:,2)).*(V_expansion(:,2))/(1-
gamma_prod)).*((P_expansion(:,2)/P_atm).^((1-gamma_prod)/gamma_prod)-
1);

PE_comb_exp=PE_comb+PE_exp;

%% Kinetic energy of free piston
KE_fp=0.5*M*(V_expansion1(:,2)./A).^2;
%% Kinetic energy of combustion valve
KE_cv=0.5*m*(x_valve_dot(:,2)).^2;
%% Pneumatic PE in compression chamber
PE_comp=(P_pump(:,2)).*(V_pump(:,2))/(1-
gamma_air).*((P_pump(:,2)./P_atm).^((1-gamma_air)/gamma_air)-1);
%% Pneumatic potential put in reservior
%mass_pumped=mp0-P_pump1(:,2)-15.67/16.67*mc0; %removes investment for
next combustion
mass_res=mass_pumped;
index=0;
if 1,
    for j=1:1:length(pump_end_delay),
        if pump_end_delay(j,2)==max(pump_end_delay(:,2)),
            index=j;
            break;
        end
    end
end

if 1,
    for i=index:1:length(pump_end_delay);
        %mass_res(i,2)=mass_pumped(length(mass_pumped),2)-
15.67/16.67*mc0;
        mass_res(i,2)=0.0001;
    end
end
vf=mass_res(:,2)*R_air*T_amb/P_s; %partial volume pumped (with heat
losses)
```

```
PE_res=vf*P_s/(1-gamma_air)*((P_s/P_atm)^((1-gamma_air)/gamma_air)-1);

%PE_res(12300:length(V_expansion(:,1)))=PE_res(12300:length(V_expansion
(:,1)))+offset;
%% PE spring
PE_spring=0.5*k*((V_pump(:,2)-V0)/A).^2;
%% Plot all energies
figure(1)
plot(V_expansion(:,1)*1e3, PE_comb_exp,'b','LineWidth',2);
hold on
plot(V_expansion(:,1)*1e3, KE_fp,'r','LineWidth',2);
plot(V_expansion(:,1)*1e3, PE_comp,'g','LineWidth',2);
plot(V_expansion(:,1)*1e3, PE_res,'m','LineWidth',2);
plot(V_expansion(:,1)*1e3, KE_cv,'k','LineWidth',2);
plot(V_expansion(:,1)*1e3, PE_spring,'k:','LineWidth',2);
%plot(V_expansion(:,1)*1e3,
PE_comb_exp+KE_fp+KE_cv(:,2)+PE_comp+PE_res+PE_spring,'k:','LineWidth',
2);
axis([0 10 -5 65]); grid; hold off;
%legend('Pneumatic PE Combustion and Expansion Chambers','Kinetic
Energy of Free Piston','Kinetic Energy of Combustion Valve','Pneumatic
PE of Compression Chamber','Pneumatic PE in Reservoir (after heat
loss)','Total Stored Energy')
legend('Pneumatic PE Combustion and Expansion Chambers','Kinetic Energy
of Free Piston','Pneumatic PE of Compression Chamber','Pneumatic PE in
Reservoir (after heat loss)','Kinetic Energy of Combustion
Valve','Elastic PE of diaphragms')
xlabel('Time (msec)');
ylabel('Energy (J)');

%%
if 0,

clear all;
load dissertation_low_mass; %M=0.05 kg

%% Pneumatic PE in combustion and expansion chamber
%PE_comb_exp=((P_combustion(:,2)).*(V_expansion(:,2)+Vc)/(1-
gamma_prod)).*((P_combustion(:,2)/P_atm).^((1-gamma_prod)/gamma_prod)-
1);

%PE in Combustion Chamber
PE_comb=((P_combustion(:,2)).*(Vc)/(1-
gamma_prod)).*((P_combustion(:,2)/P_atm).^((1-gamma_prod)/gamma_prod)-
1);

%PE in Expansion Chamber
PE_exp=((P_expansion(:,2)).*(V_expansion(:,2))/(1-
gamma_prod)).*((P_expansion(:,2)/P_atm).^((1-gamma_prod)/gamma_prod)-
1);

PE_comb_exp=PE_comb+PE_exp;

%% Kinetic energy of free piston
KE_fp=0.5*M*(V_expansion1(:,2)./A).^2;
%% Kinetic energy of combustion valve
KE_cv=0.5*m*(x_valve_dot).^2;
```

```
%% Pneumatic PE in compression chamber
PE_comp=(P_pump(:,2)).*(V_pump(:,2))/(1-
gamma_air).*((P_pump(:,2)./P_atm).^((1-gamma_air)/gamma_air)-1);
%% Pneumatic potential put in reservior
%mass_pumped=mp0-P_pump1(:,2)-15.67/16.67*mc0; %removes investment for
next combustion
mass_res=mass_pumped;
index=0;
if 1,
    for j=1:1:length(pump_end_delay),
        if pump_end_delay(j,2)==max(pump_end_delay(:,2)),
            index=j;
            break;
        end
    end
end

if 1,
    for i=index:1:length(pump_end_delay);
        mass_res(i,2)=mass_pumped(length(mass_pumped),2)-
15.67/16.67*mc0;
        %mass_res(i,2)=0.0001;
    end
end
vf=mass_res(:,2)*R_air*T_amb/P_s; %partial volume pumped (with heat
losses)
PE_res=vf*P_s/(1-gamma_air)*((P_s/P_atm)^((1-gamma_air)/gamma_air)-1);

%PE_res(12300:length(V_expansion(:,1)))=PE_res(12300:length(V_expansion
(:,1)))+offset;
%% PE spring
PE_spring=0.5*k*((V_pump(:,2)-V0)/A).^2;
%% Plot all energies
Figure(2)
plot(V_expansion(:,1)*1e3, PE_comb_exp,'b','LineWidth',2);
hold on
plot(V_expansion(:,1)*1e3, KE_fp,'r','LineWidth',2);
plot(V_expansion(:,1)*1e3, PE_comp,'g','LineWidth',2);
plot(V_expansion(:,1)*1e3, PE_res,'m','LineWidth',2);
plot(V_expansion(:,1)*1e3, KE_cv,'k','LineWidth',2);
plot(V_expansion(:,1)*1e3, PE_spring,'c:','LineWidth',1);
plot(V_expansion(:,1)*1e3,
PE_comb_exp+KE_fp+KE_cv(:,2)+PE_comp+PE_res+PE_spring,'k:','LineWidth',
2);
axis([0 20 -5 65]);
%legend('Pneumatic PE Combustion and Expansion Chambers','Kinetic
Energy of Free Piston','Kinetic Energy of Combustion Valve','Pneumatic
PE of Compression Chamber','Pneumatic PE in Reservoir (after heat
loss)','Total Stored Energy')
legend('Pneumatic PE Combustion and Expansion Chambers','Kinetic Energy
of Free Piston','Pneumatic PE of Compression Chamber','Pneumatic PE in
Reservoir (after heat loss)','Kinetic Energy of Combustion
Valve','Elastic PE of diaphragms')
xlabel('Time (msec)');
ylabel('Energy (J)');

%%
```

```
clear all;
load dissertation_very_low_mass; %M=0.005 kg

%% Pneumatic PE in combustion and expansion chamber
%PE_comb_exp=((P_combustion(:,2)).*(V_expansion(:,2)+Vc)/(1-
gamma_prod)).*((P_combustion(:,2)/P_atm).^((1-gamma_prod)/gamma_prod)-
1);

%PE in Combustion Chamber
PE_comb=((P_combustion(:,2)).*(Vc)/(1-
gamma_prod)).*((P_combustion(:,2)/P_atm).^((1-gamma_prod)/gamma_prod)-
1);

%PE in Expansion Chamber
PE_exp=((P_expansion(:,2)).*(V_expansion(:,2))/(1-
gamma_prod)).*((P_expansion(:,2)/P_atm).^((1-gamma_prod)/gamma_prod)-
1);

PE_comb_exp=PE_comb+PE_exp;

%% Kinetic energy of free piston
KE_fp=0.5*M*(V_expansion1(:,2)./A).^2;
%% Kinetic energy of combustion valve
KE_cv=0.5*m*(x_valve_dot).^2;
%% Pneumatic PE in compression chamber
PE_comp=(P_pump(:,2)).*(V_pump(:,2))/(1-
gamma_air).*((P_pump(:,2)./P_atm).^((1-gamma_air)/gamma_air)-1);
%% Pneumatic potential put in reservior
%mass_pumped=mp0-P_pump1(:,2)-15.67/16.67*mc0; %removes investment for
next combustion
mass_res=mass_pumped;
index=0;
if 1,
    for j=1:1:length(pump_end_delay),
        if pump_end_delay(j,2)==max(pump_end_delay(:,2)),
            index=j;
            break;
        end
    end
end

if 1,
    for i=index:1:length(pump_end_delay);
        mass_res(i,2)=mass_pumped(length(mass_pumped),2)-
15.67/16.67*mc0;
        %mass_res(i,2)=0.0001;
    end
end
vf=mass_res(:,2)*R_air*T_amb/P_s; %partial volume pumped (with heat
losses)
PE_res=vf*P_s/(1-gamma_air)*((P_s/P_atm)^((1-gamma_air)/gamma_air)-1);

%PE_res(12300:length(V_expansion(:,1)))=PE_res(12300:length(V_expansion
(:,1)))+offset;
%% PE spring
PE_spring=0.5*k*((V_pump(:,2)-V0)/A).^2;
```

```
%% Plot all energies
figure(3)
plot(V_expansion(:,1)*1e3, PE_comb_exp,'b','LineWidth',2);
hold on
plot(V_expansion(:,1)*1e3, KE_fp,'r','LineWidth',2);
plot(V_expansion(:,1)*1e3, PE_comp,'g','LineWidth',2);
plot(V_expansion(:,1)*1e3, PE_res,'m','LineWidth',2);
plot(V_expansion(:,1)*1e3, KE_cv,'k','LineWidth',2);
plot(V_expansion(:,1)*1e3, PE_spring,'c:','LineWidth',1);
plot(V_expansion(:,1)*1e3,
PE_comb_exp+KE_fp+KE_cv(:,2)+PE_comp+PE_res+PE_spring,'k:','LineWidth',
2);
axis([0 20 -5 65]);
%legend('Pneumatic PE Combustion and Expansion Chambers','Kinetic
Energy of Free Piston','Kinetic Energy of Combustion Valve','Pneumatic
PE of Compression Chamber','Pneumatic PE in Reservoir (after heat
loss)','Total Stored Energy')
legend('Pneumatic PE Combustion and Expansion Chambers','Kinetic Energy
of Free Piston','Pneumatic PE of Compression Chamber','Pneumatic PE in
Reservoir (after heat loss)','Kinetic Energy of Combustion
Valve','Elastic PE of diaphrams')
xlabel('Time (msec)');
ylabel('Energy (J)');

end;
```

MATLAB m-file "Combustion_Valve_Model_Validation_Plots.m"

This m-file generates combustion valve validation plots shown in Figures 5-2 through 5-7.

```
clear all;
close all;

%load experimental data
%load valve_laser_data_040208_40psi_res_good;
%load valve_laser_data_040208_46psi_res_good;
%load valve_laser_data_040208_60psi_res_good;
load valve_laser_data_040208_80psi_res_good;

Pc_exp = P_comb1;
sigs=signals;
x_valve_exp = valve_disp;

if 1,

%% Plot typical experimental combustion at 80 psig air supply

figure(1)
plot(Pc_exp(:,1)-0.672,(Pc_exp(:,2)+18.2)*6.895,'g','LineWidth',2);
grid;
axis([-0.04 0.02 0 1500]);
xlabel('Time (s)'); ylabel('Pressure in Combustion Chamber (kPa)');

%% Plot same experimental combustion with modeled

figure(2)
plot(Pc_exp(:,1)-1.172,(Pc_exp(:,2)+17.7)*6.895,'g','LineWidth',2);
grid;
hold on;
load combustion_validation_simulation_80psi;
Pc_sim = P_combustion;
plot((Pc_sim(:,1))-0.0355,(Pc_sim(:,2)+0.19)*6.895,'b-
.','LineWidth',2);
legend('Combustion Pressure (Experimental)','Combustion Pressure
(Simulation)');
xlabel('Time (s)'); ylabel('Pressure in Combustion Chamber (kPa)');


axis([-0.04 0.02 0 1500]);
%xlabel('Time (s)'); ylabel('Pressure in Combustion Chamber (kPa)');


%%
%load simulation data
%load combustion_validation_simulation_40psi;
%load combustion_validation_simulation_46psi;
%load combustion_validation_simulation_60psi;
%load combustion_validation_simulation_80psi;
%Pc_sim = P_combustion;
```

```
x_valve_sim = x_valve;

figure(3)
hold on;
%%

plot((Pc_sim(:,1))-0.0354,(Pc_sim(:,2))*6.895,'b-.','LineWidth',2);
plot(Pc_exp(:,1)-1.1366-
0.0354,(Pc_exp(:,2)+15.7)*6.895,'g','LineWidth',2);
plot(x_valve_sim(:,1)-
0.0354,10000*x_valve_sim(:,2)*10,'k:','LineWidth',2);
plot(x_valve_exp(:,1)-1.236-
0.0354,(x_valve_exp(:,2)+1.38)*100,'r','LineWidth',2);
grid;
xlabel('Time (s)');
ylabel('Pressure (kPa), Displacement (1000=10mm)');
legend('Combustion Pressure (Simulation)','Combustion Pressure
(Experimental)',...
    'Valve Displacement (Simulation)','Valve Displacement
(Experimental)',...
    'Location','NorthWest');
axis([-0.036 0.03 0 1500]);

%%
load valve_laser_data_040208_60psi_res_good;
Pc_exp = P_comb1;
x_valve_exp = valve_disp;
load combustion_validation_simulation_60psi;
Pc_sim = P_combustion;
x_valve_sim = x_valve;

figure(4)
hold on;
plot((Pc_sim(:,1))-0.036,(Pc_sim(:,2))*6.895,'b-.','LineWidth',2);
plot(Pc_exp(:,1)-1.636-
0.036,(Pc_exp(:,2)+14.7)*6.895,'g','LineWidth',2);
plot(x_valve_sim(:,1)-
0.036,10000*x_valve_sim(:,2)*10,'k:','LineWidth',2);
plot(x_valve_exp(:,1)-1.636-
0.036,(x_valve_exp(:,2)+8.38)*100,'r','LineWidth',2);
xlabel('Time (s)');
ylabel('Pressure (kPa), Displacement (1000=10mm)');
legend('Combustion Pressure (Simulation)','Combustion Pressure
(Experimental)',...
    'Valve Displacement (Simulation)','Valve Displacement
(Experimental)',...
    'Location','NorthWest');
axis([-0.036 0.03 0 1500]);
grid;

%%
load valve_laser_data_040208_46psi_res_good;
Pc_exp = P_comb1;
x_valve_exp = valve_disp;
load combustion_validation_simulation_46psi;
Pc_sim = P_combustion;
x_valve_sim = x_valve;
```

```
figure(5)
hold on;
plot((Pc_sim(:,1))-0.035,(Pc_sim(:,2))*6.895,'b-.','LineWidth',2);
plot(Pc_exp(:,1)-1.737-
0.035,(Pc_exp(:,2)+14.7)*6.895,'g','LineWidth',2);
plot(x_valve_sim(:,1)-
0.035,10000*x_valve_sim(:,2)*10,'k:','LineWidth',2);
plot(x_valve_exp(:,1)-1.737-
0.035,(x_valve_exp(:,2)+2.942)*100,'r','LineWidth',2);
grid;
xlabel('Time (s)');
ylabel('Pressure (kPa), Displacement (1000=10mm)');
legend('Combustion Pressure (Simulation)','Combustion Pressure
(Experimental)',...
    'Valve Displacement (Simulation)','Valve Displacement
(Experimental)',...
    'Location','NorthWest');
axis([-0.036 0.03 0 1500]);

end
%% plot combutsion pressure and its derivative next to valve
displacement,
% for 80 psig supply.
% this will be used to show that when valve lets go, pressure is still
% building up in chamber.

clear all;
load combustion_validation_simulation_80psi;
load derivatives;

figure(6)
subplot(4,1,1), plot(x_valve(:,1)*1000-35.4,1000*x_valve(:,2));
grid; axis([2.6 6.6 0 0.5]); title('Valve Displacement');
xlabel('Time (ms)'); ylabel('mm');
subplot(4,1,2), plot(P_combustion(:,1)*1000-
35.4,P_combustion(:,2)*6.895);
grid; axis([2.6 6.6 0 1500]); title('Combustion Pressure');
xlabel('Time (ms)'); ylabel('kPa');
subplot(4,1,3), plot(P_combustion_80_dot(:,1)*1000-
35.4,P_combustion_80_dot(:,2)*6.895);
grid; axis([2.6 6.6 -2000000 1000000]); title('First Derivative of
Combustion Pressure');
xlabel('Time (ms)'); ylabel('kPa/s');
subplot(4,1,4), plot(P_combustion_80_ddot(:,1)*1000-
35.4,P_combustion_80_ddot(:,2)*6.895);
grid; axis([2.6 6.6 0 600000000]); title('Second Derivative of
Combustion Pressure');
xlabel('Time (ms)'); ylabel('kPa/s/s');
```

MATLAB m-file "Continuous_Combustion_Plots.m"

This m-file generates experimental plots of open combustion at 1, 5 and 10 Hz. These are Figures 5-9 through 5-11 from the document.

```
%% This plots open combustion data for continuous combustion at 1, 5,
and
% 10 Hz

%% 1 Hz
clear all; close all;

load 070608_Open_Combustion_1Hz.mat

figure(1)
plot(P_comb1(:,1),(P_comb1(:,2)+9.7)*6.895,'LineWidth',2); grid;
xlabel('Time (s)'); ylabel('Combustion Pressure (kPa)');
axis([0 10 0 2000]);

%% 5 Hz
clear all;

load 070608_Open_Combustion_5Hz.mat

figure(2)
plot(P_comb1(:,1),(P_comb1(:,2)+14.7)*6.895,'LineWidth',2); grid;
xlabel('Time (s)'); ylabel('Combustion Pressure (kPa)');
axis([0 5 0 2000]);

%% 10 Hz
clear all;

load 070608_Open_Combustion_10Hz.mat

figure(3)
plot(P_comb1(:,1),(P_comb1(:,2)+14.7)*6.895,'LineWidth',2); grid;
xlabel('Time (s)'); ylabel('Combustion Pressure (kPa)');
axis([0 3 0 2000]);
```

MATLAB m-file "Open_Loop_Experimental_and_Model_Validation_Plots.m"

This m-file generates experimental plots of "open loop" FLPC operation and compares it against the model. It produces Figures 5-13 through 5-19 from the document.

```
close all;
clear all;

load 051508_full_device_r13

%% Filter Reservoir Pressure Signal, with 200 Hz. cutoff

cutoff=200; %cutoff frequency, in Hz
w_n=2*pi*cutoff; %cutoff in radians
num1=[1];
den1=[1/w_n 1];
sys1=tf(num1,den1); %First order Filter

sys1dis=c2d(sys1,0.0002) %Convert to discrete

%Create vectors B and A, with first coefficient corresponding to the
%highest order of z in denominator.  Once you do, run:

%P_res_filt=filtfilt(B,A,P_ecr(:,4));

%For a 1st order filter with cutoff of 200 Hz, use command lines below:

B=[0 0.2222];
A=[1 -0.7778];
P_res_filt=filtfilt(B,A,P_ecr(:,4));

%% Plot 7 consecutive pumpings with all signals (filtered res.
pressure)

figure(1);
plot(P_comb(:,1)-1.95,(P_comb(:,2)+18.7)*6.895,P_ecr(:,1)-
1.95,(P_ecr(:,2)+16.7)*6.895,P_ecr(:,1)-
1.95,(P_ecr(:,3)+14.7)*6.895,P_ecr(:,1)-
1.95,(P_res_filt+14.7)*6.895,'LineWidth',1);
grid;
axis([0 0.95 0 1400]);
xlabel('Time (s)');
ylabel('Pressure (kPa)');
legend('Combustion Pressure','Expansion Pressure','Pump
Pressure','Reservoir Pressure')
%title('Pressures in Combustion Chamber (red), Expansion Chamber
(blue), Pump Chamber (green) and Reservoir (Turquoise)')

%% Plot zoomed-in reservoir pressure for same data

figure(2);
plot(P_ecr(:,1)-1.95,(P_res_filt+14.7)*6.895,'c');
grid;
axis([0 0.95 467 577]);
xlabel('Time (s)');
ylabel('Pressure (kPa)');
```

```
%% Plot experimental single event, all signals.

figure(3);
plot(P_comb(:,1)-2.523,(P_comb(:,2)+18.7)*6.895,'b','LineWidth',2);
hold on;
plot(P_ecr(:,1)-2.523,(P_ecr(:,2)+16.7-0.05)*6.895,'g','LineWidth',2);
plot(P_ecr(:,1)-2.523,(P_ecr(:,3)+14.7-2)*6.895,'r','LineWidth',2);
plot(P_ecr(:,1)-2.523,(P_res_filt+14.7)*6.895,'c','LineWidth',2);
hold off;
grid;
axis([-0.028 0.03 0 1400]);
xlabel('Time (s)');
ylabel('Pressure (kPa)');
legend('Combustion Pressure','Expansion Pressure','Pump
Pressure','Reservoir Pressure','Location','NorthWest')

%% Plot Command Signals

figure(4);
plot(signals(:,1)-2.523,(signals(:,2)-0.05)*3,'r','LineWidth',2); hold
on;
plot(signals(:,1)-2.523,(signals(:,4)-0.15)*0.5,'b','LineWidth',2);
%plot(signals(:,1)-2.523,signals(:,5),'g','LineWidth',2);
plot(signals(:,1)-2.523,signals(:,6),'g','LineWidth',2);
hold off;
grid;
axis([-0.028 0.03 -0.1 11]);
xlabel('Time (s)');
ylabel('Current (Amperes)');
legend('Ignition Coil','Injection On/Off Valve','Exhaust
Solenoid','Location','NorthWest');

%% Plot Simulated single event

load 073108_Dissertation_Full_Model_2_cycles_3.mat;
figure(5);
plot(P_combustion(:,1)-
0.0286,P_combustion(:,2)*6.895,'b','LineWidth',2); hold on;
plot(P_expansion(:,1)-0.0286,P_expansion(:,2)*6.895,'g','LineWidth',2);
plot(P_pump(:,1)-0.0286,P_pump(:,2)*6.895,'r','LineWidth',2);
plot(P_res(:,1)-0.0286,P_res(:,2)*6.895,'c','LineWidth',2);
hold off;
grid;
axis([-0.029 0.03 0 1400]);
xlabel('Time (s)');
ylabel('Pressure (kPa)');
legend('Combustion Pressure','Expansion Pressure','Pump
Pressure','Reservoir Pressure','Location','NorthWest');
axis([-0.028 0.03 0 1400]);

%% Plot simulated and Experimental Combustion Pressures

figure(6);
plot(P_comb(:,1)-2.523,(P_comb(:,2)+18.7)*6.895,'b','LineWidth',2);
hold on;
```

```
plot(P_combustion(:,1)-0.0286,P_combustion(:,2)*6.895,'g-
.','LineWidth',2);
hold off;
grid;
axis([-0.028 0.03 0 1400]);
xlabel('Time (s)');
ylabel('Pressure (kPa)');
legend('Experimental','Simulated','Location','NorthWest');

%% Plot simulated and Experimental Expansion Pressures

figure(7);
plot(P_ecr(:,1)-2.523,(P_ecr(:,2)+16.7-0.05)*6.895,'b','LineWidth',2);
hold on;
plot(P_expansion(:,1)-0.0286,P_expansion(:,2)*6.895,'g-
.','LineWidth',2);
hold off;
grid;
axis([0 0.03 0 500]);
xlabel('Time (s)');
ylabel('Pressure (kPa)');
legend('Experimental','Simulated','Location','NorthWest');

%% Plot simulated and Experimental Pump and Reservoir Pressures

figure(8);
plot(P_ecr(:,1)-2.523,(P_ecr(:,3)+14.7-2)*6.895,'b','LineWidth',2);
hold on;
plot(P_pump(:,1)-0.0286,P_pump(:,2)*6.895,'g-.','LineWidth',2);
plot(P_ecr(:,1)-2.523,(P_res_filt+14.7)*6.895,'c','LineWidth',2); hold
on;
plot(P_res(:,1)-0.0286,P_res(:,2)*6.895,'r-.','LineWidth',2);
hold off;
grid;
axis([0 0.03 0 650]);
xlabel('Time (s)');
ylabel('Pressure (kPa)');
legend('Experimental Pump Pressure','SimulatedPump
Pressure','Experimental Reservoir Pressure','Simulated reservoir
Pressure','Location','NorthEast');
```

MATLAB m-file "Closed_Loop_Experimental_Plots.m"

This m-file generates experimental plots of "closed loop" FLPC operation. It corresponds to Figures 5-20 and 5-21 from the document.

```
clear all;
close all;

load
070608_Full_Device_From_res_then_wall_convex_diaph_vs_wavy_diaph_4Hz_th
ree_good_pumps_04.mat;

%% Patch data from spark noise in reservoir signal.

for i=1:length(P_ecr(:,1)),
    if P_ecr(i,1)>7.7204,
        if P_ecr(i,1)<7.7208,
            P_ecr(i,4)=66.6185;
        end
    end
end

%% Filter Reservoir Pressure Signal, with 200 Hz. cutoff

cutoff=200; %cutoff frequency, in Hz
w_n=2*pi*cutoff; %cutoff in radians
num1=[1];
den1=[1/w_n 1];
sys1=tf(num1,den1); %First order Filter

sys1dis=c2d(sys1,0.0002) %Convert to discrete

%Create vectors B and A, with first coefficient corresponding to the
%highest order of z in denominator.  Once you do, run:

%P_res_filt=filtfilt(B,A,P_ecr(:,4));

%For a 1st order filter with cutoff of 200 Hz, use command lines below:

B=[0 0.2222];
A=[1 -0.7778];
P_res_filt=filtfilt(B,A,P_ecr(:,4));

%% plot all signals for good pumping event

figure(1);
plot(P_comb(:,1)-7.7206,(P_comb(:,2)+14.7)*6.895,'b','LineWidth',2);
hold on;
plot(P_ecr(:,1)-7.7206,(P_ecr(:,2)+14.7)*6.895+3,'g','LineWidth',2);
plot(P_ecr(:,1)-7.7206,(P_ecr(:,3)+14.7)*6.895-40,'r','LineWidth',2);
plot(P_ecr(:,1)-7.7206,(P_res_filt+14.7)*6.895,'c','LineWidth',2);
hold off;
grid;
axis([-0.041 0.059 0 1300]); % good pump not after misfire
```

```
xlabel('Time (s)');
ylabel('Pressure (kPa)');
legend('Combustion Chamber','Expansion Chamber','Pump
Chamber','Reservoir');

%% Plot zoomed-in reservoir signal

figure(2);
plot(P_ecr(:,1)-7.7206,(P_res_filt+14.7)*6.895,'c','LineWidth',2);
grid;
axis([-0.041 0.059 550 590]);
xlabel('Time (s)');
ylabel('Pressure (kPa)');
```

MATLAB m-file "Closed_Loop_Analysis_Plots.m"

This m-file generates experimental plots for misfire analysis. It produces Figures 6-1 through 6-3 in the document.

```
close all;
clear all;

load 071508_full_device_from_res_30ms_inj_40msexhsol_8Hz_06.mat;
figure(1);
plot(P_comb(:,1)-2,(P_comb(:,2)+21.7)*6.895,P_ecr(:,1)-
2,(P_ecr(:,4)+14.7)*6.895);
grid;
axis([-0.03 4 0 1200]);
xlabel('Time (s)');
ylabel('Pressure (kPa)');
legend('Combustion Chamber','Reservoir');


%% Side by side comparison of data after misfire and after regular fire

load
070408_Full_Device_From_wall_then_res_convex_diaphragm_with_water_two_p
umps_01.mat;

% Patch data from spark noise in signals.

for i=1:length(P_ecr(:,1)),
    if P_ecr(i,1)>6.152,
        if P_ecr(i,1)<6.1524,
            P_ecr(i,4)=60.075;
        end
    end
end

for i=1:length(P_ecr(:,1)),
    if P_ecr(i,1)>5.652,
        if P_ecr(i,1)<5.6524,
            P_ecr(i,4)=64.15;
        end
    end
end

for i=1:length(P_ecr(:,1)),
    if P_ecr(i,1)>6.152,
        if P_ecr(i,1)<6.1524,
            P_ecr(i,2)=2.5;
        end
    end
end

for i=1:length(P_ecr(:,1)),
    if P_ecr(i,1)>5.652,
        if P_ecr(i,1)<5.6524,
```

```
            P_ecr(i,2)=6.2;
        end
    end
end

for i=1:length(P_ecr(:,1)),
    if P_ecr(i,1)>6.152,
        if P_ecr(i,1)<6.1524,
            P_ecr(i,3)=2.5;
        end
    end
end

for i=1:length(P_ecr(:,1)),
    if P_ecr(i,1)>5.652,
        if P_ecr(i,1)<5.6524,
            P_ecr(i,3)=6.2;
        end
    end
end


% Filter Reservoir Pressure Signal, with 200 Hz. cutoff

cutoff=200; %cutoff frequency, in Hz
w_n=2*pi*cutoff; %cutoff in radians
num1=[1];
den1=[1/w_n 1];
sys1=tf(num1,den1); %First order Filter

sys1dis=c2d(sys1,0.0002) %Convert to discrete

%Create vectors B and A, with first coefficient corresponding to the
%highest order of z in denominator.  Once you do, run:

%P_res_filt=filtfilt(B,A,P_ecr(:,4));

%For a 1st order filter with cutoff of 200 Hz, use command lines below:

B=[0 0.2222];
A=[1 -0.7778];
P_res_filt=filtfilt(B,A,P_ecr(:,4));

% plot signals

figure(2);
plot(P_comb(:,1)-6.1522,(P_comb(:,2)+14.7)*6.895,P_ecr(:,1)-
6.1522,(P_ecr(:,2)+11.95)*6.895,...
    P_ecr(:,1)-6.1522,(P_ecr(:,3)+8.45)*6.895,P_ecr(:,1)-
6.1522,P_res_filt*6.3895);
hold on
plot(P_comb(:,1)-5.6522,(P_comb(:,2)+20.7)*6.895,':',P_ecr(:,1)-
5.6522,(P_ecr(:,2)+11.95)*6.895,':',...
    P_ecr(:,1)-5.6522,(P_ecr(:,3)+8.45)*6.895,':',P_ecr(:,1)-
5.6522,P_res_filt*6.895,':');
hold off;
grid;
```

```
xlabel('Time (s)');
ylabel('Pressure (kPa)');
axis([-0.0272 0.0328 0 1500]);
legend('Combustion Chamber 1','Expansion Chamber 1','Pump Chamber
1','Reservoir 1',...
    'Combustion Chamber 2','Expansion Chamber 2','Pump Chamber
2','Reservoir 2');

figure(3);
plot(P_comb(:,1)-6.1522,(P_comb(:,2)+14.7)*6.895,P_ecr(:,1)-
6.1522,(P_ecr(:,2)+11.95)*6.895,...
    P_ecr(:,1)-6.1522,(P_ecr(:,3)+8.45)*6.895,P_ecr(:,1)-
6.1522,P_res_filt*6.3895);
hold on
plot(P_comb(:,1)-5.6522,(P_comb(:,2)+20.7)*6.895,':',P_ecr(:,1)-
5.6522,(P_ecr(:,2)+11.95)*6.895,':',...
    P_ecr(:,1)-5.6522,(P_ecr(:,3)+8.45)*6.895,':',P_ecr(:,1)-
5.6522,P_res_filt*6.895,':');
hold off;
grid;
xlabel('Time (s)');
ylabel('Pressure (kPa)');
axis([0.005 0.02 0 700]);
legend('Combustion Chamber 1','Expansion Chamber 1','Pump Chamber
1','Reservoir 1',...
    'Combustion Chamber 2','Expansion Chamber 2','Pump Chamber
2','Reservoir 2');
```

MATLAB m-file "Simulation_Diagnosis_plots"

This m-file generates simulated and experimentally obtained plots used for diagnostics concerning initial piston position, leakage in combustion chamber, magnetic holding force and pressure port blockage. It generates Figures 6-4 through 6-12, and 6-15 from the document.

```
close all; clear all;

load 080508_Simulation_Closed_Loop_Nominal_01;

figure(1);
plot(P_all(:,1),P_all(:,2)*6.895,'b','LineWidth',2); hold on;
plot(P_all(:,1),P_all(:,3)*6.895,'g','LineWidth',2);
plot(P_all(:,1),P_all(:,4)*6.895,'r','LineWidth',2);
plot(P_all(:,1),P_all(:,5)*6.895,'c','LineWidth',2); hold off;
grid; axis([0 0.1 0 1700]); xlabel('Time (s)'); ylabel('Pressure
(kPa)');
legend('Combustion Chamber','Expansion Chamber','Pump
Chamber','Reservoir');

figure(2);
plot(V_expansion(:,1),V_expansion(:,2)*1000000,'LineWidth',2);
grid; axis([0 0.1 0 160]); xlabel('Time (s)'); ylabel('Volume (mL)');

clear all; load leak_test_optrand.mat; figure(3); subplot(2,1,1);
plot(P_comb(:,1)-4,(P_comb(:,2)+10.7)*6.895,'LineWidth',2); grid;
axis([0 4.5 0 800]); xlabel('Time (s)'); ylabel('Pressure (kPa)');
title('(a) Pressure in Combustion Chamber');
subplot(2,1,2);
plot(signals(:,1),signals(:,5),signals(:,1),signals(:,6),'LineWidth',2)
; grid
axis([0 4.5 -0.1 1.75]); xlabel('Time (s)'); ylabel('Signal (1=on;
0=off)');
title('(b) Injection and Exhaust Valve Command Signals');
legend('Injection','Exhaust');

clear all; load 080508_Simulation_Closed_Loop_Nominal_01; figure(4);
plot(P_all(:,1),P_all(:,2)*6.895,'b','LineWidth',2); hold on;
plot(P_all(:,1),P_all(:,3)*6.895,'g','LineWidth',2);
plot(P_all(:,1),P_all(:,4)*6.895,'r','LineWidth',2);
plot(P_all(:,1),P_all(:,5)*6.895,'c','LineWidth',2); hold off;
grid; %axis([0.045 0.095 0 1700]); xlabel('Time (s)'); ylabel('Pressure
(kPa)');
legend('Combustion Chamber','Expansion Chamber','Pump
Chamber','Reservoir');

clear all; load 080508_Simulation_Closed_Loop_Cmag_00008_03
E0=337.6550; %Initial Pneumatic PE in reservoir - computed from initial
conditions
figure(5);
plot(P_all(:,1),P_all(:,2)*6.895,'b','LineWidth',2); hold on;
plot(P_all(:,1),P_all(:,3)*6.895,'g','LineWidth',2);
plot(P_all(:,1),P_all(:,4)*6.895,'r','LineWidth',2);
```

```
plot(P_all(:,1),P_all(:,5)*6.895,'c','LineWidth',2); hold off;
grid; axis([0 0.1 0 1500]); xlabel('Time (s)'); ylabel('Pressure
(kPa)');
legend('Combustion','Expansion','Pump','Reservoir');

figure(6);
plot(Energy(:,1),E0+Energy(:,2),'LineWidth',2); grid;
%plot(m_pump(:,1),0.0042+mass_pumped(:,2)-m_reinv(:,2),'LineWidth',2);
axis([0 0.1 332 347]); xlabel('Time (s)'); ylabel('Pneumatic Potential
Energy (J)');

clear all; load 080508_Simulation_Closed_Loop_Cmag_0012_02;
E0=337.6550; figure(7);
plot(P_all(:,1),P_all(:,2)*6.895,'b','LineWidth',2); hold on;
plot(P_all(:,1),P_all(:,3)*6.895,'g','LineWidth',2);
plot(P_all(:,1),P_all(:,4)*6.895,'r','LineWidth',2);
plot(P_all(:,1),P_all(:,5)*6.895,'c','LineWidth',2); hold off;
grid; axis([0 0.1 0 1900]); xlabel('Time (s)'); ylabel('Pressure
(kPa)');
legend('Combustion','Expansion','Pump','Reservoir');

figure(8);
plot(Energy(:,1),E0+Energy(:,2),'LineWidth',2); grid;
%plot(m_pump(:,1),0.0042+mass_pumped(:,2)-m_reinv(:,2),'LineWidth',2);
axis([0 0.1 332 347]); xlabel('Time (s)'); ylabel('Pneumatic Potential
Energy (J)');


clear all; load 080508_Simulation_Closed_Loop_Cmag_00014_03;
E0=337.6550; figure(9);
plot(P_all(:,1),P_all(:,2)*6.895,'b','LineWidth',2); hold on;
plot(P_all(:,1),P_all(:,3)*6.895,'g','LineWidth',2);
plot(P_all(:,1),P_all(:,4)*6.895,'r','LineWidth',2);
plot(P_all(:,1),P_all(:,5)*6.895,'c','LineWidth',2); hold off;
grid; axis([0 0.1 0 2000]); xlabel('Time (s)'); ylabel('Pressure
(kPa)');
legend('Combustion','Expansion','Pump','Reservoir');

figure(10);
plot(Energy(:,1),E0+Energy(:,2),'LineWidth',2); grid
%lot(m_pump(:,1),0.0042+mass_pumped(:,2)-m_reinv(:,2),'LineWidth',2);
axis([0 0.1 332 347]); xlabel('Time (s)'); ylabel('Pneumatic Potential
Energy (J)');

clear all;
load
071608_full_device_from_res_30ms_inj_8Hz_convex_toward_comb_04.mat;
% Filter Reservoir Pressure Signal, with 200 Hz. cutoff
cutoff=200; %cutoff frequency, in Hz
w_n=2*pi*cutoff; %cutoff in radians
num1=[1];
den1=[1/w_n 1];
sys1=tf(num1,den1); %First order Filter
sys1dis=c2d(sys1,0.0002) %Convert to discrete
%Create vectors B and A, with first coefficient corresponding to the
%highest order of z in denominator.  Once you do, run:
%P_res_filt=filtfilt(B,A,P_ecr(:,4));
```

```
%For a 1st order filter with cutoff of 200 Hz, use command lines below:
B=[0 0.2222];
A=[1 -0.7778];
for i=5139:5142,
    P_ecr(i,4)=69.5;
end
P_res_filt=filtfilt(B,A,P_ecr(:,4));
figure(11);
plot(P_comb(5000:5250,1),(P_comb(5000:5250,2)+14.7)*6.895,'b','LineWidt
h',2); hold on;
plot(P_ecr(5000:5250,1),(P_ecr(5000:5250,2)+14.55)*6.895,'g','LineWidth
',2);
plot(P_ecr(5000:5250,1),(P_ecr(5000:5250,3)+13.34)*6.895,'r','LineWidth
',2);
plot(P_ecr(5000:5250,1),P_res_filt(5000:5250)*6.895,'c','LineWidth',2);
hold off; grid; axis([1 1.05 0 1350]); xlabel('Time (s)');
ylabel('Pressure (kPa)');
legend('Combustion','Expansion','Pump','Reservoir');
```

REFERENCES

[1] Dunn-Rankin, D., Leal, E. M., and Walther, D. C., (2005) "Personal Power Systems". *Progress in Energy and Combusion Scence,* vol. 31, pp. 422–465.

[2] Hirai, K., Hirose, M., Haikawa, Y., and Takenaka, T., (1998) "The Development of Honda Humanoid Robot," *Proceedings of the 1998 IEEE International Conference on Robotics & Automation (ICRA),* Leuven, Belgium, pp. 1321-1326.

[3] Van den Bosche, P., Vergels, F., Van Mierlo, J., Matheys, J., and Van Autenboer, W., (2006) "SUBAT: An Assessment of Sustainable Battery Technology," *Journal of Power Sources,* vol. 162, pp. 913-919.

[4] Kuribayashi, K., (1993) "Criteria for the evaluation of new actuators as energy converters," *Advanced Robotics*, vol. 7, no. 4, pp. 289-37.

[5] Goldfarb, M., Barth, E. J., Gogola, M. A., and Wehrmeyer, J. A., (2003) “Design and Energetic Characterization of a Liquid-Propellant-Powered Actuator for Self-Powered Robots,” *IEEE/ASME Transactions on Mechatronics*, vol. 8, no. 2, pp. 254-262.

[6] Fite, K. B., and Goldfarb, M., (2006) "Design and Energetic Characterization of a Proportional-Injector Monopropellant-Powered Actuator," *IEEE/ASME Transactions on Mechatronics,* vol. 11, no.2, pp. 196-204.

[7] Johansen, T. A., Egeland, O., Johannessen, E. A., and Kvamsdal, R., (2003) "Dynamics and Control of a Free-Piston Diesel Engine," *ASME Journal of Dynamic Systems, Measurement, and Control*, Vol. 125, pp. 468-474.

[8] Mikalsen, R., and Roskilly, A. P., (2007) "A Review of Free-Piston Engine History and Applications," *Applied Thermal Engineering,* vol. 27, pp. 2339-2352.

[9] Pescara, R. P., (1928) “Motor Compressor Apparatus,” U.S. Patent No. 1,657,641.

[10] Nakahara, M., (2001) "Free Piston Kikai-Kouzou to Rekisi". *Shinko-Techno Gihou*, Vol.13, No. 25 & 26.

[11] Klotsch, P., (1959) “Ford Free-Piston Engine Development,” *SAE Technical Paper Series*, 590045, vol. 67, pp. 373-378.

[12] Underwood, A. F., (1957) “The GMR 4-4 ‘Hyprex’ Engine: A Concept of the Free-Piston Engine for Automotive Use,” *SAE Technical Paper Series*, 570032, vol. 65, pp. 377-391.

[13] Aichlmayr, H. T., Kittelson, D. B., and Zachariah, M. R., (2002a) "Miniature free-piston homogenous charge compression ignition engine-compressor concept – Part I: performance estimation and design considerations unique to small dimensions," *Chemical Engineering Science*, 57, pp. 4161-4171.

[14] Aichlmayr, H. T., Kittelson, D. B., and Zachariah, M. R., (2002b) "Miniature free-piston homogenous charge compression ignition engine-compressor concept – Part II: modeling HCCI combustion in small scales with detailed homogeneous gas phase chemical kinetics," *Chemical Engineering Science*, 57, pp. 4173-4186.

[15] Aichlmayr, H. T., Kittelson, D. B., and Zachariah, M. R., (2003) "Micro-HCCI combustion: experimental characterization and development of a detailed chemical kinetic model with coupled piston motion," *Combustion and Flame*, 135, pp. 227-248.

[16] Beachley, N. H. and Fronczak, F. J., (1992) "Design of a Free-Piston Engine-Pump," *SAE Technical Paper Series*, 921740, pp. 1-8.

[17] McGee, T. G., Raade, J. W., and Kazerooni, H., (2004) "Monopropellant-Driven Free-piston Hydraulic Pump for Mobile Robotic Systems," *ASME Journal of Dynamic Systems, Measurement, and Control*, vol. 126, pp. 75-81.

[18] Achten, P. A.., Van Den Oeven, J. P. J., Potma, J., and Vael, G. E. M. (2000) Horsepower with Brains: the design of the CHIRON free piston engine, *SAE Technical Paper* 012545.

[19] Riofrio, J. A., and Barth, E. J., (2007) "A Free Piston Compressor as a Pneumatic Mobile Robot Power Supply: Design, Characterization and Experimental Operation," *International Journal of Fluid Power,* vol. 8, no. 1, pp 17-28.

[20] Barth, E. J., and Riofrio, J., (2004) "Dynamic Characteristics of a Free Piston Compressor," *2004 ASME International Mechanical Engineering Congress and Exposition (IMECE),* IMECE2004-59594, Anaheim, CA.

[21] Lide, David R. (ed), (2003) *CRC Handbook of Chemistry and Physics, 84th Edition*. CRC Press. Boca Raton, Florida.

[22] Richer, E., and Hurmuzlu, Y., (2000) "A High Performance Pneumatic Force Actuator System: Part I – Nonlinear Mathematical Model," *Transactions of ASME,* vol. 122, pp. 416-425.

[23] Yong, C., Barth, E., and Riofrio, J., (2008) "Modeling and Control of a Free Liquid-Piston Engine Compressor," *Accepted to the Bath/ASME Symposium on Fluid Power & Motion control (FPMC 2008),* Bath, UK.

[24] http://www.kettering.edu/~drussell/Demos/MembraneCircle/Circle.html